

https://dspace.org/

Osmium as a potential Fischer-Tropsch catalyst using hollow carbon spheres as support

Tshepo, Molefe

2018

https://hdl.handle.net/10539/25876

Molefe, Tshepo (2018) Osmium as a potential Fischer-Tropsch catalyst using hollow carbon spheres as support,University of the Witwatersrand, Johannesburg, <http://hdl.handle.net/10539/25876>

Downloaded from a DSpace repository. https://dspace.org/

Osmium as a potential Fischer-Tropsch catalyst using hollow carbon spheres as support

By

Tshepo Molefe

Student number: 604157

A dissertation submitted to the Faculty of Science, University of the Witwatersrand, Johannesburg, in fulfilment of the requirements for the Degree of Masters of Science in Chemistry.

Supervisor: Prof Neil J. Coville

Co-Supervisor: Dr Roy Forbes

University of the Witwatersrand. Johannesburg. Date:

DECLARATION

I declare that this dissertation is my own, unaided work. It is being submitted for the degree of Master of Science at the University of the Witwatersrand, Johannesburg. It has not been submitted before for any degree or examination at any other University.





_____

Tshepo Molefe

On this 14 day of May 2018

DEDICATION

To my parents: Lizzie Madi and Richard Molefe.

Unconditional love to you'll

ACKNOWLEDGMENTS

I would like to express my sincere gratitude to the following people and institutions for their various roles in making this project a success:

- My supervisor, Professor N. J. Coville for his invaluable support, guidance and helpful suggestions and criticisms during this project.
- My co-supervisor, Dr R. Forbes for his support and guidance with XRD and Fischer-Tropsch related analysis.
- The staff members of the Microscopy and Microanalysis Unit at the University of the Witwatersrand for assistance with electron microscopy work.
- The glassblower, Mr T. Dzara for assistance with the quartz tubes and glassware modifications used for this work.
- Dr T. Phaahlamohlaka and Dr W. Dlamini for assistance with Fischer-Tropsch analysis.
- Tshepo for helping to set-up the Fischer- Trospch rig and assistance with other technical work.
- Late Rajesh Molose for being a friend and more since first year.
- All my colleagues in chemistry department and the CATOMMAT group for their support and assistance in helping with the research project.
- The DST-NRF Scarce Skills scholarship, DST-NRF Centre of Excellence in Catalysis "Cchange", and the University of the Witwatersrand.
- Lastly, My family for their patience in seeing me through this work and the Almighty God.

PRESENTATIONS

Tshepo Molefe, Nomthandazo Mbita, Arthur Moya, and Dr S Durbach. *Carbon Nano-fibres formation on a fly ash catalyst with hydrogen and nitrogen gas as carrier gases*. (**2nd Best oral presentation**). RAP, November 2013.

Tshepo Molefe, and Dr Carren Billing. *Investigation and parameter optimization for DPASV used to study complex formation.* (**Oral presentation**). RAP, November 2014.

Tshepo Molefe, Tumelo Phaahlamohlaka, Dr Roy Forbes, and Prof Neil Coville. *Osmium as a potential Fischer-Tropsch catalyst using hollow carbon spheres as support*. (**Oral presentation**). DST center of excellence in catalysis (cchange) meeting, Wits and UCT-Johannesburg, July 2016.

Tshepo Molefe, Tumelo Phaahlamohlaka, Dr Roy Forbes, and Prof Neil Coville. *Osmium as a potential Fischer-Tropsch catalyst using hollow carbon spheres as support*. (**Posetr presentation**). Catalysis South Africa (CATSA) conference - Drakensburg, November 2016.

Tshepo Molefe, Dr William Dlamini, Dr Roy Forbes, and Prof Neil Coville. *Osmium as a potential Fischer-Tropsch catalyst using hollow carbon spheres as support*. (**2nd Best poster presentation**). 7th SANi 2017 symposium – Technology University of Tshwane, November 2017.

Tshepo Molefe, Dr William Dlamini, Dr Roy Forbes, and Prof Neil Coville. *Osmium as a potential Fischer-Tropsch catalyst using hollow carbon spheres as support*. (**Oral presentation**). DST center of excellence in catalysis, Cchange symposium - Wits and UCT - Johannesburg, November 2017.

TABLE OF CONTENTS

DECLARATION ii

DEDICATION i

ACKNOWLEDGMENTS ii

PRESENTATIONS iii

ABSTRACT ix

LIST OF FIGURES x

LIST OF SCHEMATICS xiii

LIST OF TABLES xiv

LIST OF ABBREVIATIONS xv

Chapter 1: Introduction to study, research question and hypothesis 1

1.1. Introduction 1

1.2. Motivation 3

1.3. Aim 3

1.4. Objectives 4

1.5. Hypothesis and questions 4

1.6. Outline of dissertation 5

1.7. References 6

Chapter 2: Literature review 9

2.1. Hollow Carbon Spheres 9

2.1.1. Introduction 9

2.1.2. Synthesis of hollow carbon sphere by templating 10

2.1.3. Application of HCSs/core-shell structure in heterogeneous catalysis 15

2.1.3.1. Oxidation reactions 15

2.1.3.2. Reduction reactions 16
2.1.3.3. Hydrogenation reactions 18
2.1.3.4. Ficher-Tropsch reactions 19
2.2. Osmium as a hydrogenation catalyst 20
2.2.1. Introduction 20
2.2.2. Catalytic application of osmium 22
2.2.2.1. Os in organic chemistry 22
2.2.2.2. Os in inorganic chemistry 24
2.3. Fischer-Tropsch synthesis 32
2.3.1. History and background 32
2.3.2. Fischer-Tropsch synthesis 34
2.3.3. Fischer-Tropsch chemistry 36
2.3.4. Fischer-Tropsch synthesis product distribution 37
2.3.5. Fischer-Tropsch reaction 39
2.3.6. Fischer-Tropsch reaction mechanism 40
2.3.6.1. The methylene Insertion (carbide and alkyl) mechanism 41
2.3.6.2. The vinyl/alkenyl mechanism 41
2.3.6.3. The oxygenate mechanism 42
2.3.6.4. The CO insertion mechanism 42
2.3.7. Fischer-Tropsch catalysts 42
2.3.8. Fischer-Tropsch catalyst supports 44
2.3.8.1. Carbon support 45
2.3.8.2. Carbon supports in heterogeneous catalysis 46
2.3.9. Shaped carbon material 46
2.3.9.1. Activated carbon 47
2.3.9.2. Carbon nanotubes 48
2.3.9.3. Carbon nanofibers 49

2.3.9.4. Carbon sphere 50
2.3.9.5. Hollow carbon spheres 51
2.3.10. Conclusions and outlook 51
2.4. Reference 52
Chapter 3: Experimental and characterization procedures for the synthesis of hollow carbon spheres encapsulating osmium nanoparticles and the Fischer-Tropsch process. 65
3.1. Introduction 65
3.2. Materials 65
3.3. Method for synthesizing Os@HCS 65
3.3.1. Synthesis of ammonium hexachloroosmate (IV), $(NH_4)_2OsCl_6$ 65
3.3.2. Synthesis of silica spheres 66
3.3.3. Synthesis of Os/SiO_2 66
3.4. Experimental procedure for synthesizing hollow carbon spheres 67
3.4.1. Gases 67
3.4.2. Chemical vapour deposition reactor set-up 67
3.5. Structural characterization 68
3.5.1. Transmission electron microscopy (TEM) 68
3.5.1. Scanning electron microscope (SEM) 69
3.5.2. Powder X-ray diffraction (PXRD) 69
3.5.3. Inductively coupled plasma optical emission spectroscopy (ICP-OES) analysis 69
3.5.4. Thermogravimetric analysis (TGA) 69
3.5.5. Temperature programmed reduction 70
3.5.6. Brunauer-Emmet and Teller (BET) surface area measurement 70
3.5.7. Fourier transform infrared spectroscopy (FTIR) 70
3.6. Experimental procedure for Fischer-Tropsch synthesis 71
3.6.1. Gases 71
3.6.2. Reactor setup 71

3.6.3. Catalytic experiments 73
3.6.4. Gas chromatography calibration and product analysis 73
3.7. Mass balance calculations 76
3.8. Reference 78
Chapter 4: Synthesis and characterization of osmium nanoparticles encapsulated in hollow carbon spheres 79
4.1. Introduction 79
4.2. Experimental 81
4.2.1. Synthesis of Stöber silica sphere supporting Os (Os/SiO_2) 81
4.2.2. Synthesis of Os nanoparticles encapsulated in HCSs (Os@HCS) 81
4.2.3. Characterization techniques 82
4.3. Results and discussion 82
4.3.1. Electron microscopy 82
4.3.2. Os nanoparticles loaded on Stöber silica spheres (5% Os/SiO_2) 83
4.3.3. Carbonized Os nanoparticles loaded on Stöber silica spheres (5% Os/SiO2@C) 85
4.3.4. Os nanoparticles encapsulated inside hollow carbon spheres (5% Os@HCS) .. 86
4.3.5. Energy dispersive X-ray spectroscopy 89
4.3.6. Fourier transformation infrared spectroscopy 89
4.3.7. Powder X-ray diffraction 91
4.3.8. Thermogravimetric analysis 93
4.3.9. Nitrogen absorption-desorption analysis 95
4.4. Conclusion 97
4.5. Reference 99
Chapter 5: Application – osmium encapsulated inside hollow carbon spheres as a Fischer Tropsch synthesis catalyst. 102
5.1. Introduction 102
5.2. Experimental 103

5.2.1. Catalyst preparation 103
5.2.2. Characterization 104
5.2.3. Catalytic evaluation 105
5.3. Results 105
5.3.1. Transmission electron microscopy 106
5.3.2. Powder X-ray diffraction 110
5.3.3. Temperature programmed reduction 111
5.3.4. Fischer-Tropsch evaluation 114
5.3.5. Transmission electron microscopy studies of a spent catalyst 120
5.3.6. Poweder X-ray diffraction studies of a spent catalyst 122
5.4. Conclusion 124
5.5. Reference 125
Chapter 6: Conclusions and recommendations 128
6.1. Conclusion 128
6.2. Recommendations 129
Appendix 1 130

ABSTRACT

Little attention has been given to the use of osmium as a catalyst or promoter for Fischer Tropsch synthesis (FTS). In this study the synthesis and use of osmium nanoparticles supported or encapsulated inside hollow carbon sphere (HCS) as a potential FT catalyst is reported. Os is not expected to be a good FT catalyst and this study provided for an evaluation of the role of Os on carbon as a catalyst in the FT reaction. The Os was encapsulated inside hollow carbon spheres (HCSs) as this will eventually allow for a study of spillover effects in FT reactions. The Os@HCS was prepared using sacrificial Stöber silica spheres as a template. The SiO_2 spheres were loaded with Os ($(NH_4)_2OsCl_6$ metal precursor) via two methods: homogenous deposition precipitation (HDP) and wetness impregnation (WI). The Os/SiO_2 was encapsulated by a carbon layer deposited by CVD using toluene. Removal of the sacrificial template gave Os@HCS (d_{Os} = 11-17.5 nm; d_{HCS} = 450-560 nm). Numerous physicochemical properties were used to reveal that the Os@HCS catalyst had been successfully synthesized. These included electron microscopy, PXRD, TGA, BET, and TPR studies. In the FTS evaluation, the Os@HCS and Os/SiO_2 (as reference) showed low activity compared to conventional FT catalysts. The Os supported catalysts showed a product selectivity mainly to C_1 and C_2 hydrocarbons with high selectivity towards methane (> ~65%).

LIST OF FIGURES

Figure 2. 1: Representation of (a) solid, (b) core-shell, and (c) hollow carbon spheres. 9
Figure 2. 2: General schematic synthesis of HCS through pre-synthesized template [1]. 10
Figure 2. 3: Scheme illustrating the templating strategies, based on the nature of the template, for the synthesis of HCS [18]. 12
Figure 2. 4: Synthetic strategy for the hydrothermal carbonisation (HTC) of hollow carbon spheres using polystyrene latex as a soft template and carbohydrate biomass as a carbon source [16]. 13
Figure 2. 5: TEM images of (a, b) SiO_2@m-SiO_2 and (c) mHCSs [31, 32]. 15
Figure 2. 6: TEM images of (a) Pd@HCS and (b) Pd/HCS [36]. 16
Figure 2. 7: TEM images of (a) Au@HCS, (c) Pd@NC nanoreactors initially synthesized and (e) recovered after 6 recycles. SEM image of (b) Pd@NC nanoreactors. (d) Time dependent conversion of 4-nitrophenol by $NaBH_4$ to 4-aminophenol. (f) Catalytic conversion of 4-nitrophenol by using recycled Pd@NC nanoreactors at different cycle times [65] 17
Figure 2. 8: TEM, SEM images and Ru particles size distribution of Ru@MHCS (a,b,c), and Ru@HCS (d,e,f). 19
Figure 2. 9: Transmission electron microscopy (TEM) images of various shaped Os nanoparticles/nanoclusters. (A) and (B) show a low and high magnified TEM images of aggregated Os nanoclusters. (C) and (D) show a low magnified image of Os chain-like networks. (E) and (F) show a show a high magnified image of Os chain-like networks. (G) and (H) show a low and high magnified image of spherical shaped Os nanoparticles [23] 21
Figure 2. 10: TEM image of kidney tissue. (A) Shows a TEM image with no OsO_4 staining on kidney tissue. (B) Shows a TEM image of kidney tissue in presence of OsO_4 staining, note enhancement of contrast of mitochondrial cristae, mitochondrial dense granules, plasma membrane, and nuclear envelope [93]. 23
Figure 2. 11: TEM image of self-assembled Os nanoclusters in DNA. (A), (B) and (C) show the low and high magnification of DNA-Os nanoclusters having a wire-like morphology [71]. 24

Figure 2. 12: CO conversion catalysed by $Os_3(CO)_{12}/Al_2O_3$ – reactant, $He:H_2:CO$ = 1:3:1, total pressure: 7.9 x 105 $N.m^{-2}$, temperature: 573 K, mass of catalyst: 0.1651 g, Os content: 0.24 wt%, feed flow rate: 166 scc min^{-1} (T = total conversion) [104]. 27
Figure 2. 13: Deconvolution of the Os 4f XPS spectra of pristine Os/SiO_2 (top) and after air exposure (bottom) [65, 66]. 30
Figure 2. 14: (a) Representative HAADF-STEM micrograph of Os/SiO_2 after exposure to air. (b) Particle size distribution of the Os [106]. 31
Figure 2. 15: Three stages in Fischer–Tropsch process [123] 35
Figure 2. 16: Plot of log (W_n/n) against n illustrating the ASF distribution [129] 38
Figure 2. 17: Representation of activated carbon particle [154]. 47
Figure 2. 18: TEM image of CNTS under low magnification [153]. 48
Figure 2. 19: TEM images of (a) a cobalt oxide particle deposited on the edge of a fish bone CNF, (b) Co/Platelet catalyst, (c) Co/CNF [161]. 49
Figure 2. 20: Carbon nanospheres SEM image (a), Carbon nanospheres agglomerated TEM image (b) [184]. 50

Figure 3. 1: Horizontal CVD set up. 68
Figure 3. 2: Schematic illustration of the reactor and rig setup. 72
Figure 3. 3: Schematic diagram of a fixed bed reactor. 72
Figure 3. 4: A GC-TCD trace recorded during syngas calibration H_2 (60%), N_2 (10%) and CO (30%). 74
Figure 3. 5: A GC-FID trace recorded during the six-gas mixture calibration 74
Figure 3. 6: A GC-FID trace recorded during a typical FTS run. 75

Figure 4. 1: Silica and Os/SiO_2 spheres. (a) SEM image of Stöber silica spheres, (b) TEM image of Stöber silica spheres, (c) TEM image of 5% Os/SiO_2 prepared via wetness impregnation method, and (d) TEM image of 5% Os/SiO_2 prepared via homogenous deposition precipitation method. (e) SiO_2 particle size distribution. 84
Figure 4. 2: (a) SEM and (b) TEM images of 5% Os/SiO_2@C from 5% Os/SiO_2 prepared via the homogeneous deposition precipitation method. 86
Figure 4. 3: (a) and (b) SEM images of 5% Os@HCS prepared via homogenous deposition precipitation and wetness impregnation method, respectively. (c) and (d) TEM images of 5% Os@HCS prepared via homogenous deposition precipitation and wetness impregnation

method, respectively. (e) and (f) up close TEM images of 5% Os@HCS prepared via homogenous deposition precipitation and wetness impregnation method, respectively 87
Figure 4. 4: Os nanoparticle size distribution from (a) Os@HCS HDP and (b) Os@HCS WI. 88
Figure 4. 5: Spectrum 1 - EDS of SiO_2; Spectrum 2 - EDS of Os@HCS synthesized via wetness impregnation method; Spectrum 3 - EDS of Os@HCS synthesized via homogenous deposition precipitation method; and Spectrum 4 - EDS of Os/SiO_2@C. 89
Figure 4. 6: FTIR spectra of the Os/SiO_2, Os@HCS prepared via the wetness impregnation and homogeneous deposition precipitation methods, and HCS only. 90
Figure 4. 7: PXRD patterns of the synthesized 5% and 10% Os@HCS prepared via the wetness impregnation and homogeneous deposition precipitation methods. 92
Figure 4. 8: TGA thermograms for the bulk assembled synthesized 5% and 10% Os@HCS prepared via the wetness impregnation and homogeneous deposition precipitation methods 93
Figure 4. 9: First derivative of TGA thermograms for the bulk assembled synthesized 5% and 10% Os@HCS prepared via the wetness impregnation and homogeneous deposition precipitation methods. 94
Figure 4. 10: N_2 adsorption-desorption isotherms of (a) HCS only and (b) 5% Os@HCS WI catalyst. 96

Figure 5. 1: TEM images and particle size distribution for: (a) and (b) 5% O/SiO_2, (c) and (d) 10% Os/SiO_2 catalyst. 107
Figure 5. 2: TEM images and particle size distribution for: (a) and (b) 5% Os@HCS HDP, (c) and (d) 10% Os@HCS HDP. 108
Figure 5. 3: TEM images of 10% Os@HCS HDP catalyst. (a) Lower magnification TEM image, displaying the larger portion of the spent catalyst. (b) High magnification TEM image, displaying the presence of carbon nanofibers on the surface of the HCSs from the spent catalyst. 109
Figure 5. 4: PXRD pattern of 5% Os@HCS HDP, 10% Os@HCS HDP, and 10% $Os/SiO_2$111
Figure 5. 5: H_2-TPR profile for Os nanoparticles on various supports, 5% Os@HCS HDP, 10% Os@HCS HDP, and 10% Os/SiO_2 HDP catalysts. 114
Figure 5. 6: CO conversions for the Os supported catalysts over 150 hours on stream at different reaction temperatures. 116
Figure 5. 7: Olefin to paraffin ratio of Os supported catalysts at various temperatures. 119

Figure 5. 8: TEM images and particle size distribution for: (a) and (b) 5% Os@HCS HDP, (c) and (d) 10% Os@HCS HDP, (e) and (f) 10% Os/SiO_2 spent catalysts. 121
Figure 5. 9: PXRD patterns of the synthesized 5%, 10% Os@HCS and 10% Os/SiO2 via homogeneous deposition precipitation methods. 123

Figure S. 1: CO conversions for the Os supported catalysts over 150 hours on stream at different reaction temperatures. 130
Figure S. 2: CO conversions for the Os/SiO_2 catalysts over 150 hours on stream at different reaction temperatures. 131

LIST OF SCHEMATICS

Scheme 2. 1: Schematic illustration of olefin hydrogenation to form an alkane [15]. 18

Scheme 3. 1: Schematic illustration of Os@HCS synthesis 68

LIST OF TABLES

Table 2. 1: Catalytic activity comparison between Pt@hmC, Pt/PVP and Pt/AC [9]. 18
Table 2. 2: A comparison of activation energies (a) and reaction rates (b) [66]. 28
Table 2. 3: Typical product selectivity from two Sasol processes [138].....39
Table 2. 4: Comparison of Co, Fe and Os as catalysts for the FT reaction [137]. 43

Table 3. 1: Specification of the GC operating conditions.....75

Table 4. 1: Particle size data for osmium nanoparticles and hollow carbon spheres. 92
Table 4. 2: Textual properties (surface area, pore volume and average pore size) of the hollow carbon sphere support and osmium encapsulated inside hollow carbon spheres. 97

Table 5. 1: Fischer-Tropsch synthesis catalytic performance of Os supported catalysts. 117
Table 5. 2: Particle size data for osmium nanoparticles and hollow carbon spheres. 124

LIST OF ABBREVIATIONS

Abbreviation	Description
ASF	Anderson Schulz Flory
BET	Branauer Emmett Teller
CNF's	Carbon nanofibers
CNT's	Carbon nanotubes
CVD	Chemical Vapour Deposition
FID	Flame ionization detector
FTIR	Fourier Transform Infrared Spectroscopy
FTS	Fischer-Tropsch synthesis
GC	Gas chromatography
HCS	Hollow Carbon Spheres
HDP	Homogeneous deposition precipitation
PXRD	Powder X-ray diffraction
SEM	Scanning Electron Microscopy
TCD	Thermal conductivity detector
TEM	Transmission Electron Microscopy
TGA	Thermo-Gravimetric analysis
TPR	Temperature Programmed Reduction
WI	Wetness Impregnation
WGS	Water gas shift
α	Alpha

Chapter 1: Introduction to study, research question and hypothesis

1.1. Introduction

Given the world's finite fossil fuel resources, as well as the ever-growing population, it has been clear that the energy supply is unsustainable for humans current and long term demand for energy. Even though crude oil derived fuels have long been used, research has shown that its popular demand has put a strain on the world's crude oil reserves and there has been a concern about the depletion of the global crude oil reserves [1].

The major contributing factor for global warming is greenhouse gases such as CO_2 and CH_4 which are emitted from the combustion of fossil fuels. In 2015, 399 pm of CO_2 was recorded in the atmosphere [2]. The serious climatic concerns such as heat waves, sea levels, and droughts arising from global warming are the driving forces for the utilization of carbon dioxide to produce biofuels. Generally, biofuels can be produced from biomass including municipal solid waste, vegetable oil, algae, agricultural by-products and nonedible oils. One of the processes to produce liquid fuels from biomass is via gasification to produce syngas (mixture of hydrogen and carbon monoxide) which is converted to liquid fuels via the Fischer-Tropsch synthesis.

Fischer-Tropsch synthesis (FTS) is one of the most promising alternative routes for the production of cleaner energy source such as synthetic liquid fuels and synthetic lubricants. The FTS provides an alternative that will reduce global warming and the dependency of fossil fuel utilization. In FTS syngas is catalytically converted to a mixture of hydrocarbons C_1-C_{60} (olefin, paraffin, and oxygenates). The reaction mechanisms involved in FTS are complex, however reactions (1) and (2) are desirable, whereas the major undesirable side reaction is water gas shift (WGS) (3).

$$(2n + 1)\ H_2 + nCO \rightarrow C_nH_{2n+2} + nH_2O \quad (1)$$

$$2nH_2 + nCO \rightarrow C_nH_{2n} + nH_2O \quad (2)$$

$$CO + H_2O \rightarrow CO_2 + H_2 \quad (3)$$

The most commonly used catalysts in FTS are the group 8-10 metals of the Periodic Table [3, 4]. The most widely and commercially viable metals for the FTS are iron and cobalt at temperatures between 200 and 300 °C, and at 10-60 bar pressure [5, 6]. Generally, the iron based catalysts show high WGS activity, therefore, they are more preferable in conversion of hydrogen lean synthesis gas ($H_2/CO < 1.8$), typically derived from coal and biomass [7]. Iron based catalysts are more selective towards the production of olefins (gasoline, hydrocarbons and linear alpha-olefins) and oxygenates (alcohols, aldehydes and ketones) compared to paraffins. However, the selectivity towards the iron catalyst can be varied with temperature [8]. On the other hand, cobalt based catalysts show low activity for the WGS reaction and they are more preferable for the synthesis of long-chain linear paraffins. Cobalt based catalysts are more selective towards the production of paraffins and C_{5+} hydrocarbons or heavy molecular weight waxes compared to iron catalyst and they exhibit higher hydrocarbon production per unit mass of the catalyst [7, 8].

The catalyst performance is a backbone for the economy of the FTS process. Therefore, FTS research focus is developing catalysts with improved hydrocarbon yield. This can be achieved by incorporating appropriate promoters and support materials. Typically, an FT catalyst promoter functions as a structural promoter or as an electronic promoter. Structural promoters stop metal sintering by separating the surfaces of active atoms. Electronic promoters donate electrons to enhance reducibility and catalytic activity of an active metal. The promotion of cobalt catalyst can be achieved by addition of small quantities of noble metals, such as Pt, Ru, Au or Re. Whereas, the promotion of iron catalyst can be achieved by addition of small quantities of Mn, K, and Cu metals. Typically, an FT catalyst is dispersed on a support material and most commonly metal oxides such as Al_2O_3, TiO_2, SiO_2 and MgO, and various shaped carbon materials are used as support materials for FT catalysts [5, 9, 10]. Research work has shown that the support material plays a vital role in influencing the dispersion of the active metal as well as stabilizing the active metal phase against loss of surface area due to sintering or agglomeration in FTS reaction conditions.

Metal oxides as support materials have shown to produce hard-to-reduce complexes, such as Co_2SiO_2, $CoTiO_2$ and $Co_2Al_2O_4$. The hard-to-reduce complexes are attributed by the strong interaction of these supports with the catalyst precursors [11-13]. An alternative to hard-to-reduce complexes formation is the use of carbon based support materials. In the last decade the possibility of making hollow supports with the metal placed inside the support has become possible [14, 15]. Recently several reports have been reported for improving the stability of

metal nanoparticles by encapsulating the metal nanoparticles in hollow porous shells [16, 17]. In the case of using carbon as the support, hollow carbon spheres (HCSs) have been used in heterogeneous catalysis due to their relative chemical inertness, thus allowing easier reducibility and increased metal catalytic activity of metals incorporated in the HCS [18, 19].

1.2. Motivation

In the last decades, iron and cobalt based catalyst have been used as CO hydrogenation catalysts in FTS. As mentioned, the catalysts are usually promoted by metals that enhance FTS activity. Although Fe is much cheaper than Co, Co based catalysts are the preferred catalysts for industrial application. Cobalt FT catalysts promoted by precious metals such as Pt and Ru have shown to enhance the degree of reduction, facilitate hydrogenation activity and hence reduce propensity for carbon deposition, for example, by Exxon Mobil for ruthenium [20, 21]. Even though Ru is added in small quantities as a promoter its impact on the FT activity is highly desirable.

Osmium has similar properties to Ru in low oxidation states, thus, Os should also be able to act as a promoter in FT reactions. Prior to investigating the use of Os as a promoter it is necessary to establish the activity of Os as a FT catalyst. Indeed, while there have been very few studies on this topic, researchers have shown that Os can indeed show FT activity [22-28]. Even though osmium has been investigated on conventional oxide supports, to date, no reports on the application of Os nanoparticles encapsulated inside HCS (Os@HCS) for gas phase CO hydrogenation reaction in FTS has been reported. Since osmium and ruthenium resemble one another in low oxidation states, herein, we explore the use of osmium nanoparticles encapsulated in hollow carbon spheres as a potential Fischer-Tropsch catalyst.

1.3. Aim

The aim of this research is to synthesize osmium nanoparticles supported or encapsulated in hollow carbon spheres (nanoreactors) as an FT catalyst and to test its catalytic performance in the hydrogenation of CO.

1.4. Objectives

The aim of this project will be achieved through the following objectives:

I. Synthesise Stöber spheres as a template and use it in the synthesis of hollow carbon spheres (HCS) using chemical vapour deposition (CVD) procedures.
II. Compare two synthesis methods applied in synthesising the catalyst- support template precursor: the homogeneous deposition precipitation (HDP) and wetness impregnation (WI) methods.
III. Characterise the synthesised Os encapsulated in HCS (Os@HCS) using a wide range of techniques including: powder X-ray diffraction, thermal analysis (TGA), electron microscopy (SEM, EDS and TEM), Temperature programmed reduction (TPR), and BET surface area and pore size analysis.
IV. Evaluate the catalytic performance of 5% and 10% loaded Os encapsulated in HCS catalysts, and 10% loaded Os on silica sphere (SiO_2) catalyst in the FTS.

1.5. Hypothesis and questions

The osmium metal can be easily detected inside HCS due to its large size (high atomic number) by using microscopic techniques. The use of a HCS reduces the sintering effect of metal particles under reaction conditions (high temperature) and the porosity of the support enables reactants and products to diffuse and interact with the metal catalyst. The effect of loading of different metal percentage catalyst enables the detection of the size and location of Os nanoparticles inside the hollow carbon spheres. The Os metal has catalytic activity and selectivity in the FTS. Therefore, this study sought to utilize Os for enhanced detection and analysing its character under FTS conditions by addressing the following research questions:

I. Does encapsulating the metal inside the HCS reduce the sintering effect?
II. Is Os metal easily detected on a carbon support under microscopic techniques?
III. Can the size and shape of Os nanoparticles be controlled?

IV. What is the catalytic activity and selectivity of Os metal in the FT reaction?

1.6. Outline of dissertation

The content of the current dissertation is as follows:

- Chapter 1: Gives the research introduction, main motive for the research, aim and objectives, and hypothesis associated with research questions.

- Chapter 2: Gives a detailed review on the use of a carbon material as a heterogenous catalyst support, the application of Os in hydrogenation reactions, and a brief background and the process of Fischer-Tropsch synthesis.

- Chapter 3: Provides experimental procedures involved in synthesizing Os nanoparticles encapsulated in hollow carbon spheres, the characterization of the synthesized materials, the FT reactor setup and the calculations involved in the FT process.

- Chapter 4: Reports on the synthesis of Os supported on a Stober sphere template using wetness impregnation and homogenous precipitation deposition methods and the synthesis of Os nanoparticles encapsulated in a hollow carbon sphere support.

- Chapter 5: Reports on the application of Os encapsulated in a hollow carbon sphere catalyst and Os supported on a silica sphere in the Fischer-Tropsch synthesis.

- Chapter 6: Provides the conclusions and recommendations for this study.

1.7. References

1. Owen, N.A., O.R. Inderwildi, and D.A. King, *The status of conventional world oil reserves—Hype or cause for concern?* Energy policy, 2010. **38**(8): p. 4743-4749.
2. Ail, S.S. and S. Dasappa, *Biomass to liquid transportation fuel via Fischer Tropsch synthesis–Technology review and current scenario.* Renewable and Sustainable Energy Reviews, 2016. **58**: p. 267-286.
3. Anderson, R.B., H. Kölbel, and M. Rálek, *The Fischer-Tropsch Synthesis*. 1984: Academic Pr.
4. Vannice, M., *The catalytic synthesis of hydrocarbons from H2CO mixtures over the Group VIII metals: V. The catalytic behavior of silica-supported metals.* Journal of Catalysis, 1977. **50**(2): p. 228-236.
5. Dry, M., *The fischer-tropsch synthesis.* Catalysis science and technology, 1981. **1**: p. 159-255.
6. Jager, B. and R. Espinoza, *Advances in low temperature Fischer-Tropsch synthesis.* Catalysis Today, 1995. **23**(1): p. 17-28.
7. Khodakov, A.Y., W. Chu, and P. Fongarland, *Advances in the development of novel cobalt Fischer− Tropsch catalysts for synthesis of long-chain hydrocarbons and clean fuels.* Chemical reviews, 2007. **107**(5): p. 1692-1744.
8. Jahangiri, H., et al., *A review of advanced catalyst development for Fischer–Tropsch synthesis of hydrocarbons from biomass derived syn-gas.* Catalysis Science & Technology, 2014. **4**(8): p. 2210-2229.
9. Oukaci, R., A.H. Singleton, and J.G. Goodwin, *Comparison of patented Co F–T catalysts using fixed-bed and slurry bubble column reactors.* Applied Catalysis A: General, 1999. **186**(1): p. 129-144.
10. Jenness, G.R. and J.R. Schmidt, *Unraveling the Role of Metal-Support Interactions in Heterogeneous Catalysis: Oxygenate Selectivity in Fischer-Tropsch Synthesis.* Acs Catalysis, 2013. **3**(12): p. 2881-2890.
11. Mogorosi, R.P., et al., *Strong-metal–support interaction by molecular design: Fe–silicate interactions in Fischer–Tropsch catalysts.* Journal of catalysis, 2012. **289**: p. 140-150.
12. Liu, Y., et al., *Titania-decorated silicon carbide-containing cobalt catalyst for fischer–tropsch synthesis.* ACS Catalysis, 2013. **3**(3): p. 393-404.

13. Zhang, S., et al., *Dynamical Observation and Detailed Description of Catalysts under Strong Metal–Support Interaction.* Nano letters, 2016. **16**(7): p. 4528-4534.
14. Yin, Y., et al., *Formation of hollow nanocrystals through the nanoscale Kirkendall effect*. Science, 2004. **304**(5671): p. 711-714.
15. Kim, S., et al., *IR Spectroscopic Observation of Molecular Transport through Pt@ CoO Yolk− Shell Nanostructures.* Journal of the American Chemical Society, 2007. **129**(30): p. 9510-9513.
16. Hu, Y., et al., *Size-controlled synthesis of highly stable and active Pd@ SiO2 core–shell nanocatalysts for hydrogenation of nitrobenzene.* The Journal of Physical Chemistry C, 2013. **117**(17): p. 8974-8982.
17. Du, X. and J. He, *Carrier effect in the synthesis of rattle-type Au@ hollow silica nanospheres by impregnation and thermal decomposition method.* Microporous and Mesoporous Materials, 2012. **163**: p. 201-210.
18. Xiong, H., et al., *Cobalt catalysts supported on a micro-coil carbon in Fischer–Tropsch synthesis: A comparison with CNTs and CNFs.* Catalysis today, 2013. **214**: p. 50-60.
19. Trépanier, M., A.K. Dalai, and N. Abatzoglou, *Synthesis of CNT-supported cobalt nanoparticle catalysts using a microemulsion technique: role of nanoparticle size on reducibility, activity and selectivity in Fischer–Tropsch reactions.* Applied Catalysis A: General, 2010. **374**(1): p. 79-86.
20. Van Berge, P.J. and S. Barradas, *Catalysts*. 2008, Google Patents.
21. Inga, J., P. Kennedy, and S. LeViness, *Fischer-Tropsch process in the presence of nitrogen contaminants*. 2004, Google Patents.
22. Basset, J., et al., *Supported cluster and Mechanism of CO Reduction.* Fundam. Res. Homogeneous Catal, 1984: p. 19-53.
23. Ede, S.R., U. Nithiyanantham, and S. Kundu, *Enhanced catalytic and SERS activities of CTAB stabilized interconnected osmium nanoclusters.* Physical Chemistry Chemical Physics, 2014. **16**(41): p. 22723-22734.
24. Nithiyanantham, U., S.R. Ede, and S. Kundu, *Self-assembled wire-like and honeycomb-like osmium nanoclusters (NCs) in DNA with pronounced catalytic and SERS activities.* Journal of Materials Chemistry C, 2014. **2**(19): p. 3782-3794.
25. Anantharaj, S., et al., *Osmium organosol on DNA: application in catalytic hydrogenation reaction and in SERS studies.* Industrial & Engineering Chemistry Research, 2014. **53**(49): p. 19228-19238.

26. Boyd, E.P., et al., *Chemical vapor deposition of metallic thin films using homonuclear and heteronuclear metal carbonyls.* Chemistry of materials, 1997. **9**(5): p. 1154-1158.
27. Knözinger, H. and Y. Zhao, *Infrared characterization of mononuclear osmium carbonyl species on alumina.* Journal of Catalysis, 1981. **71**(2): p. 337-347.
28. Bungane, N., et al., *Fischer-Tropsch CO-Hydrogenation on SiO2-supported Osmium Complexes.* Zeitschrift für Naturforschung B, 2008. **63**(3): p. 289-292.

Chapter 2: Literature review

2.1. Hollow Carbon Spheres

2.1.1. Introduction

Spherically shaped carbon materials can be thought of as materials composed of subsequent layers of graphitic flakes with random twists [29] deposited in a manner that follows the curvature of the sphere. The spherical curvature layer is due to different carbon ring sizes that coexist. There are three types of spherically shaped carbon materials; namely solid carbon spheres (SCSs), core-shell carbon spheres (CSCSs), and hollow carbon spheres (HCSs) [30] (figure 2.1).

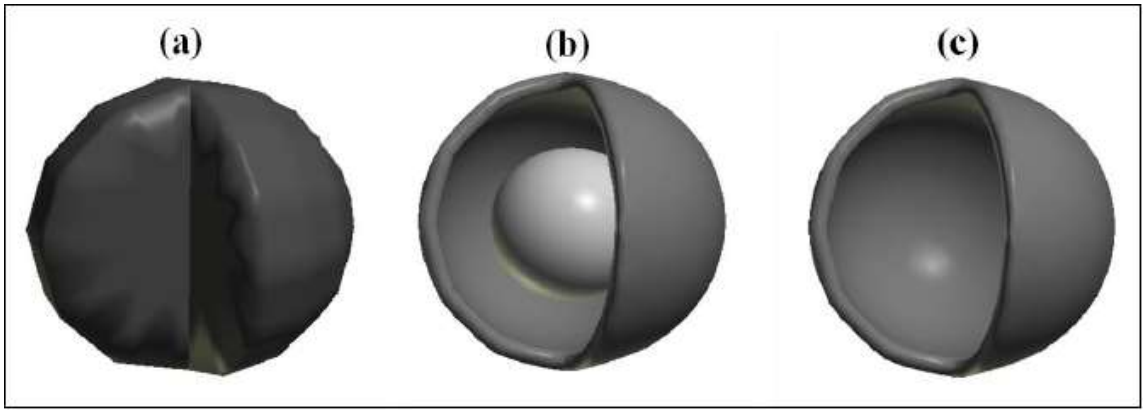


Figure 2. 1: Representation of (a) solid, (b) core-shell, and (c) hollow carbon spheres.

Solid carbon spheres (SCSs) are nanospheres made of graphitic flakes that form a completely dense structure. The layers of graphitic flakes within a SCS are not closed and this arrangement allows for their use in various applications such as reinforcement materials for rubber, lubricating materials, and in catalysts as a catalyst support [31].

Both the core-shell and hollow carbon sphere are closely related, in that the core-shell structure involves the encapsulation of a core by a "shell" (hollow carbon sphere) which is chemically different and therefore allows for the fabrication of materials with multiple functionalities. The multiple functionality of these materials makes them excellent candidates for applications in drug delivery, catalysis, photonic crystals, bio-diagnostics and energy and energy storage [32].

Core-shell structured materials can encapsulate cores of different chemical composition within a polymeric or inorganic shell. Metal nanoparticles can be encapsulated in silica spheres ($M@SiO_2$) and theses materials have shown that core-shell materials have a potential in electronics, magnetic, optic and catalysis fields [33-35]. Mesoporous core-shell carbon spheres have been reported to comprise of an active metal precursor as the core encapsulated by a mesoporous shell which is a suitable candidate for nanoparticle immobilization in catalysis. The porous shell prevents particle aggregation and ensures a short diffusion distant of reagent molecules [36]. Carbon-based shells encapsulating metal nanoparticles are interesting because of carbon's tuneable pore structure and relative chemical inertness. One such core-shell composite involved platinum nanoparticles encapsulated in hollow porous carbon shell (Pt@HCS) [37]. The Pt@HCS was synthesised using a hard template method where Pt nanoparticles were coated with a silica layer, and subsequently coated again with a carbon layer to form $Pt@SiO_2@C$. Afterwards, silica was etched out resulting in the formation of Pt@HCS structure. The Pt@HCS structure prevented Pt particle aggregation during olefin hydrogenation reactions [38]. This structure was further tested by replacing platinum with rhodium, and similar findings were observed whereby the metals were stabilized against aggregation while still maintaining their catalytic activity [38].

2.1.2. Synthesis of hollow carbon sphere by templating

The precise synthesis of well-ordered and porous HCSs has been achieved through the use of a pre-synthesized template or scaffold structure [39], as shown schematically in Figure 2.2.

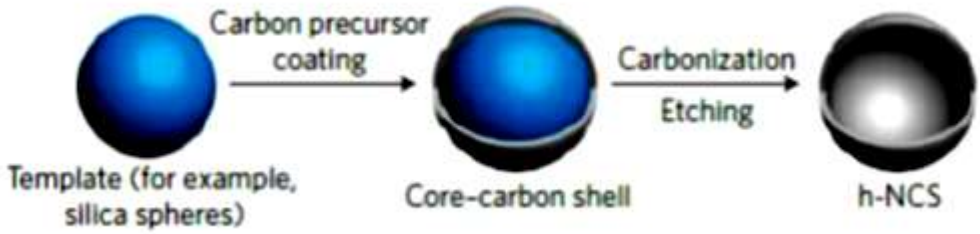


Figure 2. 2: General schematic synthesis of HCS through pre-synthesized template [1].

Generally the synthesis of HCS via the templating route requires (1) production of the template; (2) simple modification of the template; (3) uniform encapsulation of the template by a shell precursor; and (4) a facile method for the removal of the template [40-42]. The carbonization of the template can be performed under gas-phase chemical vapour deposition (CVD) wherein a carbon source (i.e. bubbled toluene or acetylene) is deposited or decomposed at high temperatures onto a template, followed by the removal of the template thus resulting in the formation of HCSs [43]. Alternatively carbonization of a template can be achieved through a hydrothermal method under high pressures in a autoclave reactor, wherein a biomass monomer (usually glucose) is catalytically polymerized in solution in the presence of a template, and subsequently calcined at high temperature to carbonize the reactant [44, 45]. HCSs synthesized via CVD typically have a high graphitic carbon content whereas those synthesized via hydrothermal method have a higher specific surface area due to their high porosity, as opposed to CVD synthesized HCSs [43].

Fabrication of HCSs by the template approach is done through the use of two main strategies known as the soft- and hard-templating (Figure 2.3 (i) and (ii), respectively) [46].

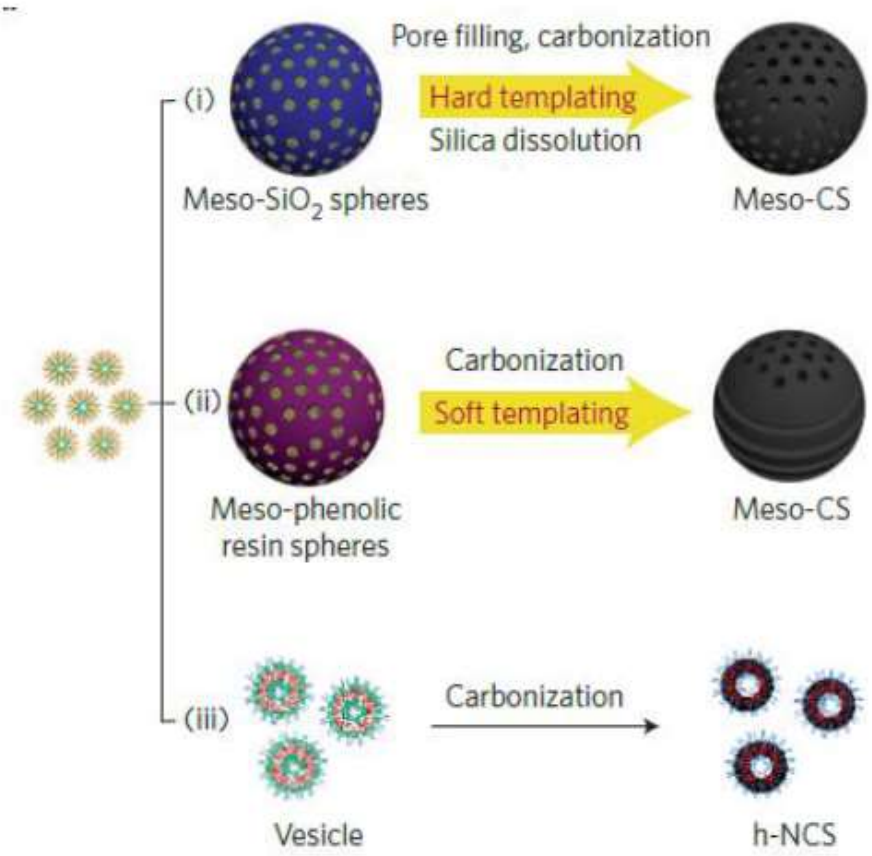


Figure 2. 3: Scheme illustrating the templating strategies, based on the nature of the template, for the synthesis of HCS [18].

Generally a template is any material that will provide the underlying structure that possesses the specific dimensions of interest. Templates are classed based on their physicochemical properties, and their templating methods [47]. Templates can be synthesised materials or naturally occurring materials such as inorganic minerals.

2.1.2.1.Soft-templating route

Soft templates are typically made of soft matter, which is organic molecules or amphiphilic supramolecules such as surfactants and polymers. These molecules usually form vesicles in aqueous media through hydrogen bonding and involve hydrophilic or hydrophobic interactions [48]. The ability of these organic structures to self-organize enables easy manipulation of the pore structure of the nanomaterials to be synthesized. The supramolecular interaction of the

template with a carbon precursor gives a well-defined organic-organic structure [49, 50]. The soft template can then either be removed at later stages of the synthesis or removed by extraction or calcination procedures. For example, polyvinyl alcohol a soft template has been used in large scale hydrothermal synthesis of HCSs with a high specific surface area of 1036 m^2/g using a phenolic resin as a carbon source [51]. The polyvinyl alcohol polymer template is decomposed/collapsed under high calcination temperatures to remove the template. Similarly, polystyrene latex beads have been used to synthesize HCSs using the hydrothermal method (Figure 2.4) [44].

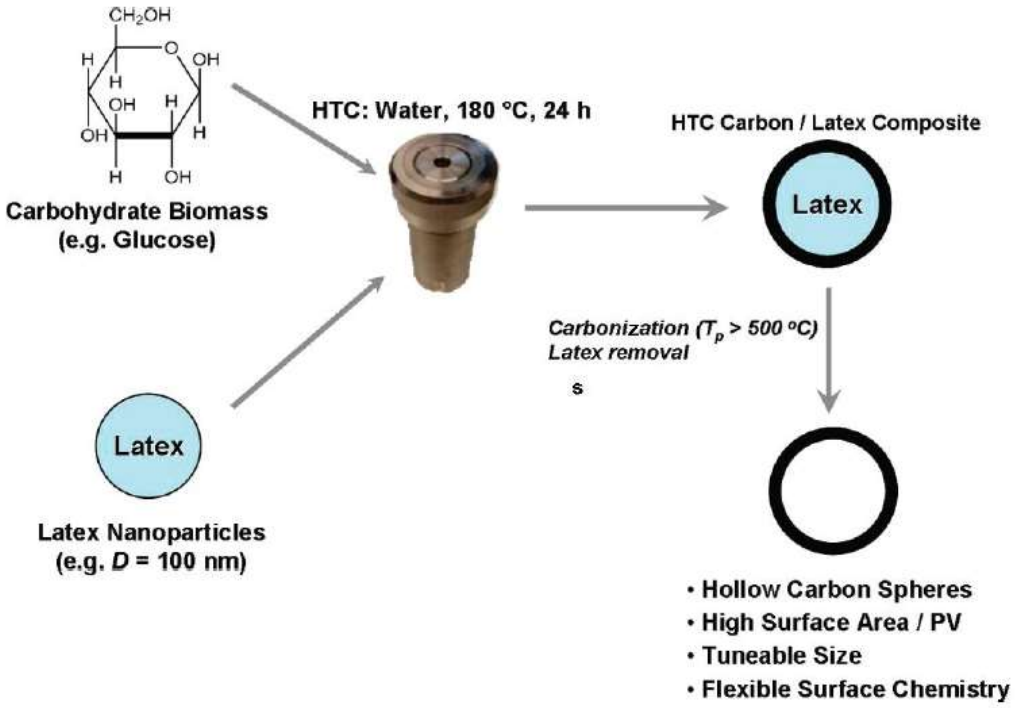


Figure 2. 4: Synthetic strategy for the hydrothermal carbonisation (HTC) of hollow carbon spheres using polystyrene latex as a soft template and carbohydrate biomass as a carbon source [16].

The general advantage of soft-templating is that it does not require the use of hazardous chemicals such as HF or NaOH for template removal. The disadvantage of soft-templating is its lack of reproducibility when synthesis is applied in large quantities.

2.1.2.2.Hard-templating route

Hard templates are one of the most effective templates used for the synthesis of HCSs with well-defined pore structures [52, 53]. The hard-templating route involves prior preparation of solid particles such as silica particles synthesised by the Stöber method [54]. This route of HCS synthesis requires an additional synthesis step for the removal of the sacrificial template after formation of a carbon shell-template complex which entails dissolution or etching via the use of hazardous chemicals such as HF or NaOH.

In the HCS synthesis the Stöber method is used to synthesize uniform and monodispersed colloidal silica spheres with a size range of 50-2000 nm [55]. The method is highly reproducible. Colloidal silica spheres are produced through the hydrolysis of silicon alkoxides (e.g. tetraethyl orthosilicate, TEOS) in ethanolic media (water-ethanol) using ammonia as a catalyst (Eq. 2.1) and an anti-aggregation agent. The solution forms by condensation of silanol groups to produce siloxane bonds (Si-O-Si) producing by-products which are water (Eq. 2.2) and alcohol (Eq. 2.3) [56].

The size of monodispersed silica spheres produced can be varied by changing the ethanolic media ratio, the TEOS, and the ammonia concentration [57]. The ammonia functions as an anti-aggregation agent by creating a positively charged layer of NH_4^+ ions on the surface of the silica that inhibits silica particles from aggregation.

The reactions involved include:

Hydrolysis: $\equiv Si–OR + H_2O \leftrightarrow \equiv Si–OH + ROH$ (2.1)

Water condensation: $\equiv Si–OH + \equiv Si–OH \leftrightarrow \equiv Si–O–Si + H_2O$ (2.2)

Alcohol condensation: $\equiv Si–OR + \equiv Si–OH \leftrightarrow \equiv Si–O–Si + ROH$ (2.3)

where R is an alkyl group

The use of colloidal silica spheres and an amphiphilic block copolymer, polystyrene-b-polyethylene oxide, in a dual-template approach has been applied in the synthesis of N-doped HCSs with large mesopores (~20 nm) and surface area [58]. It is often desirable to functionalize the surface of the template in order to tailor the specific surface area, pore size and the pore structure of the final nanostructure. For example Chen et al. functionalized silica spheres with

a mesoporous silica layer to form SiO_2@m-SiO_2 template (Fig. 2.5). In the synthesis of a SiO_2@m-SiO_2 a surfactant CTAB (cetyltrimethylammonium bromide) was used as a structure directing agent. The use of CTAB resulted in the deposition of a carbon source onto the silica template which led to higher yields, and it also resulted in the production of high surface area (771 m^2/g) mesoporous hollow carbon spheres (mHCSs) [59].

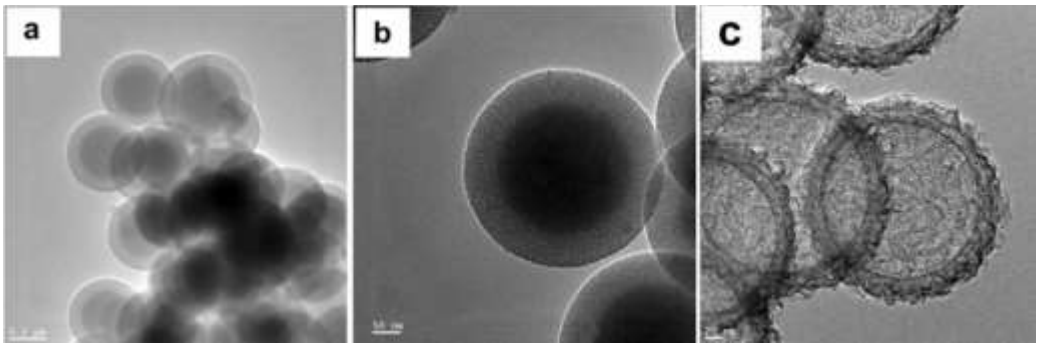


Figure 2. 5: TEM images of (a, b) SiO_2@m-SiO_2 and (c) mHCSs [31, 32].

2.1.3. Application of HCSs/core-shell structure in heterogeneous catalysis

HCSs have application in different catalysed chemical reactions such as (i) oxidation, (ii) nitroarene reduction, (iii) hydrogenation reaction, (iv) Fischer-Tropsch synthesis, and (iv) the integration of multiple catalytic reactions. The HCSs are applied in these reactions as nanoreactors, where the interior void space is initially functionalized with a catalytically active particle thus allowing chemical reactions to take place in the core area. The nanoreactor composition is described as single-or multi-core with the hollow shell structure composed of oxide materials, carbon-based materials, or organic polymers. Some of the different types of chemical reactions that have been performed using nanoreactors in catalytic systems are described below

2.1.3.1.Oxidation reactions

Many reports are available in literature regarding the use of nanoreactors in catalytic oxidation reactions [60-62]. The use of nanoreactors introduces a more enhanced thermal stability to a catalyst. For example, Huang *et al.* encapsulated gold nanoparticles in hollow titania and

zirconium dioxide shells for CO oxidation reactions [63]. The findings were that the Au active material maintained its catalytic activity even at temperatures of 800 ℃ (50% CO conversion) which was also observed at 200 ℃ [63]. The nanoreactors have also been shown to be viable in liquid phase oxidation reactions. For example, Harada *et al.* synthesized palladium nanoparticles encapsulated in hollow carbon spheres (Pd@HCSs) for the oxidation of alcohols [64] which is an important process in organic synthesis. This reaction occurred under elevated temperatures. Pd@HCS was compared with Pd nanoparticles loaded on hollow carbon spheres (Pd/HCS) (Fig 2.6).

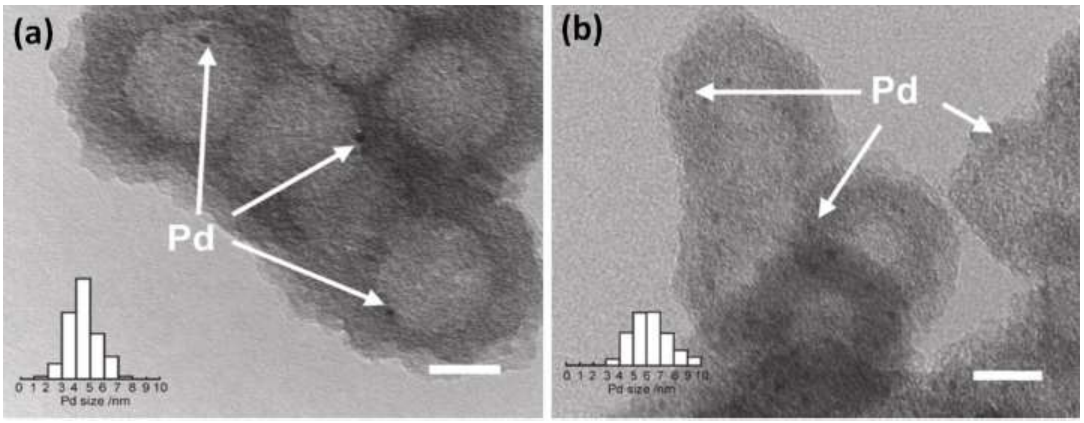


Figure 2. 6: TEM images of (a) Pd@HCS and (b) Pd/HCS [36].

The findings were that Pd@HCS had a greater activity for the oxidation of primary alcohols compared to Pd/HCS even though the mechanistic aspects of the reaction were the same, thus implying that the increase in activity of the catalyst was due to the core-shell structure.

A similar observation was observed by Chen *et al.* where Pd@*hm*CeO_2 catalysts had a superior activity and stability when compared to a Pd/*hm*CeO_2 counterpart and Pd/C catalysts for the oxidation of cinnamyl alcohol [61]. Therefore the encapsulation of an active particle inside a hollow shell structure improves the catalytic activity and stability of catalysts.

2.1.3.2.Reduction reactions

Catalytic reduction of nitrophenol has been reported to be catalysed by a yolk-carbon shell structure. For example, Rui *et al.* synthesized a monodispersed gold nanoparticle encapsulated in a hollow carbon sphere (Au@HCS) (Fig 2.7) as a catalyst for *o*-nitrophenol reduction. The

Au@HCS catalysed the reduction of *o*-nitrophenol to *o*-aminophenol by $NaBH_4$ within 10 min [32]. Another similar example, Shao *et al.* reported the reduction of 4-nitrophenol to 4-aminophenol by $NaBH_4$. The reaction was catalysed by palladium nanoparticle encapsulated in nitrogen doped hollow carbon sphere (Pd@NHCS) nanoreactors [65]. In synthesizing Pd@NHCSs, Pd nanoparticles were first adsorbed onto the $-NH_2$ functionalized silica nanospheres and then coated with dopamine. The dopamine was transformed to poly-dopamine and finally the silica was etched using NaOH.

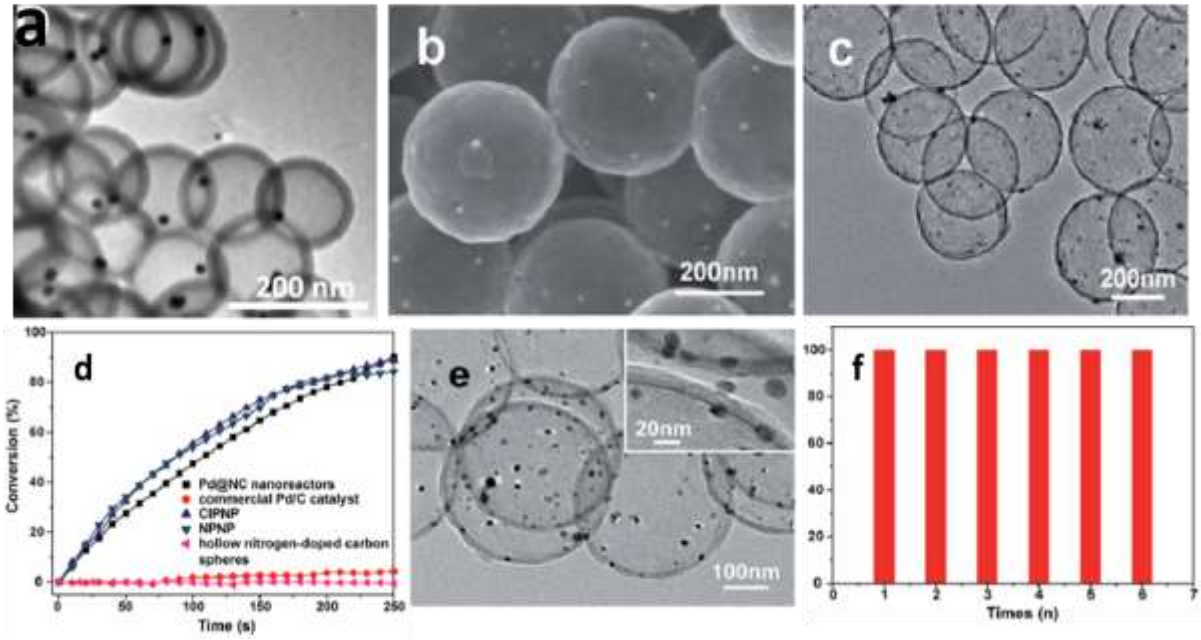


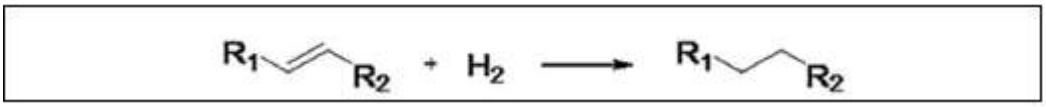
Figure 2. 7: TEM images of (a) Au@HCS, (c) Pd@NC nanoreactors initially synthesized and (e) recovered after 6 recycles. SEM image of (b) Pd@NC nanoreactors. (d) Time dependent conversion of 4-nitrophenol by $NaBH_4$ to 4-aminophenol. (f) Catalytic conversion of 4-nitrophenol by using recycled Pd@NC nanoreactors at different cycle times [65].

The conversion rate of 4-nitrophenol to 4-aminophenol reached 90% after 4.2 min in the presence of Pd@NHCS, while at the same period of time, the commercial Pd/C catalyst only reached 4% conversion. The Pd@NHCS could be recycled six times without catalytic loss. After six recycles the Pd nanoparticles were shown to be partially embedded in the nitrogen-doped shells. The presence of nitrogen-doped shells facilitated the prevention of migration and aggregation of the Pd nanoparticles [66-68] in that the particle sizes were almost unchanged after six cycles.

Overall, the use of core-shell structure under reduction conditions has been shown to be effective in high catalytic activity, preventing migration and aggregation, and enhancing the stability of the highly dispersed metal nanoparticles under reaction conditions.

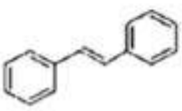
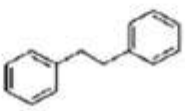
2.1.3.3.Hydrogenation reactions

Numerous catalysts (Rh, Pt, and Ni) have been encapsulated in a core-shell structure and hydrogenated in hydrogenation reactions [38, 69, 70]. For example, Ikeda *et al.* encapsulated platinum in mesoporous hollow carbon spheres (Pt@*hm*C) as a catalyst for hydrogenating various olefins (Scheme 2.1 and Fig 2.8) [37]. The catalytic activity of Pt@*hm*C in hydrogenation of various olefins was found to be superior to those of Pt supported by polyvinyl propylene (PVP) and activated carbon (AC).



Scheme 2. 1: Schematic illustration of olefin hydrogenation to form an alkane [15].

Table 2. 1: Catalytic activity comparison between Pt@hmC, Pt/PVP and Pt/AC [9].

Substrate	Catalyst	Product	t [h][b]	Conv. [%][c]
	Pt@*hm*C		2	> 99
	Pt–PVP		2	91
	Pt/AC		2	7
	Pt@*hm*C		2	96
	Pt–PVP		2	70
	Pt/AC		2	16
	Pt@*hm*C		1	91
	Pt–PVP		1	42
	Pt/AC		1	3
	Pt@*hm*C		15	72
	Pt–PVP		15	46
	Pt/AC		15	16

From this investigation it was concluded that the hollow structure of the carbon spheres contributes in enhancing the catalytic activity of a catalyst by protecting the platinum nanoparticle from aggregation and by rendering the internal void for reactions to take place in a hydrophobic environment, thus allowing for the enrichment of organic substrates near the surfactant-free nanoparticle surface [71].

2.1.3.4.Ficher-Tropsch reactions

The concept of performing Fischer-Tropsch synthesis (FTS) inside HCSs or nanoreactors was first reported by Tumelo *et al* [72]. In their study they reported the synthesis of two novel FT catalysts, Ru encapsulated in hollow carbon spheres (Ru@HCS) and Ru encapsulated in mesoporous hollow carbon sphere (Ru@MHCS). The catalysts were synthesised from hard template method using monodispersed silica spheres as a sacrificial template, a procedure proven to be invaluable in the synthesis of hollow nanoreactors [32, 47, 73].

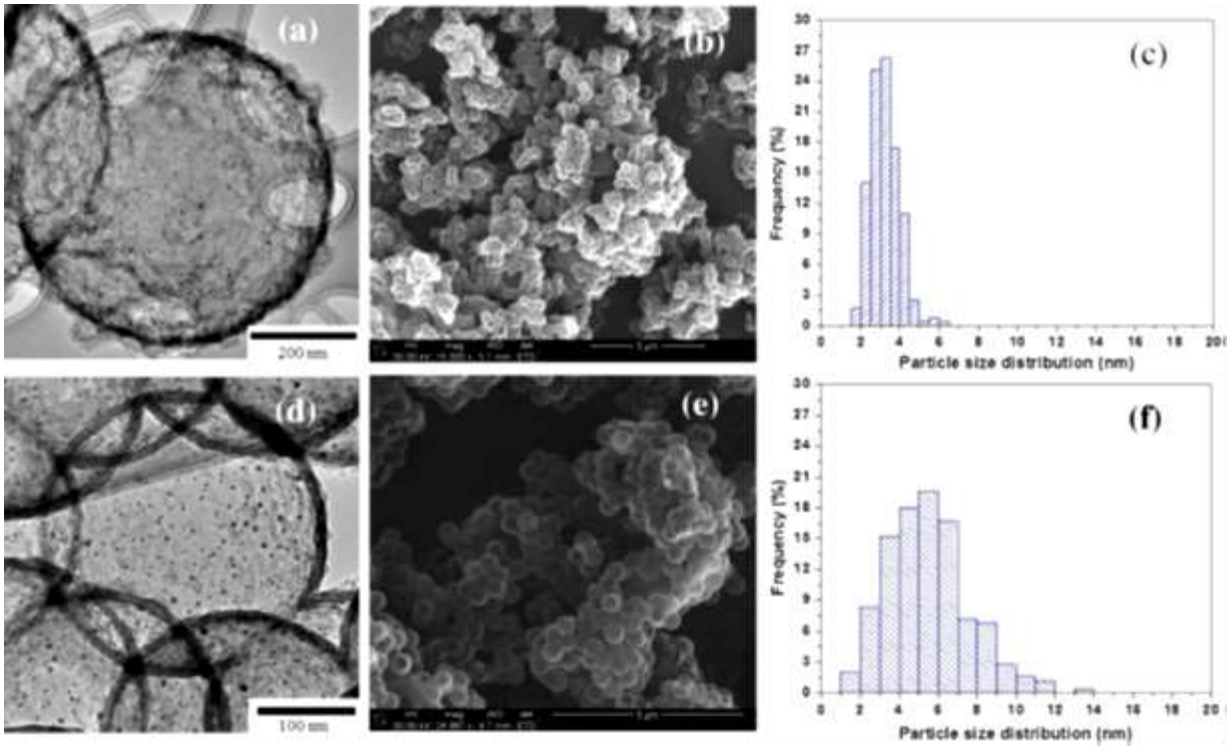


Figure 2. 8: TEM, SEM images and Ru particles size distribution of Ru@MHCS (a,b,c), and Ru@HCS (d,e,f).

Removal of the silica template gave Ru@HCS (d_{Ru} = 5.5 nm) and Ru@MHCS (d_{Ru} = 3.2 nm) that had carbon shells with different physicochemical properties (Figure 2.2). The HCS porosity of the shell allowed for access of reactants (syngas) and products (hydrocarbons) to enter and exit from the inside of the HCS; and it showed to affect the activity of the Ru FT catalyst encapsulated in the HCSs. Typical product selectivity associated with Ru nanoparticles was observed and the methane content increased with reaction temperature. No substantial Ru sintering occurred below 220 °C.

2.2. Osmium as a hydrogenation catalyst

2.2.1. Introduction

Os metal is lustrous, bluish white, extremely hard and brittle even at high temperatures. The Os has a very low compressibility and high bulk modulus and it is comparable to that of diamond, however, Os is softer than diamond [74, 75]. Os is an interesting material among noble metals in that it competes with iridium for being the densest known natural element. Os in nature occurs as an alloy osmoiridium or uncombined and most of the Os is obtained from wastes of a nickel refinery. The metal is a platinum group metal and it has the highest melting point and lowest vapour pressure of the platinum group metals. It is the densest naturally occurring element and the rarest stable element in the earth's crust with an estimated abundance of 0.05 parts per billion [76]. Os and its oxides have many properties and the metal is a demanding material to manufacture due to its scarcity. Os metal is usually alloyed with other noble metals for use in instrument pivots, electrical contacts, fountain pen tips and phonograph needles. Os powder reacts slowly with O_2 at 25 °C to give the volatile OsO_4 (the bulk metal requires heating to 397°C), which is a powerful oxidising agent that is quite toxic [77]. Osmium tetroxide causes lung, skin and eye damage. The metal must be used in a fume hood for safety precautions.

Generally OsO_4 is applied in organic chemistry as an oxidizing agent (e.g. in converting alkenes to 1,2 diols) and as a biological stain [77]. The chemistry of osmium has been studied extensively with a degree of interest shown in its tendency to form metal clusters [78].

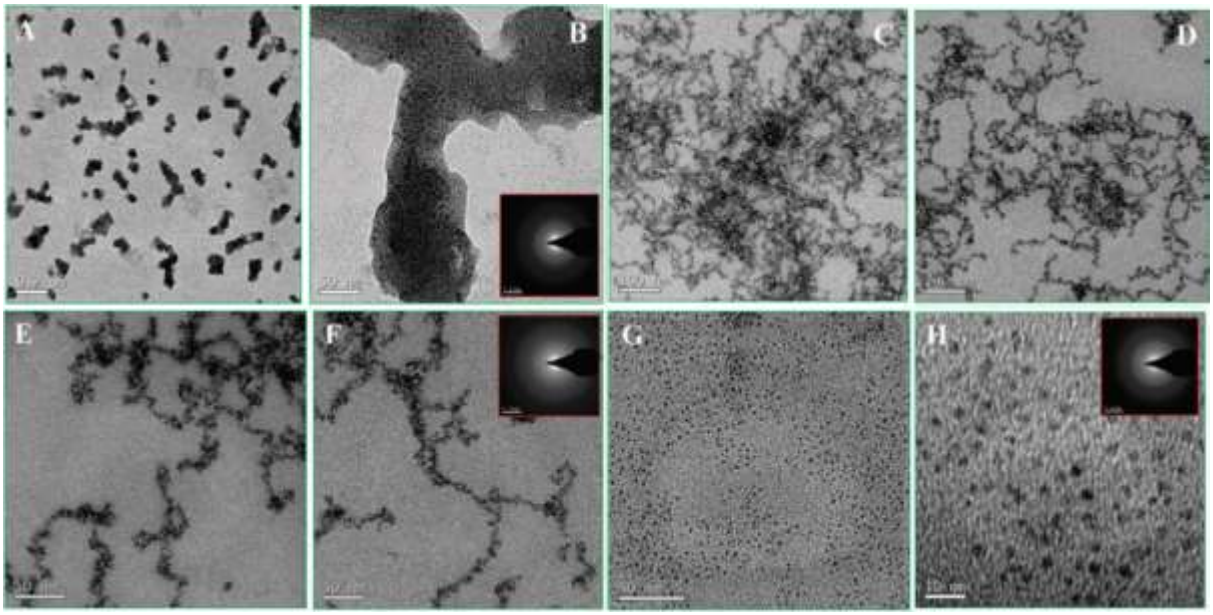


Figure 2. 9: Transmission electron microscopy (TEM) images of various shaped Os nanoparticles/nanoclusters. (A) and (B) show a low and high magnified TEM images of aggregated Os nanoclusters. (C) and (D) show a low magnified image of Os chain-like networks. (E) and (F) show a show a high magnified image of Os chain-like networks. (G) and (H) show a low and high magnified image of spherical shaped Os nanoparticles [23].

There are few reports of Os nanoparticles being prepared with different morphologies and sizes in the form of nano-clusters [24], nano-wires [25], wire-like aggregates [26], and thin films (Figure 2. 9). It is sometimes combined with other metals such as Pd or Pt using physical vapour deposition routes [79-82]. Lam and Gyenge synthesized a high performance Os nanoparticles electrocatalyst for direct borohydride PEM fuel cell anodes and concluded that Os nanoparticles provide similar activities to that of a PtRu catalyst [83]. Kim *et al.* utilized an MCM-48 template for the preparation of network Os and Pt metal 3d nanostructures [84]. Janiak *et al.* synthesized uniform Ru and Os nanoparticles by thermal and photolytic decomposition of their precursors under argon atmosphere [85]. Leskela *et al.* reported on the growth of Os thin films and nanoparticles by atomic layer deposition at 325-375℃ [86]. Doped thin film Os have been grown using various methods such as chemical vapour deposition (CVD) [79], the sol gel technique [87], vacuum pyrolysis [88], physical vapour deposition [89], etc. Coperet *et al.* synthesized silica supported Os nanoparticles by an organometallic route [90].

2.2.2. Catalytic application of osmium

Osmium metal has applications in both organic and inorganic chemistry. The Os metal is generally applied in organic chemistry as a strong oxidizing agent, widely used to oxidise alkenes into vicinol diols, and it is also applied as a biological stain. In inorganic chemistry the metal is less applied. However, a few studies have been conducted on applying the metal in (i) reduction reactions, (ii) fuel-cells, (iii) hydrogenation reactions, and (iv) hydrogenolysis reactions.

2.2.2.1. Os in organic chemistry

2.2.2.1.1. Oxidation of alkenes

Dihydroxylation is the process whereby diolate species are hydrolyzed to give cis-diols. The reaction is catalysed by OsO_4 where a cycloaddition between alkene and OsO_4 forms as an intermediate osmate etser which rapidly hydrolyses to give vicinal diol [91].

2.2.2.1.2. Biological staining

OsO_4 is used in transmission electron microscopy (TEM) and scanning electron microscopy (SEM) as a staining agent. In TEM studies the staining agent is used to improve image contrast in biological cells [92]. In SEM studies the staining agent is used as a lipid stain and an alternative to sputter coating. The staining agent works in that it embeds the heavy metal directly into cell membranes, thus causing a high electron scattering rate which improves the contrast. This effect is known in light microscopy as fixation. OsO_4 is the only fixing agent known which completely and easily fixes fats. Although dichromate can perform similarly with regards to lipid containing membranes and lipoproteins, the treatment takes several days; whereas OsO_4 accomplishes the same effect more effectively within a few hours.

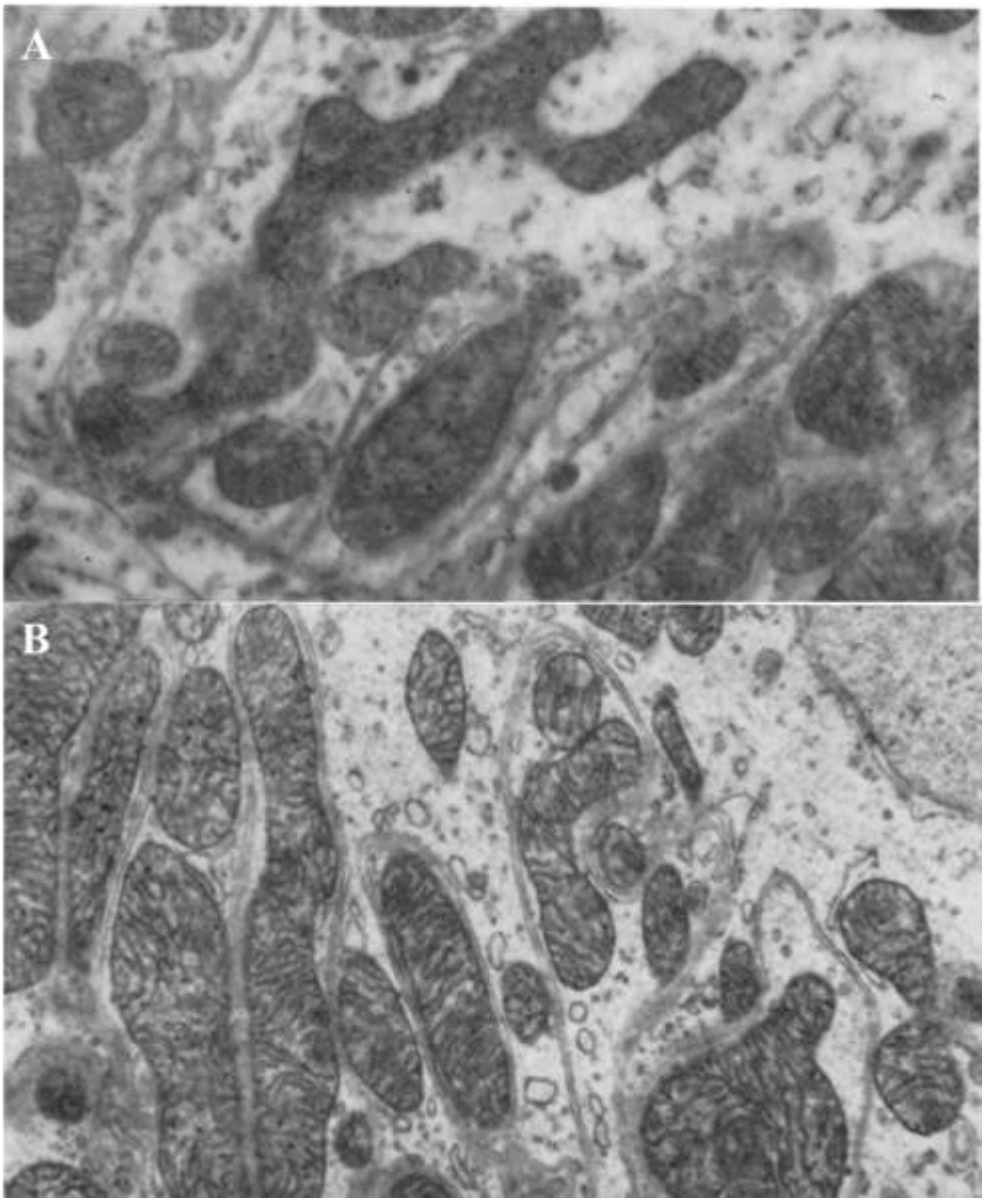


Figure 2. 10: TEM image of kidney tissue. (A) Shows a TEM image with no OsO_4 staining on kidney tissue. (B) Shows a TEM image of kidney tissue in presence of OsO_4 staining, note enhancement of contrast of mitochondrial cristae, mitochondrial dense granules, plasma membrane, and nuclear envelope [93].

Arnold *et al.* enhanced the contrast of a lipid containing membrane and droplets in OsO_4-fixed tissue with osmiphilic thiocarbohydrazide (TCH) [93]. The procedure was performed to enhance the contrast and consisted of a treatment of excess TCH where one end of the molecule attached to the Os in the tissue. This was followed by exposure to OsO_4 and more osmium was bound to the sites. The method uses the bridging phenomenon [24], whereby the contrast was

enhanced in the tissue components holding the most Os, i.e. osmiophilic components. Figure 2 (A) shows the reaction of excess TCH with lipid fixed. It is evident that subsequent treatment with OsO_4 resulted in attachment of more Os to the unreacted end of bound TCH to yield an increase in contrast (Figure 2.10 (B)). This method resulted in increased lipid density thus enhancing the contrast.

2.2.2.2.Os in inorganic chemistry

2.2.2.2.1. Reduction reactions

Even though Os is known as a strong oxidizing agent, several experiments have been conducted where Os has been involved in reduction reactions as a catalyst. Nithiyanantham *et al.* reported for the first time the synthesis of small size, self-assembled Os nanoclusters in DNA within a minute of microwave heating in the presence of ethanol [94]. The morphology of the particles was tuned by varying the molar ratios of DNA to Os salt and also by altering reaction parameters. The catalytic activity of the synthesised DNA-Os nanoclusters was examined for the reduction of 4-nitroaniline with excess $NaBH_4$.

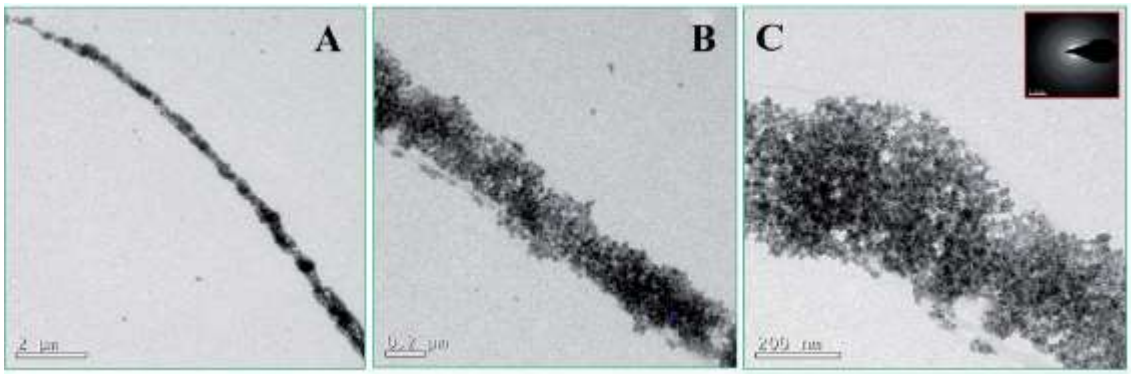


Figure 2. 11: TEM image of self-assembled Os nanoclusters in DNA. (A), (B) and (C) show the low and high magnification of DNA-Os nanoclusters having a wire-like morphology [71].

Figure 2. 11 shows the self-assembly of Os nanoparticles to Os nanoclusters. Figure 2. 11 shows the Os nanoclusters to have a wire-like morphology at various magnifications. The wire-like morphology was formed by the self-assembly of Os nanoparticles and their growth over the DNA chain. The average particle size of the nanoclusters was between 1 and 3 nm and that

of the wire-like morphology was ~ 290 ± 20 nm. The catalyst synthesised under reduction reaction of 4-nitroaniline was found to be larger in size compared to reports where Au or Ag nanoparticles were used [95-97].

Another study of reduction was performed on a hexavalent chromium (Cr^{6+}) ion using Os organosol as catalyst [82]. This catalytic reaction is important in that Cr^{6+} compounds are the most significant threats to the environment due to their extensive toxicity. The successive reduction of Cr^{6+} ions by thiosulphate in the presence of the Os organosol was conducted and monitored by UV-vis spectrophotometry. The Os nanoparticles acted as an electron carrier of thiosulphate to Cr^{6+}. The reduction of Cr^{6+} in presence of Os nanoparticles was found to be the fastest ever reported with a rate constant value of $1.3 \times 10^{-2} min^{-1}$ [82]. The catalyst could be recycled 7-10 times while retaining its catalytic activity.

Overall, the use of Os nanoparticles under reduction conditions has been shown to be effective and shows high catalytic activity and retention of catalytic activity for long period of time.

2.2.2.2.2. Fuel-cell electrocatalyst reactions

A high performance of Os nanoparticle electrocatalyst as a direct borohydride PEM fuel cell anode has been reported by Lam and Gryenege [98]. A direct nonhydrogen polymer electrolyte membrane (PEM) fuel cell is advantageous compared to hydrogen fuel cells due to simpler fuel storage and delivery infrastructure issues. In their study they have performed a comprehensive comparative study of Pt, PtRu and Os nanoparticles, where the Os/C synthesized by the Bönneman organosol method and supported on Vulcan XC-72R was shown to be electrochemically active, highly stable and cost efficient catalyst when compared to Pt and PtRu alloys for BH^-_4 oxidation. At room temperature the Os/C electrocatalyst gave a high open circuit and operating voltage of $E_{cell} \geq 9$ V in the kinetic region. Furthermore in polarization regions where mass transfer effects can be predominant, the PtRu/C and Pt/C electrodes performance decayed quickly, while that of Os/C gave excellent performance.

From this study Os nanoparticles have shown to be electrochemically active, highly stable and a cost efficient catalyst compared to direct fuel cells when using carbonaceous fuels. The borohydride cell has an advantage over direct fuel cells in that it does not involve CO_{ad} poisoning and shows a less-severe cathode mixed-potential-related effects due to crossover [98].

2.2.2.2.3. Hydrogenation reactions

Few reports are available in literature regarding the use of osmium cluster and nanoparticles in hydrogenation reactions. One example is the triosmium carbonyl cluster supported on Al_3O_4 that has been reported by Nozinger and Hao to be a hydrogenation catalyst [27, 98-101]. The Al_2O_3 support was chosen because the Os catalyst showed the ability to be active in CO hydrogenation reaction, giving methane as the product [98]. Os clusters have been used in hydrogenation reaction fuels as the hydrogenation of ethane, carbon monoxide, carbon dioxide, and the hydrogenolyses of ethane [102, 103]. In CO hydrogenation the catalyst has been reported to produce alkenes and alkanes [104] and to give low conversions of only $C_1 - C_4$ hydrocarbons. The results obtained were conducted at pressure of 7.9 x 105 $N.m^{-2}$ and the catalyst showed a slow loss of catalytic activity which was believed to be due to the formation of carbonaceous deposits on the catalyst surface (figure 2. 12).

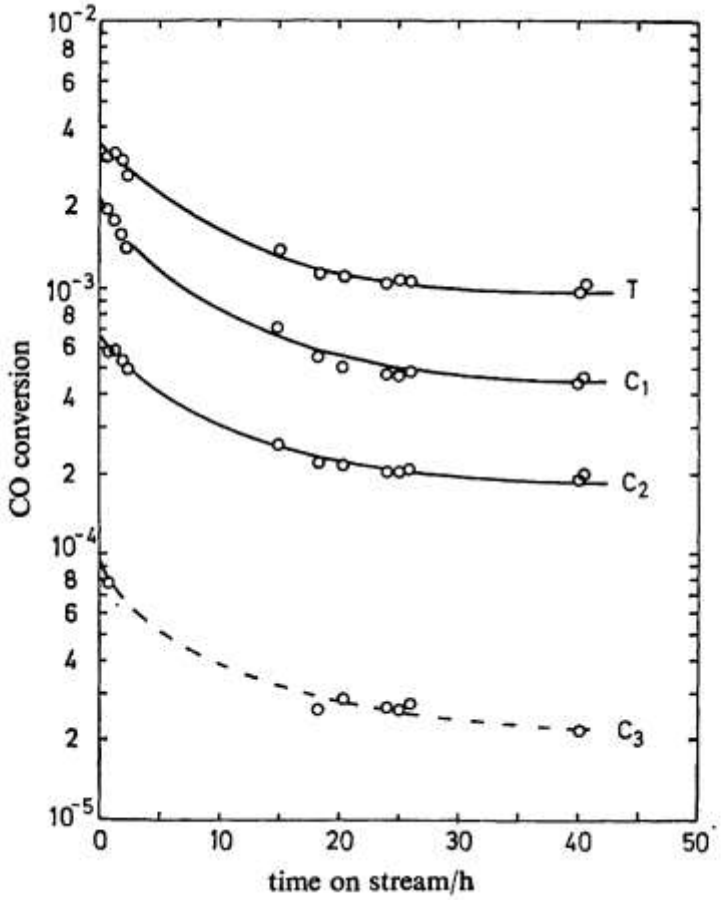


Figure 2. 12: CO conversion catalysed by $Os_3(CO)_{12}/Al_2O_3$ – reactant, $He:H_2:CO$ = 1:3:1, total pressure: 7.9 x 105 $N.m^{-2}$, temperature: 573 K, mass of catalyst: 0.1651 g, Os content: 0.24 wt%, feed flow rate: 166 scc min^{-1} (T = total conversion) [104].

Another study by Jackson *et al.* showed that the chemistry of an Os cluster catalyst was insensitive to oxygen and air poisoning [105]. The catalyst cluster could be removed from the reactor, exposed to air, replaced in the reactor and the reaction would still continue at the same rate as before without any induction period. The reason for such insensitivity was related to the strength of oxygen adsorption on the osmium clusters. Another general aspect of such catalytic chemistry was the non steady-state system. When the reactant mixtures were passed over the catalyst there occurred a period of non steady-state behaviour [105]. During the non steady state behaviour, carbonaceous material was deposited on the catalyst and maximum activity of the catalyst was reached when the amount deposited was equal to the number of sites. This was interpreted as a hydrogen-transfer reaction. The decrease in activity was due to site blocking effects and steric hindrance as the deposition continued. A shift in frequency of CO bond to Os

in the infrared spectrum was also observed due to electron-density being transferred from the support to the Os [105]. Therefore a large transfer of electron-density led to a C=O bond being weakened and an Os-C bond being strengthened. This affected the catalytic activity by changing the strength of adsorption brought by variation in the electron-density. The large electron-density transfer resulted in strong chemisorptive bonding which gave a low catalytic activity. As the amount of electron-density transferred decreased the activity increased with reduction in strength of adsorption until a maximum was reached. As the reduction in strength increased it led to a reduction in concentration of the reactive species and thus subsequent reduction in activity.

Table 2. 2: A comparison of activation energies (a) and reaction rates (b) [66].

Catalyst	Reaction			
	$C_2H_4 + H_2 \rightarrow C_2H_6$[(c)]		$CO + 3H_2 \rightarrow CH_4 + H_2O$[(d)]	
	Ea	$\log_{10} r_{605}$	Ea	$\log_{10} r_{605}$
$H_2Os_3(CO)_{12}/Al_2O_3$	42(378-406K)	0.25	114(485 – 561K)	0.03
$Os_3(CO)_{12}/Al_2O_3$	50(390-500K)	-1.65	95(540 – 645K)	-3.21
$Os_3(CO)_{12}/TiO_2$	44(355-390K)	-0.15	93(485 – 570K)	-0.62
$Os_6(CO)_{18}/SiO_2$	41(385-425K)	-0.09	73(590 – 665K)	-0.32
$Os_6(CO)_{18}/TiO_2$	45(325-425K)	-0.54	80(465 – 605K)	-2.00
$H_2Os_{10}C(CO)_{24}/Al_2O_3$	53(520-590K)	-2.25	122(520 – 590K)	-1.07
Os/Al_2O_3	35(290-320K)	[(e)]	119(500 – 560K)	-0.09

Ea in KJ/mol

Rates in μmol/s/g catalyst

(c) C_2H_4: H_2 ratio 1: 1

(d) CO:H_2 ratio 1:3

The hydrogenation of ethene over Os cluster catalysts on different support (Table 2) indicated that higher temperatures were required than those found for conventional catalysts; similarly

the activation energies were also higher than those found with a conventional osmium catalyst (Table 2). The adsorption of ethene on Os cluster catalyst was weak and this was seen by the positive orders of reaction for the clusters compared with zero order for a conventional catalyst. Hence higher temperatures were required for the catalyst to obtain measurable rates from a low steady-state concentration of adsorbed ethene. Therefore, the hydrogenation of ethene over an Os cluster catalyst was similar to that of a CO poisoned conventional Os catalyst.

The hydrogenation of CO over the osmium cluster catalysts was similar to that of conventional catalyst in that the activation energies were similar as were the products (methane and CO_2) (Table 2). However, the Os cluster catalysts activity was significantly lower than its conventional counterparts. The carbonyl ligands were retained throughout the hydrogenation reaction and these results may suggest that on a conventional catalyst there was a significant proportion of inactive CO present on the surface of the catalyst during the hydrogenation reaction.

2.2.2.2.4. Hydrogenolysis reactions

Hydrogenolysis catalytic active Os nanoparticles were prepared by an organometallic approach and narrowly dispersed on silica support [106]. In this study the Os nanoparticles were prepared from [osmium(0) (η^4-1,5-cyclooctadiene)(η^6-1,3,5,7-cyclooctatetraene)], Os(cod)(cot) [107]. The Os nanoparticles chemisorptive properties, and an evaluation of the catalyst catalytic activity in alkane hydrogenolysis was performed. The method used to load the Os on the silica support was impregnation. The ligands of the dispersed Os(cod)(cot) on silica were removed upon mild H_2 treatment at 573 K. The formation of fully reduced Os nanoparticles, which was converted into OsO_2 upon exposure to air, were confirmed by the shift of the Os XPS peaks (Os $4f_{7/2}$ and $4f_{5/2}$) (figure 2. 13) [108, 109].

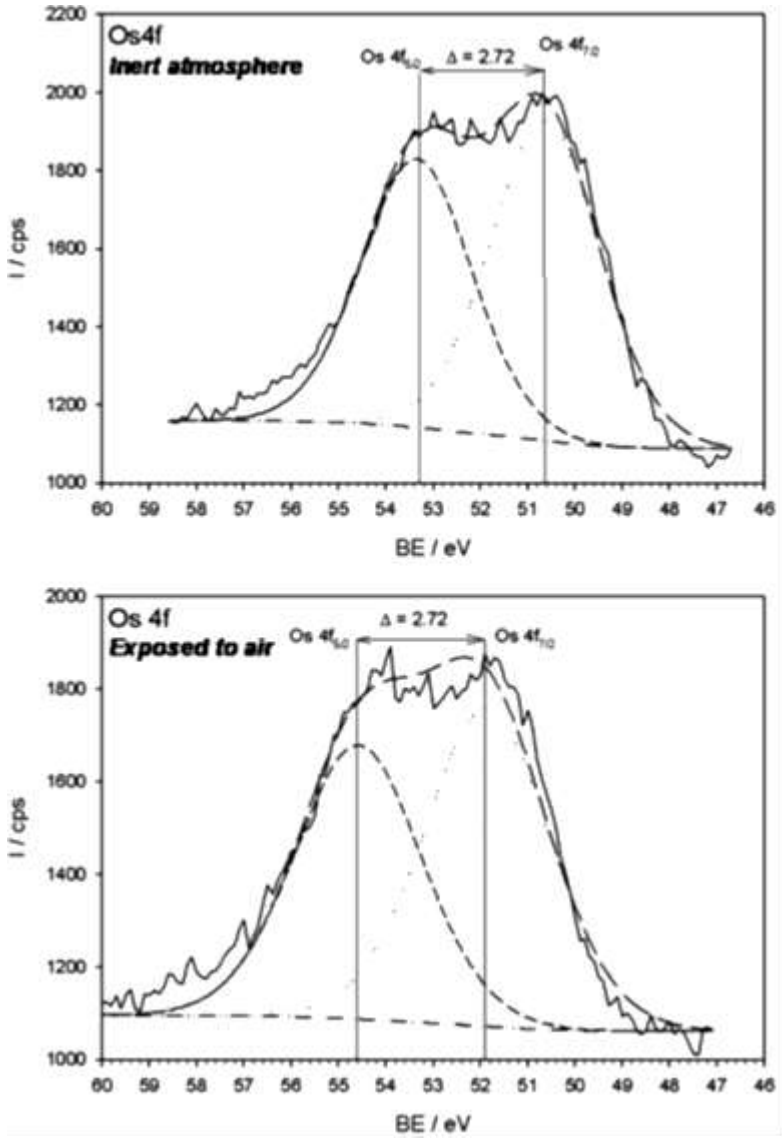


Figure 2. 13: Deconvolution of the Os 4f XPS spectra of pristine Os/SiO_2 (top) and after air exposure (bottom) [65, 66].

High-angle annular dark-field scanning transmission electron microscopy (HAADF-STEM) was performed on Os/SiO_2 exposed to air which revealed the presence of small OsO_2 particles as suggested by XPS. The mean Os dispersion on silica was 73% and the average particle size of Os was 1.1 $\pm$0.3 nm and corresponded to *ca.* 90 atoms (figure 2. 14).

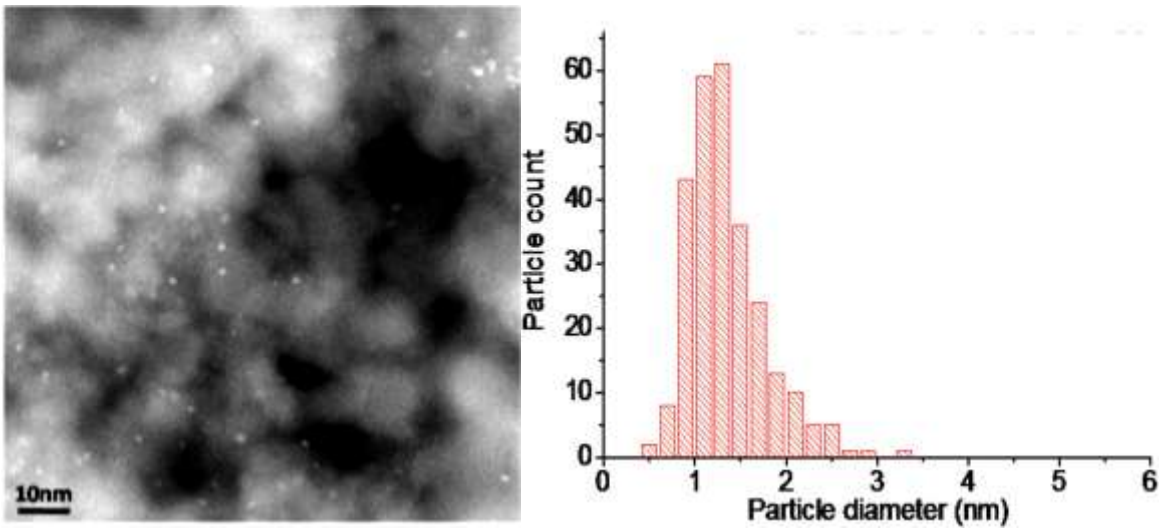


Figure 2. 14: (a) Representative HAADF-STEM micrograph of Os/SiO_2 after exposure to air. (b) Particle size distribution of the Os [106].

The catalytic activity of the catalyst was conducted on the hydrogenolysis of ethane and butane. The butane was converted into a mixture of methane, ethane and propane under reaction conditions of 660 mbar H_2 at 423 K. The catalyst selectivity was 60 and 40% to CH_4 and C_2H_6, respectively. The hydrogenolysis of pure ethane under the same reaction conditions was found to be three orders of magnitude slower. Overall from the investigation it was concluded that the hydrogenolysis of butane occurred most likely through a dimetallacylopentane intermediates, as in the case of Ru/SiO_2 [89].

2.3. Fischer-Tropsch synthesis

2.3.1. History and background

The catalytic reaction of hydrogenation began early in 1823 when it was discovered by Dobereiner that finely divided platinum led into spontaneous burning of hydrogen in air [110]. From such findings five decades later, scientists began to delve into investigating a wide range of metals and their catalytic properties; these metals were iron, copper, platinum group metals etc. In 1902, the discovery of carbon monoxide hydrogenation to form methane over a transition metal (Ni or Co) catalyst at temperatures of 180-200 ℃ was discovered by Sabatier and Senderens which laid the foundation of XTL technology (X = coal, gas, biomass; T = to; L = liquid) [111-113]. This technology is the precursor of the Fischer-Tropsch synthesis which began in 1913 by the German company BASF (Badishe Anilin und Soda Fabrik) when it patented the preparation of hydrocarbons and oxygenates by hydrogenation of carbon monoxide (CO) over a Co catalyst [3, 113-116]. Further development of the process was conducted by Franz Fischer and Hans Tropsch at the Kaiser Wihelm Institute in 1923 by synthesising aliphatic oxygenated compounds from CO hydrogenation over alkalised Fe chips at 400 ℃ and 150 bar pressure. The reaction was then named the Fischer-Tropsch synthesis (FTS) which also applies in the synthesis of a broad range of hydrocarbon products (e.g. petrol, diesel and heavy oils) [117]. A few years later Otto Roelen who worked with Fischer and Tropsch at the Wilhelm Institute developed an industrial synthesis of aldehydes from carbon monoxide and alkene using Co, the now called homogeneously catalysed hydroformylation process [113].

In the 1920s access to petroleum became essential for industrial nations and had a positive impact on their economies. The mass production of automobiles, airplanes and ships which were powered by petroleum contributed to an increased demand for liquid fuels as a major source of energy, compared to wood and coal [118].

Around 1927, scientists gathered together to solve chemical engineering problems associated with the FTS and a series of fixed bed reactors were developed under the supervision of Roelen. After the development of new reactors a FT process license was obtained in 1934 by Ruhrchemie. In 1936 the first four coal-based FT plants were commissioned in Braunkohle-Benzin, Germany and they had a capacity of about 200 000 tons of hydrocarbons per year

[116]. Two years later Germany had a total of 9 commissioned coal-based FT plants in operation with a combined total capacity of 660 000 tons per year [119]. The plants operated by using a Co and Fe catalysts to convert CO/H_2 to fuels [118].

The Fischer-Tropsch process went from lab scale to a full scale multiple plant operation in Germany and this development impacted on World War II. The demand for FT fuels led to new production technologies and improved catalysts and reactors. In early 1944, the synthetic fuel capacity of Germany was 14 675 tons per day. After World War II new oil reserves were discovered in the Middle East and this decreased the demand for fuels and chemicals made from the FT process [119]. However in the 1950s USA had a shortage of petroleum which caused the country to focus on alternatives of petroleum and hence the first coal-to-oil processes was investigated. In 1953 a fluidised-fixed-bed reactor that converted syngas from CH_4 over a Fe catalyst to produce fuels and chemicals was developed by Hydrocarbon Research in Trenton, New Jersey and this reactor was installed in Brownsville Texas. After a while the plant was shut down due to an increase in the price of methane.

After World War II Arbeit-Gemeinschaft Lurgi and Ruhrchemie (ARGE) developed a fixed-bed FT reactor which operated in large scale processes. Carthage Hydrocol Inc. developed a FT technology reactor based on a circulating bed [4]. During the period of apartheid South Africa was internationally isolated and this led to the implementation of both these processes by Sasol. The country had few oil reserves but the abundant coal reserves allowed for the generation of cheap syngas. In 1951 Sasol began to construct its first coal to synthetic fuels plant in Sasolburg using FT technology. In 1955 Sasol began to market its petroleum products and chemicals using the FT technology. [111, 119]. The increase in oil price and the oil embargo by the Organisation of Petroleum Exporting Countries (OPEC) in 1970s led to renewed interest and intensive research and development programs in the FT process in many countries [120]. In South Africa, two new Sasol plants were designed and built in record time, in 1980 and 1982, and these plants were situated in Secunda [3, 113, 119, 121].

Today the FT process is commercialised worldwide and many patents have been registered on aspects of the FT process. The FT process has been invested by oil companies to develop the synthesis of clean fuels and it also showed promise in the energy industry due to the economic utilisation of natural gas and coal to make environmentally clean liquid fuels and chemicals. Countries such as China and the Middle East make use of this process since they have large reserves of coal and oil.

2.3.2. Fischer-Tropsch synthesis

The Fischer-Tropsch synthesis (FTS) is the catalytic conversion of syngas to higher hydrocarbons, predominantly olefins, paraffins and alcohols. In industry the process is broken down into three stages: (i) syngas production/gasification from a carbon source (coal, natural gas and biomass), (ii) FTS, (iii) product workup and separation. The overall process is summarised in Fig. 1.1 [122].

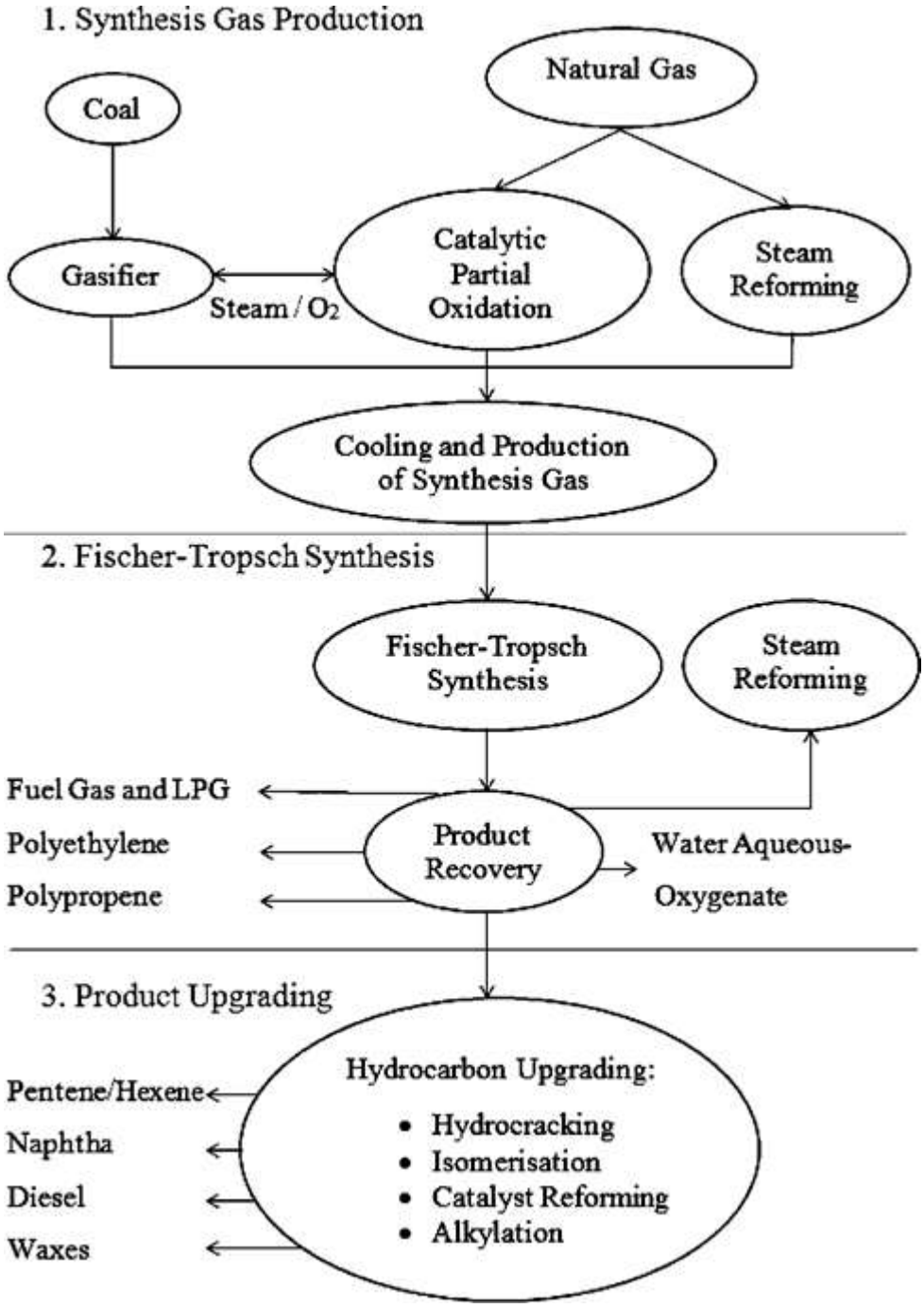


Figure 2. 15: Three stages in Fischer–Tropsch process [123].

The syngas production is done by gasification and steam reformation of coal, biomass or natural gas. The syngas (CO and H_2) is purified by removing sulphur and other impurities and then the CO/H_2 is piped into a reactor for FTS where a variety of catalytic reactions occur, resulting in a range of products such as fuel gas, ethylene, propene, liquefied petroleum gas (LPG), etc. The products obtained are further separated into different components.

2.3.3. Fischer-Tropsch chemistry

The following equations describe the FTS chemistry:

Reactions to produce paraffinic hydrocarbons

$$(2n + 1)\ H_2 + nCO \rightarrow C_nH_{2n+2} + H_2O \quad (2.1)$$

$$(n + 1)\ H_2 + 2nCO \rightarrow C_nH_{2n+2} + nCO_2 \quad (2.2)$$

Reactions producing olefinic hydrocarbons

$$2nH_2 + nCO \rightarrow C_nH_{2n} + H_2O \quad (2.3)$$

Reaction producing alcohols

$$2nH_2 + nCO \rightarrow C_nH_{2n+2}O + (n - 1)\ H_2O \quad (2.4)$$

Depending on the type of catalyst used, in addition to the above equations, side reactions also occur, such as the following:

Water Gas Shift (WGS) reaction is the main source of carbon dioxide production

$$H_2O + CO \rightarrow CO_2 + H_2 \quad (2.5)$$

Boudouard reaction (carbon deposition)

$$2CO \rightarrow C + CO_2 \quad (2.6)$$

Bulk carbide formation

$$yC + xM \rightarrow MxCy \quad (2.7)$$

Catalyst Oxidation-Reduction

$$yH_2O + xM \rightarrow MxOy + yH_2 \quad (2.8)$$

$$yCO_2 + xM \rightarrow MxOy + yCO \quad (2.9)$$

The FTS is both a hydrogenation and polymerisation reaction with a product distribution described statistically by the Anderson, Shultz and Flory (ASF) kinetic model [124, 125].

2.3.4. Fischer-Tropsch synthesis product distribution

The FTS consists of a wide range of multicomponent mixtures of hydrocarbon and oxygenated products via primary and/or secondary reactions. The 1-olefins are primary reaction products produced from the iron catalysts whereas n-paraffins are formed at a lesser degree than olefins which can possibly be reincorporated into chain growth, isomerised or hydrogenated to 2-olefins [126]. The selectivity of the various products is generally controlled by kinetic and mechanistic factors associated with various reactions occurring during FT synthesis [127]. The spread in carbon number products is dependent on the following parameters: the operating temperature and/or pressure, the type of catalyst, the type or amount of catalyst promoter, the feed composition and the type of reactor [7]. The FT chain growth is assumed to occur by the stepwise insertion of $-CH_2-$ monomers chemisorbed on the catalyst metal surface [122, 128]. The following are steps assumed in chain growth and termination:

$$\text{Desorbed from the catalyst surface into forming } C_2H_6 \quad \text{(i)}$$

$$-CH_2- + -CH_2 \rightarrow C_2H_4 + H_2 \rightarrow C_2H_6 \quad \text{(ii)}$$

$$+ CH_2 \rightarrow C_3H_6 \quad \text{(iii)}$$

The termination steps are (i) and (ii) with a probability of chain termination defined as $(1-\alpha)$ whereas chain growth is slowed in step (i) with a probability defined as alpha (α). The chain growth probability increases with an increase in α value. A mathematical model based on the mass balance for the FT reaction demonstrates the chain growth concept is the Anderson, Shultz and Flory (ASF) distribution [114]:

$$\log\left(\frac{Wn}{n}\right) = n\log\alpha + \log[(1-\alpha)^2 / \alpha] \quad 1.10$$

Where - W_n = mass fraction of product

n = number of carbon atoms in the hydrocarbon chain

α = chain growth probability

The alpha value ranges between 0 and 1 and the greater the alpha value the greater the selectivity in forming waxy products, whereas, a low alpha value implies a selectivity to forming gaseous products.

The following plot of log (W_n/n) against n, figure 2. 16, should theoretically give a linear line with a slope of log α. From this plot α can be calculated.

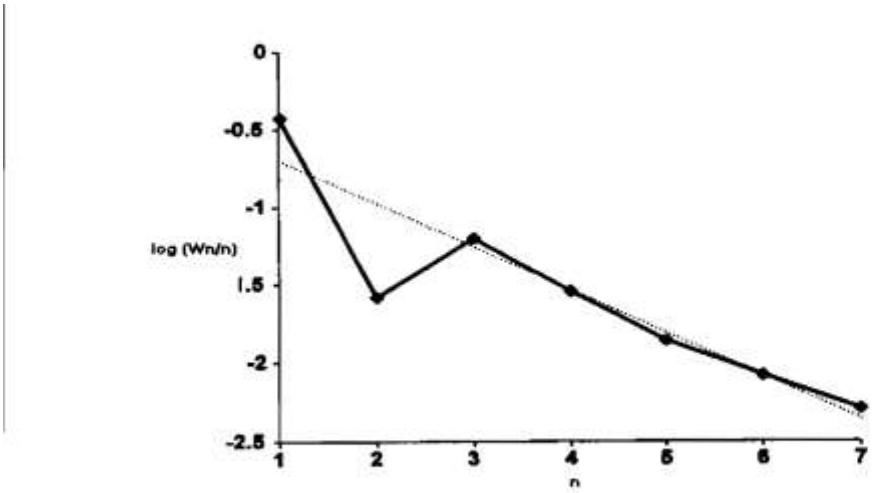


Figure 2. 16: Plot of log (W_n/n) against n illustrating the ASF distribution [129].

In practice the FT distribution deviates from the ideal distribution, in particular for methane, C_2, and higher molecular weight products [126, 130-134]. The carbon range between C_3-C_{12} usually gives a linear line implying a constant α value known as α_1. If a significant amount of waxes is produced the ASF plot shifts to yield another α value (α_2) for the high boiling hydrocarbons. The existence of two α values means that the value of α increases with chain length [134].The higher boiling products are in the liquid phase under reactor conditions as the product is found to condense in the catalyst pores.

The possibility of two α values being found may be due to diffusional restrictions of liquid products (alkenes) which become entrapped in the catalyst pores. Therefore the liquid products spend longer time in a reactor compared to lighter vapour phase products which results in re-incorporation [135].

The following are the possible reasons for diffusional restriction of long chain products spending more time inside the catalyst pores or particles: slower diffusion rates, higher solubility in the liquid phase and stronger physisorption of the longer chain products [136].

2.3.5. Fischer-Tropsch reaction

The FT reaction is a highly exothermic, heterogeneous catalysed polymerisation reaction that converts syngas into a wide range of products (hydrocarbons and oxygenates) according to the following stoichiometric equation:

Formation of paraffins: $(2n+1)H_2+nCO \rightarrow C_nH_{2n+2}+ nH_2O$ $-\Delta_{rxn}H$ (230 °C) =210-160kJ/mol_{CO}

Formation of olefins: $2nH_2+nCO \rightarrow C_nH_{2n} +nH_2O$ $-\Delta_{rxn}H$ (230 °C) =110-150kJ/mol_{CO}

The heat of reaction per mol of CO converted varies due to the decrease in the thermodynamic stability of hydrocarbons with increasing chain length of the products. The heat of reaction to form low molecular mass olefins is less than that of the corresponding paraffins. The FTS products vary with temperature. For example a low temperature reaction results in long chain hydrocarbons and a high temperature reaction results in short chain hydrocarbons. Industrially the temperature change results in two operating modes called high temperature Fischer-Tropsch (HTFT) operated around 340 °C and low temperature Fischer-Tropsch (LTFT) operated around 230 °C [7, 119, 137]. The consequences of HTFT are increased selectivity of the undesired methane and also an increase in deposition of carbon, which is found to result in catalytic particle sintering [114]. The HTFT mode uses an iron based catalyst which produces gasoline and low molecular mass olefins ranging from $C_2 - C_{15}$ [7, 119, 137]. The LTFT mode uses iron-based or cobalt-based catalysts to produce high molecular linear waxes that can be converted into high quality diesel oil [115]. Table, 1.1, shows the distribution of products from LTFT and HTFT processes [138].

Table 2. 3: Typical product selectivity from two Sasol processes [138].

Product (wt%)	LTFT	HTFT
CH_4	4	7

C_2 to C_4 olefins	4	24
C_2 to C_4 paraffins	4	6
Gasoline	18	36
Middle distillate	19	12
Heavy Oils/waxes	48	9
Oxygenates	3	6

2.3.6. Fischer-Tropsch reaction mechanism

Numerous FT reaction mechanisms have been proposed in order to explain the FT product formation. The mechanisms proposed are assumptions based on product distributions and that catalyst metal crystallites consists of multiple active sites [139]. These mechanisms are based on whether the formation of an oxygen containing intermediate is achieved by hydrogen addition to the adsorbed CO first or if the C-O bond splits first. The plausible mechanisms that have been proposed with different intermediates are the carbide (alkyl), vinyl/alkenyl, oxygenate (enol) condensation and CO insertion mechanisms [127, 140].

Possible steps for FT polymerisation include [141]:

- adsorption of CO – initiation
- splitting of the C-O bond
- dissociative adsorption of $2H_2$ Intermediate
- transfer of 2H to the oxygen to yield H_2O
- desorption of H_2O
- transfer of 2H to the carbon to yield CH_2
- formation of a new C/C-bond
- desorption of products – termination

2.3.6.1.The methylene Insertion (carbide and alkyl) mechanism

This mechanism was originally proposed by Fischer and Tropsch in 1926 and was later modified by Pettit and Biloen [142]. In their theory CO is chemisorbed on the surface of the activated metal surface, followed by C=O cleavage due to hydrogenation to give an aldehyde group attached to a metal, followed by condensation and further hydrogenation and hence chain growth [143, 144]. The theory, mentioning the formation of a metal carbide, was later discarded because no carbide phases were found in the ruthenium and cobalt catalysed FT synthesis [119]. The corrected mechanism postulates that CO is coordinated on the surface of the activated metal surface, followed by C – O cleavage and hydrogenation to give sequentially surface carbide ($C_{(ad)}$), methylidyne ($CH_{(ad)}$), and methylene ($CH_{2\ (ad)}$) species [145]. The methylene product could further be hydrogenated to surface methyl ($CH_{3(ad)}$) and finally be released as methane [145].

The alkyl mechanism involves the CH_3 as the chain initiator and the insertion of CH_2 species as the chain monomers to lead to growth of the chain [145]. The chain growth termination is believed to occur by either β-hydrogen abstraction or hydrogen addition to give α–olefins or n-parrafins as the primary reaction products [128]. The alkyl mechanism does not allow for branch formation to occur, however, it has been suggested that branched molecules form by re-adsorption of olefins such as propene [146].

2.3.6.2.The vinyl/alkenyl mechanism

In this mechanism the dissociation of chemisorbed CO and subsequent hydrogenation of the surface carbon yields surface methyne (=CH) and methylene ($=CH_2$) monomers which react further to form vinyl (-CH=CH2) groups which serve as the chain initiators on the active phase surface [147]. The surface methyne monomers can also react with the vinyl species resulting in a step-wise polymerisation reaction to give chain growth and formation of allyl ($-CH_2CH=CH_2$) species which can form isomers. The vinyl and the alkyl mechanism are similar because they both explain the synthesis of branched hydrocarbons. [148, 149].

2.3.6.3. The oxygenate mechanism

The enol condensation mechanism was first proposed by Storch, Golumbic and Anderson in 1951 [150] and it involves the chemisorption of CO, which reacts with the adsorbed hydrogen to give enolic surface monomers. The chain propagation is suggested to occur via condensation. Then chain termination gives either α-olefins or oxygenated products. The hydrogenation of α-olefins yields n-paraffins and the termination occurs by hydrogenation [127, 140].

2.3.6.4.The CO insertion mechanism

In this growth mechanism the surface CH_3 species initiates the reaction. Pichler and Shulz suggested the chain growth occurs with the chemisorbed CO as the monomer [151]. The chain propagation is achieved via insertion of the chemisorbed CO on the surface of the metal alkyl bond, followed by hydrogenation to form the products (oxygenates or alkenes) [127, 152].

2.3.7. Fischer-Tropsch catalysts

In Fisher-Tropsch synthesis the common feature of all the catalysts is their strong interaction with CO and their ability to dissociate adsorbed CO. The catalytically active site of the metal and CO interaction should neither be too strong nor too weak, since this would result in formation of methane and thus no chain growth of hydrocarbon would occur [153]. The most commonly used catalysts are the group 8-10 metals of the Periodic Table [3, 4]. Although much attention has been paid in recent years to the use of group 8-10 metals as hydrogenation catalysts, comparatively little work has been done with osmium. In this study focus osmium is the metal investigated in FTS. Few reports have been conducted on Os as a hydrogenation catalysts (see *section 2.2.2.2.3*). The specific activity of these metals (supported on silica) for methane formation was reported to decrease in the following order:

Ru > Fe > Ni > Co > Rh > Os > Pt > Pd > Ir [150, 154]

From these metals only Fe, Ni, Co, and Ru have the required catalytic activity for commercial or industrial application. Ni produces too much methane and the Ru is economically unfeasible and a rare metal, thus, on a commercial scale Fe and Co are used. Os, like Ru is a rare metal and its high price also limits its commercial application as a heterogeneous catalysts [78].

From literature as mentioned earlier, less work has been done on osmium in investigating its catalytic activity in FTS. Choplin Leconte *et al* reported the first work done on Os/SiO_2 tested at 250-300 ^0C and 1 bar (H_2/CO =1:1) in FTS and the products formed were C_1-C_5 hydrocarbons [22]. In Os-FT catalyst reaction, methane was largely formed (70%) [22]. A standard Os/SiO_2 is approximately 100 times less active compared to Ru/SiO_2 in FTS [78]. The overall activity of Os in FTS is low compared to the conventional catalysts.

Table 2. 4: Comparison of Co, Fe and Os as catalysts for the FT reaction [137].

Parameter	**Cobalt catalysts**	**Iron catalysts**	**Osmium catalysts**
Cost	$ 210/Kg	$ 1.43/Kg	$ 13 000/Kg
Deactivation	Deactivation by carbon deposition identified as most serious → reversible by catalyst regeneration	Re-oxidation and sintering of metal crystallites by water → not commercially reversible	N/A
Productivity at high conversion	Higher, less significant effect of H_2O on the rate of CO conversion	Lower, strong negative effect of H_2O on the rate of CO conversion	Very low, less to no effect of H_2O on the rate of CO conversion
CO conversion to CO_2	Not very significant, more noticeable at high conversions	Significant	Not significant

Tolerable sulphur content	1-2 ppb	1-2 ppm	N/A
Flexibility (Temperature and Pressure)	Less flexible, significant influence of temperature and pressure on hydrocarbon selectivity	Flexible, methane selectivity is relatively low even at 613K	Flexible, methane selectivity
H_2/CO ratio	~2	0.5-2.5	~2

Overall the Co catalysts are more favourable compared to the Fe in terms of selectivity and production of long-chain hydrocarbons in LTFT processes because of their stability, higher per pass conversion [138], higher productivity at high conversion [7, 155], and low/no water gas shift activity [156].

2.3.8. Fischer-Tropsch catalyst supports

FTS utilizes a heterogeneous catalyst and the catalytic reaction occurs on the surface of the active metal. The metal surface area is increased by depositing small metal particles on a suitable support material which maximises metal utilisation and in turn increases the specific activity [157].

Advantages of using a support for an FT catalyst include the following [158, 159]:

- Reduces/retards metal sintering
- Enhances the reducibility of the active metal
- Increases the catalyst resistance towards catalyst poisoning

- Limiting unwanted pressure drop in fixed bed reactors during FT synthesis
- Produces large active metal surface area
- Allows easy flow of feed gas through the reactor and catalyst pores
- Produces cheaper catalysts
- Support material may act as a catalyst promoter to the supported metal

The metal supports for FT reaction are usually silica, alumina, titania and various shaped carbon materials [160]. Selection of a support is based on characteristics which are suitable for particular catalyst and reaction conditions, which includes: mechanical strength; stability under reaction conditions; appropriate physical form for the given reactor; high surface area; porosity and chemical nature [161]. The supported catalyst consists of the following components: (1) a support material, which carries the active metal, (2) a promoter, which may be Pt, Ru or Re for cobalt catalyst and Na, Li, K and Rb for iron catalyst and (3) the active catalyst metal [7, 119, 162].

2.3.8.1.Carbon support

Carbon is an important element in that it occurs in all life forms and it forms the basis of organic chemistry. The six well known allotropes of carbon are diamond, graphite, carbon nanomaterials, fullerenes, and amorphous carbon. The carbon material exploited in catalysis is generally used as a catalyst support to anchor the catalyst particles on a substrate. Carbon does not exhibit solid acid-base properties and it is resistant to acidic and basic media [160, 163, 164].

The carbon based material is unique in that it has many possible electronic states as a result of carbons ability to show sp, sp^2 and sp^3 hybridisation. The phase diagram of carbon under ambient conditions is mostly stable in the sp^2 phase [165]. Under high pressure and high temperature the carbon material transforms into a stable sp^3 phase (diamond) and when the pressure drops the diamond slowly reconverts to a thermodynamically stable graphite form [166, 167].

2.3.8.2.Carbon supports in heterogeneous catalysis

In heterogeneous catalysis carbon based materials are unique supports because of their highly controllable surface properties [4, 146, 160, 168]. The surface properties of carbon can be controlled by functionalizing the carbon atoms in the surface monolayer. The carbon materials are chemically inert and resistant to acidic and basic media. They are also thermally stable at high temperatures and cheaper to produce than most conventional support materials such as silica, titania and alumina. It is easy to tailor the pore size and the structure of a carbon material [160, 168]. They have a high surface area and exhibit high mechanical strength. Furthermore, the active metal phase can easily be recovered from the spent catalyst by burning off the carbon support in air. Properties such as metal dispersion and particle size, activity and selectivity can be readily determined. Therefore, from such properties which are not attainable from other supports it makes the carbon support more unique and very valuable. However, carbon based catalyst cannot be used at temperatures above 430 ^{0}C in the presence of hydrogen or above 230^{0}C in the presence of oxygen due to the production of methane and carbon dioxide, respectively [160, 169]. Oxygen groups can be found on a carbon surface resulting from carboxyl groups which are important in heterogeneous catalysis in that they give the carbon surface an acidic character which is useful as a catalyst anchoring site [170].

2.3.9. Shaped carbon material

At present, carbon materials that have been synthesized include activated carbon (AC), carbon nanotubes (CNTs), carbon nanofibers (CNFs), carbon spheres (CSs), hollow carbon spheres (HCSs), glassy carbon (GCs), and carbon dots (CDs). These material possess different characteristics due to carbon properties being influenced by morphology. Some of the different types of carbon shaped materials that have been used as FT catalyst supports are described below.

2.3.9.1.Activated carbon

Activated carbon (AC) is a processed carbon material that has low-volume pores that increase on the surface area available for adsorption for use in catalytic reactions [171]. Activated carbon has a high surface area due to its microporisty and this property of AC is exploited in many applications. Its main use is usually in water purification, separation of gas mixtures, to treat poisonings and overdoses following ingestion, and natural gas and hydrogen gas storage.

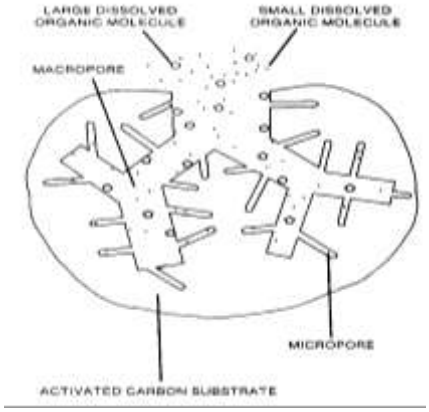


Figure 2. 17: Representation of activated carbon particle [154].

However there are studies of AC in FTS as a catalyst support. Studies worked on cobalt based catalysts supported on activated carbon for FTS have been reported [172-174]. For example, Ma *et al.* studied AC-supported Co catalyst for FTS reaction in a fixed-bed reactor [175]. In their study they found that almond activated carbon may be a suitable support for selective synthesis of C_1-C_{20} hydrocarbons and also that loading the proper amount of Co can increase the yield of the diesel component in FTS product. Xiong *et al.* studied the formation of Co_2C species in AC supported Co-based catalysts and its impact on FT reaction [176]. In the study it was found that the activity of FT reaction over Co-based catalyst decreased due to the formation of Co carbide species.

2.3.9.2.Carbon nanotubes

Carbon nanotubes are carbon allotrophs that have a cylindrical nanostructure. The remarkableble electronic and mechanical properties of CNTs are governed by the nanostructure of CNTs. CNTs are differentiated by their diameter, chiral angles and number of graphene layers. Multi-walled carbon nanotubes (MWCNT) can be determined by the number of graphene stacking layers. Single-walled carbon nanotubes (SWCNs) have a single layer of carbon and a diameter of ~ 2 nm. However, only MWCNT's have been studied in depth as catalyst supports [171].

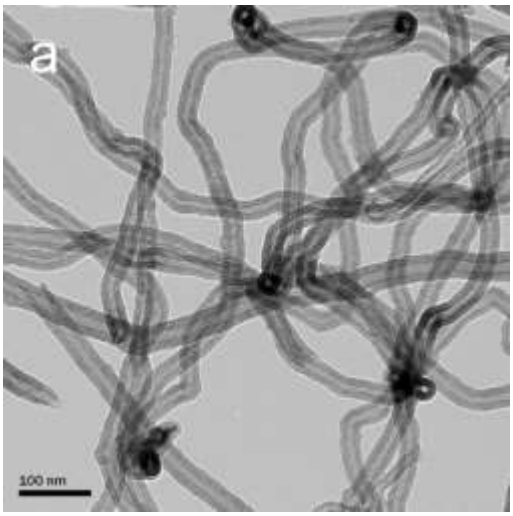


Figure 2. 18: TEM image of CNTS under low magnification [153].

The CNTs can be used as supports in catalysis for example in syngas conversion to hydrocarbons (Fischer-Tropsch process) [173]. For example, Chen *et al.* studied the confinement effect of iron particles inside the nanotube channels for FT reactions [177]. According to their report Fe/CNT supported catalyst gave the yeild of C_{5+} hydrocarbons at higher pressure of 5 MPa. Munga *et al.* studied the effect of catalyst promotion on the FTS actvity, stability, and product selectivity of Fe/CNT catalyst [178]. The Fe supported on CNT's produced a very stable and active catalyst. The addition of potassium (promoter) on the catalyst resulted in increased olefin production, decreased methane production and increased WGS activity.

2.3.9.3.Carbon nanofibers

Carbon nanofibers (CNFs) consist of interwoven fibres of graphene layers arranges as stacked cones, cups or plates. CNFs have a high purity of graphitic carbon with high mechanical strength, and high chemical inertness. The fibres are vapour grown fibres made from techniques such as chemical vapour deposition (CVD). The high temperature used in CVD cause more sp^2 bond formation in that at low temperature processes there is less graphitic carbon, suggesting more sp^3 bonding is present [172].

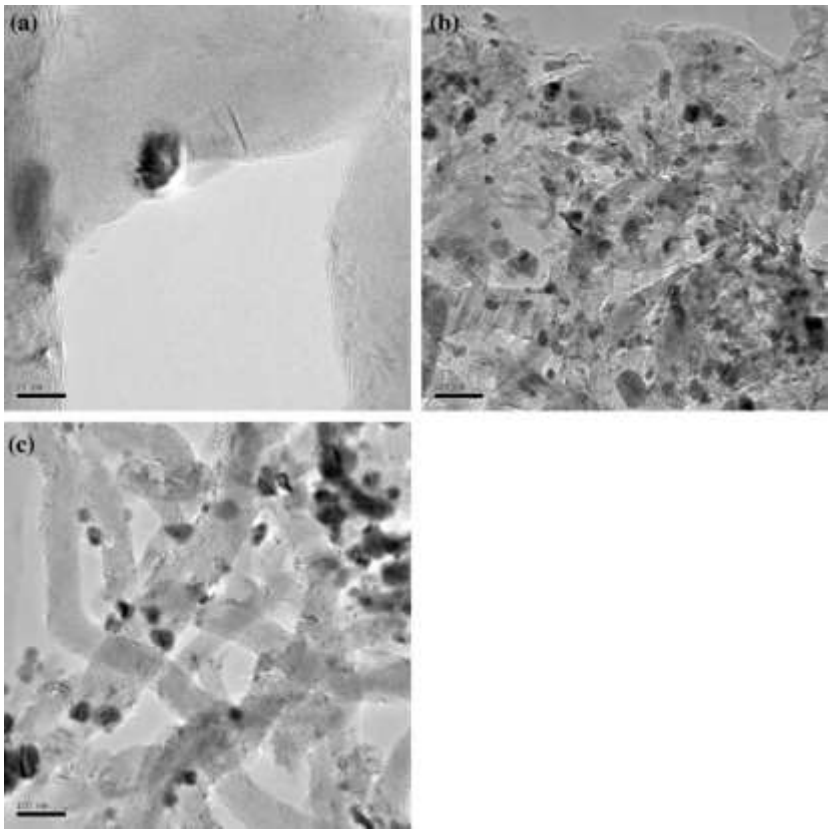


Figure 2. 19: TEM images of (a) a cobalt oxide particle deposited on the edge of a fish bone CNF, (b) Co/Platelet catalyst, (c) Co/CNF [161].

CNFs have been found to be an interesting support for a number of catalytic reactions [179] and both Fe and Co based FT catalysts supported by CNFs have been reported [180, 181]. Benzemer *et al.* showed that CNFs could be a promising support with good activity and selectivity for FTS [182]. Yu *et al.* reported platelet CNF supported cobalt catalyst for FTS with high activity and selectivity (Fig 2.5) [183]. The Co/CNF catalyst showed high selectivity to C_{5+} hydrocarbons with activity as high as γ-Al_2O_3 supported Co catalyst [183].

2.3.9.4.Carbon sphere

Carbon spheres (CSs) have distinctive properties such as excellent structural stability, high purity, high surface-to-volume ratio, low electrical sesistance, along with the possibilty to modify their surfaces and interiors by coating and dopig. CSs have been used as additives in making materials such as tyres. Their structure is spherical in nanoscale (Figure 6).

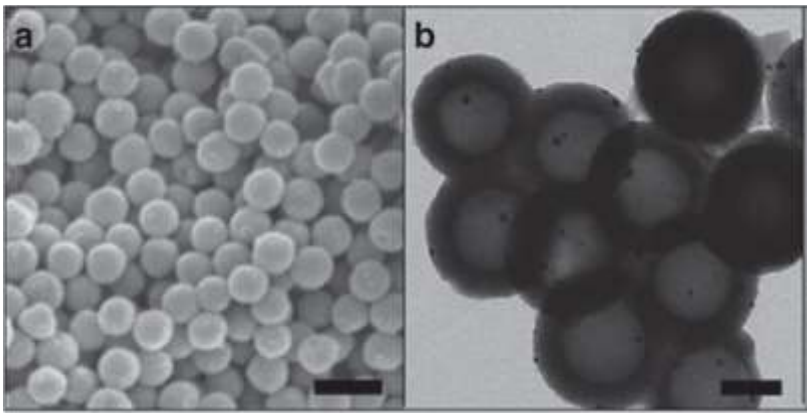


Figure 2. 20: Carbon nanospheres SEM image (a), Carbon nanospheres agglomerated TEM image (b) [184].

CSs are synthesised by two methods: In the first method, CVD process is applied usually in the absence of a catalyst [185, 186]. The second method is the hydrothermal synthesis (HTS) which consists of using heating organic carbon complexes such as glucose or sucrose in an autoclave [187, 188].

CSs are used in FTS as catalyst support. The use of CS as a FT catalyst support was due to its advantages of minimal surface energies, controllable sizes, high mechanical stability and tunable properties. Xiong *et al.* reported that CVD-synthesized CSs are better support for Co FT catalyst than CNT's due to their easier preparation and them having no metal impurities [189]. Studies by Moyo *et al.* showed that Fe FT catalyst supported by CSs had more functional groups on the carbon surface due to $KMnO_4$ treatment resulted in higher selectivies towards heavy hydrocarbons during FT synthesis [190]. Dlamini *et al.* reported a yolk-shell structure of ruthenium nanoparticles partially embedd in the carbon support (Ru@C) has been reported to demonstrate high catalytic activity in FT synthesis [191]. The high catalytic activity was due to minimized sintering of the ruthenium nanoparticles during the reaction [191].

2.3.9.5.Hollow carbon spheres

Hollow carbon spheres (HCS) have a high surface area, excellent electronic conductivity, low weight, and they have chemical inert properties. Their spherical structure enables them to be used as nanoreactors by encapsulating the active metal phase to form a heterogeneous catalyst. Due to HCSs high surface area and stability they have been used to support Pd or Pt in electro-catalysis [65]. The porosity of HCSs can be varied. Mesoporous hollow carbon spheres (MHCSs) have nano-channels where the metal catalyst can be deposited in the pores or channels and at the same time the reactants can be transported through the pores and thus increase interfacial reactions.

An advantage of using HCSs in heterogeneous catalysis such as FTS is that metal nanoparticles can be encapsulated inside HCSs thus reducing metal sintering under reaction conditions. In *section 2.1.3.4* Ru nanoparticles encapsulated inside HCS was studied as a FTS catalyst [72].

2.3.10. Conclusions and outlook

In this review, the hollow carbon spheres synthesis and applications were discussed. A brief description of the different types of templates and methods for the synthesis of HCS and its applications was given. The osmium metal chemical and physical properties and applications in various fields were discussed. A comprehensive review on the Fischer-Tropsch synthesis history, mechanisms, metals and supports was reported. Overall, many reports exist in literature on the application of Fe, Co and Ru supported with various shaped carbon materials in FTS. These reports have been useful in understanding how changing the properties of the nanostructure catalyst could influence the catalytic performance. However, less literature has been dedicated on the study of Os metal and nanoparticles application in the FTS. In this study, we encapsulate Os nanoparticles inside HCS and investigate its catalytic performance in FTS.

2.4. Reference

1. Kang, Z. and Z. Wang, *Pairing of pentagonal carbon rings in the growth of nanosized carbon spheres synthesized by a mixed-valent oxide-catalytic carbonization process.* J Phys Chem, 1996. **100**: p. 17725-31.
2. Xia, Y., et al., *Monodispersed colloidal spheres: old materials with new applications.* Advanced Materials, 2000. **12**(10): p. 693-713.
3. Flandrois, S. and B. Simon, *Carbon materials for lithium-ion rechargeable batteries.* Carbon, 1999. **37**(2): p. 165-180.
4. Liu, R., et al., *Au@ carbon yolk–shell nanostructures via one-step core–shell–shell template.* Chemical Communications, 2014. **50**(4): p. 478-480.
5. Joo, S.H., et al., *Thermally stable Pt/mesoporous silica core–shell nanocatalysts for high-temperature reactions.* Nature materials, 2009. **8**(2): p. 126-131.
6. Kim, J., et al., *Magnetic fluorescent delivery vehicle using uniform mesoporous silica spheres embedded with monodisperse magnetic and semiconductor nanocrystals.* Journal of the American Chemical Society, 2006. **128**(3): p. 688-689.
7. Ge, J., et al., *Core–satellite nanocomposite catalysts protected by a porous silica shell: controllable reactivity, high stability, and magnetic recyclability.* Angewandte Chemie, 2008. **120**(46): p. 9056-9060.
8. Yue, Q., et al., *An interface coassembly in biliquid phase: Toward core–shell magnetic mesoporous silica microspheres with tunable pore size.* J. Am. Chem. Soc, 2015. **137**(41): p. 13282-13289.
9. Ikeda, S., et al., *Ligand-Free Platinum Nanoparticles Encapsulated in a Hollow Porous Carbon Shell as a Highly Active Heterogeneous Hydrogenation Catalyst.* Angewandte Chemie, 2006. **118**(42): p. 7221-7224.
10. Harada, T., et al., *Rhodium nanoparticle encapsulated in a porous carbon shell as an active heterogeneous catalyst for aromatic hydrogenation.* Advanced Functional Materials, 2008. **18**(15): p. 2190-2196.
11. Liang, C., Z. Li, and S. Dai, *Mesoporous carbon materials: synthesis and modification.* Angewandte Chemie International Edition, 2008. **47**(20): p. 3696-3717.
12. Gao, C., et al., *Templated synthesis of metal nanorods in silica nanotubes.* Journal of the American Chemical Society, 2011. **133**(49): p. 19706-19709.

13. Sun, Y., B. Mayers, and Y. Xia, *Metal nanostructures with hollow interiors.* Advanced Materials, 2003. **15**(7-8): p. 641-646.
14. Piñeiro-Redondo, Y., et al., *The influence of colloidal parameters on the specific power absorption of PAA-coated magnetite nanoparticles.* Nanoscale research letters, 2011. **6**(1): p. 383.
15. Xia, Y. and R. Mokaya, *Synthesis of ordered mesoporous carbon and nitrogen-doped carbon materials with graphitic pore walls via a simple chemical vapor deposition method.* Advanced materials, 2004. **16**(17): p. 1553-1558.
16. White, R.J., et al., *Functional hollow carbon nanospheres by latex templating.* Journal of the American Chemical Society, 2010. **132**(49): p. 17360-17363.
17. Yang, Z.-C., et al., *Hollow carbon nanoparticles of tunable size and wall thickness by hydrothermal treatment of α-cyclodextrin templated by F127 block copolymers.* Chemistry of Materials, 2013. **25**(5): p. 704-710.
18. Liu, J., et al., *Molecular-based design and emerging applications of nanoporous carbon spheres.* Nature materials, 2015. **14**(8): p. 763-774.
19. Liu, Y., J. Goebl, and Y. Yin, *Templated synthesis of nanostructured materials.* Chemical Society Reviews, 2013. **42**(7): p. 2610-2653.
20. Lai, L., et al., *Solvothermal syntheses of hollow carbon microspheres modified with–NH 2 and–OH groups in one-step process.* Carbon, 2010. **48**(11): p. 3145-3156.
21. Wan, Y. and D. Zhao, *On the controllable soft-templating approach to mesoporous silicates.* Chemical reviews, 2007. **107**(7): p. 2821-2860.
22. Liang, Y., R. Fu, and D. Wu, *Reactive template-induced self-assembly to ordered mesoporous polymeric and carbonaceous materials.* ACS nano, 2013. **7**(2): p. 1748-1754.
23. Sun, G., et al., *A novel approach for fabrication of hollow carbon spheres with large size and high specific surface area.* Microporous and Mesoporous Materials, 2011. **139**(1): p. 207-210.
24. Qiao, Z.-A., et al., *Controlled synthesis of mesoporous carbon nanostructures via a "silica-assisted" strategy.* Nano letters, 2012. **13**(1): p. 207-212.
25. Li, Y. and J. Shi, *Hollow-Structured Mesoporous Materials: Chemical Synthesis, Functionalization and Applications.* Advanced Materials, 2014. **26**(20): p. 3176-3205.
26. Stöber, W., A. Fink, and E. Bohn, *Controlled growth of monodisperse silica spheres in the micron size range.* Journal of colloid and interface science, 1968. **26**(1): p. 62-69.

27. Tun, N., et al., *Preparation and characterization of hollow carbon nanospheres.* Inorganic Materials, 2015. **51**(5).
28. Brinker, C.J. and G.W. Scherer, *Sol-gel science: the physics and chemistry of sol-gel processing*. 2013: Academic press.
29. Malay, O., I. Yilgor, and Y.Z. Menceloglu, *Effects of solvent on TEOS hydrolysis kinetics and silica particle size under basic conditions.* Journal of sol-gel science and technology, 2013. **67**(2): p. 351-361.
30. Tang, J., et al., *Nitrogen-doped hollow carbon spheres with large mesoporous shells engineered from diblock copolymer micelles.* Chemical Communications, 2016. **52**(3): p. 505-508.
31. Chen, X., et al., *Synthesis, growth mechanism, and electrochemical properties of hollow mesoporous carbon spheres with controlled diameter.* The Journal of Physical Chemistry C, 2011. **115**(36): p. 17717-17724.
32. Yu, Y., et al., *Au nanoparticles embedded into the inner wall of TiO 2 hollow spheres as a nanoreactor with superb thermal stability.* Chemical Communications, 2013. **49**(30): p. 3116-3118.
33. Chen, C., et al., *A Multi-Yolk–Shell Structured Nanocatalyst Containing Sub-10 nm Pd Nanoparticles in Porous CeO2.* ChemCatChem, 2012. **4**(10): p. 1578-1586.
34. Yan, N., et al., *High catalytic activity for CO oxidation of Co 3 O 4 nanoparticles in SiO 2 nanocapsules.* Journal of Materials Chemistry A, 2013. **1**(3): p. 637-643.
35. Huang, X., et al., *An assembly route to inorganic catalytic nanoreactors containing sub-10-nm gold nanoparticles with anti-aggregation properties.* Small, 2009. **5**(3): p. 361-365.
36. Harada, T., et al., *Catalytic activity and regeneration property of a Pd nanoparticle encapsulated in a hollow porous carbon sphere for aerobic alcohol oxidation.* Langmuir, 2010. **26**(22): p. 17720-17725.
37. Bian, S.-W., et al., *Pd nanoparticles partially embedded in the inner wall of nitrogen-doped carbon hollow spheres as nanoreactors for catalytic reduction of 4-nitrophenol.* RSC Advances, 2015. **5**(16): p. 11913-11916.
38. Bian, S.-W., et al., *Silica nanotubes with mesoporous walls and various internal morphologies using hard/soft dual templates.* Chemical Communications, 2009(10): p. 1261-1263.

39. Jiang, H., et al., *Functional mesoporous carbon nanotubes and their integration in situ with metal nanocrystals for enhanced electrochemical performances.* Chemical Communications, 2011. **47**(30): p. 8590-8592.
40. Li, Z., et al., *One-pot synthesis of Pd nanoparticle catalysts supported on N-doped carbon and application in the domino carbonylation.* ACS Catalysis, 2013. **3**(5): p. 839-845.
41. Li, S., et al., *Size-selective hydrogenation at the subnanometer scale over platinum nanoparticles encapsulated in silicalite-1 single crystal hollow shells.* Chemical Communications, 2014. **50**(15): p. 1824-1826.
42. Park, J.C., et al., *Catalytic hydrogen transfer of ketones over Ni@ SiO2 yolk− shell nanocatalysts with tiny metal cores.* The Journal of Physical Chemistry C, 2010. **114**(14): p. 6381-6388.
43. Phago, E.R., *Synthesis of catalyst nanoparticles encapsulated in mesoporous carbon spheres and their subsequent use as catalysts for the oxygen reduction reaction*. 2016.
44. Phaahlamohlaka, T.N., et al., *Ruthenium nanoparticles encapsulated inside porous hollow carbon spheres: A novel catalyst for Fischer–Tropsch synthesis.* Catalysis Today, 2016. **275**: p. 76-83.
45. Su, F., et al., *Hollow carbon spheres with a controllable shell structure.* Journal of materials chemistry, 2006. **16**(45): p. 4413-4419.
46. Haynes, W.M., *CRC handbook of chemistry and physics*. 2014: CRC press.
47. Cynn, H., et al., *Osmium has the lowest experimentally determined compressibility*. Physical review letters, 2002. **88**(13): p. 135701.
48. Sahu, B. and L. Kleinman, *Osmium is not harder than diamond.* Physical Review B, 2005. **72**(11): p. 113106.
49. Wedepohl, K.H., *The composition of the continental crust*. Geochimica et cosmochimica Acta, 1995. **59**(7): p. 1217-1232.
50. Barnes, C.E., *Inorganic Chemistry (Catherine E. Housecroft and Alan G. Sharpe).* Journal of Chemical Education, 2003. **80**: p. 747.
51. Griffith, W.P., *The chemistry of the rarer platinum metals (Os, Ru, Ir, and Rh)*. Vol. 3. 1967: Interscience publishers.
52. Ede, S.R., U. Nithiyanantham, and S. Kundu, *Enhanced catalytic and SERS activities of CTAB stabilized interconnected osmium nanoclusters.* Physical Chemistry Chemical Physics, 2014. **16**(41): p. 22723-22734.

53. Nithiyanantham, U., S.R. Ede, and S. Kundu, *Self-assembled wire-like and honeycomb-like osmium nanoclusters (NCs) in DNA with pronounced catalytic and SERS activities.* Journal of Materials Chemistry C, 2014. **2**(19): p. 3782-3794.
54. Anantharaj, S., et al., *Osmium organosol on DNA: application in catalytic hydrogenation reaction and in SERS studies.* Industrial & Engineering Chemistry Research, 2014. **53**(49): p. 19228-19238.
55. Boyd, E.P., et al., *Chemical vapor deposition of metallic thin films using homonuclear and heteronuclear metal carbonyls.* Chemistry of materials, 1997. **9**(5): p. 1154-1158.
56. Forleo, A., et al., *Role of osmium in the electrical transport mechanism of polycrystalline tin oxide thin films.* Applied physics letters, 2004. **84**(5): p. 744-746.
57. Yung, K.-F. and W.-T. Wong, *Synthesis and Catalytic Studies of Uniform Os & Os–Pd Nanoparticles Supported on MWNTs.* Journal of Cluster Science, 2007. **18**(1): p. 51-65.
58. Jones, T., *Electrodeposition of osmium.* Metal finishing, 2002. **100**(6): p. 8486-90.
59. Lam, V.W. and E.L. Gyenge, *High-performance osmium nanoparticle electrocatalyst for direct borohydride PEM fuel cell anodes.* Journal of The Electrochemical Society, 2008. **155**(11): p. B1155-B1160.
60. Lee, C.H., et al., *Highly efficient MCM-48-based template synthesis of osmium and platinum 3-D nanonetworks.* BULLETIN-KOREAN CHEMICAL SOCIETY, 2006. **27**(1): p. 130.
61. Krämer, J., et al., *Use of ionic liquids for the synthesis of iron, ruthenium, and osmium nanoparticles from their metal carbonyl precursors.* Organometallics, 2008. **27**(9): p. 1976-1978.
62. Hämäläinen, J., et al., *Atomic Layer Deposition of Osmium.* Chemistry of Materials, 2011. **24**(1): p. 55-60.
63. Yu, H.L., et al., *New CVD source reagents for osmium thin film deposition.* Chemical Vapor Deposition, 2001. **7**(6): p. 245-248.
64. Yu, M., et al., *Sol–gel synthesis and photoluminescence properties of spherical SiO2@ LaPO4: Ce3+/Tb3+ particles with a core–shell structure.* Nanotechnology, 2006. **17**(13): p. 3245.
65. Josell, D., C. Witt, and T. Moffat, *Osmium barriers for direct copper electrodeposition in damascene processing.* Electrochemical and Solid-State Letters, 2006. **9**(2): p. C41-C43.

66. Low, J.E., et al., *Narrowly dispersed silica supported osmium nanoparticles prepared by an organometallic approach: H 2 and CO adsorption stoichiometry and hydrogenolysis catalytic activity.* Dalton Transactions, 2013. **42**(35): p. 12620-12625.
67. Kundu, S., et al., *Polyelectrolyte mediated scalable synthesis of highly stable silver nanocubes in less than a minute using microwave irradiation.* Nanotechnology, 2008. **19**(6): p. 065604.
68. Lohray, B.B., *Recent advances in the asymmetric dihydroxylation of alkenes.* Tetrahedron: Asymmetry, 1992. **3**(11): p. 1317-1349.
69. Seligman, A.M., H.L. Wasserkrug, and J.S. Hanker, *A new staining method (OTO) for enhancing contrast of lipid-containing membranes and droplets in osmium tetroxide-fixed tissue with osmiophilic thiocarbohydrazide (TCH).* The Journal of cell biology, 1966. **30**(2): p. 424.
70. Hanker, J.S., et al., *Staining tissue for light and electron microscopy by bridging metals with multidentate ligands.* Science, 1966. **152**(3729): p. 1631-1634.
71. Kundu, S., K. Wang, and H. Liang, *Size-selective synthesis and catalytic application of polyelectrolyte encapsulated gold nanoparticles using microwave irradiation.* The Journal of Physical Chemistry C, 2009. **113**(13): p. 5157-5163.
72. Kundu, S., *Formation of self-assembled Ag nanoparticles on DNA chains with enhanced catalytic activity.* Physical Chemistry Chemical Physics, 2013. **15**(33): p. 14107-14119.
73. Saha, A. and B. Ranu, *Highly chemoselective reduction of aromatic nitro compounds by copper nanoparticles/ammonium formate.* The Journal of organic chemistry, 2008. **73**(17): p. 6867-6870.
74. Anantharaj, S., et al., *π-stacking intercalation and reductant assisted stabilization of osmium organosol for catalysis and SERS applications.* RSC Advances, 2015. **5**(16): p. 11850-11860.
75. Smith, A., et al., *Surface supported metal cluster carbonyls. the surface organometallic chemistry of polymetallic and monometallic osmium carbonyl species formed by depositing various osmium clusters on silica and alumina.* Journal of Organometallic Chemistry, 1980. **192**(2): p. C31-C34.
76. Psaro, R., et al., *Surface-supported metal cluster carbonyls. Chemisorption, decomposition and reactivity of Os3 (CO) 12, H2Os3 (CO) 10 and Os6 (CO) 18 supported on silica and alumina and the investigation of the fischer-tropsch catalysis with these systems.* Journal of Organometallic Chemistry, 1981. **213**(1): p. 215-247.

77. Deeba, M. and B. Gates, *Mononuclear and trinuclear osmium carbonyl catalysts supported on SiO2, Al2O3, TiO2, and ZnO.* Journal of Catalysis, 1981. **67**(2): p. 303-307.

78. Knözinger, H. and Y. Zhao, *Infrared characterization of mononuclear osmium carbonyl species on alumina.* Journal of Catalysis, 1981. **71**(2): p. 337-347.

79. Jackson, S.D. and P.B. Wells, *Metal clusters as catalyst sites: site-support and site-carbon interactions.* Applied Catalysis, 1986. **25**(1-2): p. 157-163.

80. Jackson, S.D., et al., *Chemisorption and catalysis by metal clusters: III. Hydrogenation of ethene, carbon monoxide, and carbon dioxide, and hydrogenolysis of ethane catalyzed by supported osmium clusters derived from Os3 (CO) 12 and from Os6 (CO) 18.* Journal of Catalysis, 1984. **86**(2): p. 342-358.

81. Knözinger, H., et al., *Alumina-supported CO hydrogenation catalysts prepared from molecular osmium and ruthenium clusters.* Faraday Discussions of the Chemical Society, 1981. **72**: p. 53-71.

82. Hunt, D.J., et al., *Chemisorption and catalysis by metal clusters: characterisation and chemisorption. Properties of Ru 3 (CO) 12 and H 4 Ru 4 (CO) 12 supported on alumina, silica and titania.* Journal of the Chemical Society, Faraday Transactions 1: Physical Chemistry in Condensed Phases, 1986. **82**(1): p. 189-204.

83. Jackson, S.D. and P.B. Wells, *Catalysis by Osmium Metal Clusters.* Platinum Metals Review, 1986. **30**(1): p. 14-20.

84. Schrock, R.R. and J. Lewis, *Preparation of ruthenium (0) and osmium (0) cyclooctatetraene complexes.* Journal of the American Chemical Society, 1973. **95**(12): p. 4102-4103.

85. Sarma, D. and C. Rao, *XPES studies of oxides of second-and third-row transition metals including rare earths.* Journal of Electron Spectroscopy and Related Phenomena, 1980. **20**(1): p. 25-45.

86. Hayakawa, Y., et al., *X-ray photoelectron spectroscopy of highly conducting and amorphous osmium dioxide thin films.* Thin Solid Films, 1999. **347**(1): p. 56-59.

87. Rodriguez, E., M. Leconte, and J.-M. Basset, *Homologation and hydrogenolysis of linear and branched butenes and butanes on Ru/SiO 2 catalysts.* Journal of Catalysis, 1991. **131**(2): p. 457-481.

88. eoh. *Johann Dobereiner*. 2015, August 29; Available from: http://www.eoht.info/page/Johann+Dobereiner.

89. Schulz, H., *Short history and present trends of Fischer–Tropsch synthesis.* Applied Catalysis A: General, 1999. **186**(1): p. 3-12.
90. Sehested, J., et al., *Methanation of CO over nickel: mechanism and kinetics at high H2/CO ratios.* The Journal of Physical Chemistry B, 2005. **109**(6): p. 2432-2438.
91. Fischer, F. and H. Tropsch, *The preparation of synthetic oil mixtures (synthol) from carbon monoxide and hydrogen.* Brennstoff-Chem, 1923. **4**: p. 276-285.
92. Bartholomew, C.H., *Recent technological developments in Fischer-Tropsch catalysis.* Catalysis Letters, 1990. **7**(1-4): p. 303-315.
93. King, D.L. and A. de Klerk, *Overview of feed-to-liquid (XTL) conversion*, in *Synthetic Liquids Production and Refining*. 2011, ACS Publications. p. 1-24.
94. Anderson, R.B., H. Kölbel, and M. Rálek, *The Fischer-Tropsch Synthesis*. 1984: Academic Pr.
95. Frohning, C., et al., *Chemierohstoffe aus kohle*. 1977, Thieme, Stuttgart.
96. Abel, F.A., *NAMED THINGS IN CHEMICAL INDUSTRY.* 2000.
97. Stranges, A.N., *A history of the fischer-tropsch synthesis in Germany 1926-45.* Studies in surface science and catalysis, 2007: p. 1-27.
98. Dry, M.E., *The fischer–tropsch process: 1950–2000.* Catalysis today, 2002. **71**(3): p. 227-241.
99. GoDaddy. *Historical Development of Cobalt-slurry Fischer-Tropsch Reactor Systems* 1999; Available from: http://www.fischertropsch.org/primary_documents/presentations/Co_Slurry_FT_Dev/Co_Slurry_FT_Dev_ref.htm.
100. Das, T.K., et al., *Fischer− Tropsch synthesis: Kinetics and effect of water for a Co/SiO2 catalyst*. Energy & fuels, 2005. **19**(4): p. 1430-1439.
101. Mabaso, E.I., *Nanosized iron crystallites for Fischer-Tropsch synthesis*. 2005, University of Cape Town.
102. Fahim, M.A., T.A. Al-Sahhaf, and A. Elkilani, *Fundamentals of petroleum refining*. 2009: Elsevier.
103. Stenger Jr, H.G. and C.F. Askonas, *Thermodynamic product distributions for the Fischer-Tropsch synthesis.* Industrial & engineering chemistry fundamentals, 1986. **25**(3): p. 410-413.
104. Bartholomew, C.H. and L. Guczi, *New trends in CO activation.* Stud. Surf. Sci. Catal, 1991. **64**: p. 158.

105. Nowicki, L., S. Ledakowicz, and D.B. Bukur, *Hydrocarbon selectivity model for the slurry phase Fischer–Tropsch synthesis on precipitated iron catalysts.* Chemical engineering science, 2001. **56**(3): p. 1175-1180.

106. Davis, B.H., *Fischer–Tropsch synthesis: current mechanism and futuristic needs.* Fuel Processing Technology, 2001. **71**(1): p. 157-166.

107. Khodakov, A.Y., W. Chu, and P. Fongarland, *Advances in the development of novel cobalt Fischer− Tropsch catalysts for synthesis of long-chain hydrocarbons and clean fuels.* Chemical reviews, 2007. **107**(5): p. 1692-1744.

108. van Steen, E. and M. Claeys, *Fischer-Tropsch Catalysts for the Biomass-to-Liquid (BTL)-Process.* Chemical engineering & technology, 2008. **31**(5): p. 655-666.

109. Maitlis, P.M., et al., *Heterogeneous catalysis of C–C bond formation: black art or organometallic science?* Chemical Communications, 1996(1): p. 1-8.

110. Pichler, H., H. Schulz, and M. Elstner, *Gesetzmassigkeiten bei der synthese von kohlenwasserstoffen aus kohlenoxid und wasserstoff.* BRENNSTOFF-CHEMIE, 1967. **48**(3): p. 78-&.

111. Madon, R. and W. Taylor, *Fischer-Tropsch synthesis on a precipitated iron catalyst.* Journal of Catalysis, 1981. **69**(1): p. 32-43.

112. Huff, G.A. and C.N. Satterfield, *Evidence for two chain growth probabilities on iron catalysts in the Fischer-Tropsch synthesis.* Journal of Catalysis, 1984. **85**(2): p. 370-379.

113. König, L. and J. Gaube, *Fischer-Tropsch-Synthese. Neuere Untersuchungen und Entwicklungen.* Chemie Ingenieur Technik, 1983. **55**(1): p. 14-22.

114. Iglesia, E., S.C. Reyes, and R.J. Madon, *Transport-enhanced α-olefin readsorption pathways in Ru-catalyzed hydrocarbon synthesis.* Journal of Catalysis, 1991. **129**(1): p. 238-256.

115. Masuku, C.M., D. Hildebrandt, and D. Glasser, *The role of vapour–liquid equilibrium in Fischer–Tropsch product distribution.* Chemical engineering science, 2011. **66**(23): p. 6254-6263.

116. Fischer, F. and H. Pichler, *Synthesis of paraffin from carbon monoxide and hydrogen.[Using CoThO/sub 2/--kieselguhr as catalyst].* Ber, 1939. **72**.

117. Traa, Y., *Is a renaissance of coal imminent?—challenges for catalysis.* Chemical Communications, 2010. **46**(13): p. 2175-2187.

118. Jager, B., *Developments in Fischer-Tropsch technology.* Studies in Surface Science and Catalysis, 1997. **107**: p. 219-224.

119. Madon, R.J., S.C. Reyes, and E. Iglesia, *Primary and secondary reaction pathways in ruthenium-catalyzed hydrocarbon synthesis.* The Journal of Physical Chemistry, 1991. **95**(20): p. 7795-7804.

120. Linganiso, L.Z., *Microwave induced solid-state interactions for the synthesis of Fischer-Tropsch catalysts*. 2010.

121. Vannice, M., *The catalytic synthesis of hydrocarbons from H2CO mixtures over the group VIII metals: III. Metal-support effects with Pt and Pd catalysts.* Journal of Catalysis, 1975. **40**(1): p. 129-134.

122. Brady III, R.C. and R. Pettit, *Reactions of diazomethane on transition-metal surfaces and their relationship to the mechanism of the Fischer-Tropsch reaction.* Journal of the American Chemical Society, 1980. **102**(19): p. 6181-6182.

123. Davis, B.H., *Fischer-Tropsch synthesis: relationship between iron catalyst composition and process variables.* Catalysis Today, 2003. **84**(1): p. 83-98.

124. Dry, M.E., *Practical and theoretical aspects of the catalytic Fischer-Tropsch process.* Applied Catalysis A: General, 1996. **138**(2): p. 319-344.

125. Choi, G.N., et al. *Design/economics of a natural gas based Fischer-Tropsch plant*. in *Spring National Meeting*. 1996. American Institute of Chemical Engineers Houston.

126. Schulz, H., R. Ramananda, and M. Elstner, *Carbon-14 studies for the evaluation of the reaction mechanism of the Fischer--Tropsch synthesis.* Erdoel Kohle, Erdgas, Petrochem. Brennst.-Chem., 1970. **23**(10).

127. Puskas, I. and R. Hurlbut, *Comments about the causes of deviations from the Anderson–Schulz–Flory distribution of the Fischer–Tropsch reaction products.* Catalysis Today, 2003. **84**(1): p. 99-109.

128. Schulz, H., et al., *Regularities of selectivity as a key for discriminating FT-surface reactions and formation of the dynamic system*. Catalysis Letters, 1990. **7**(1-4): p. 157-167.

129. Long, H.C., et al., *Vinylic Initiation of the Fischer–Tropsch Reaction over Ruthenium on Silica Catalysts.* Journal of Catalysis, 1997. **167**(1): p. 172-179.

130. Bahome, M.C., *Synthesis and use of carbon nanotubes as a support for the Fischer-Tropsch Synthesis.* 2008.

131. Pichler, H. and H. Schulz, *Recent results in synthesis of hydrocarbons from CO and H2*. Chemie Ingenieur Technik, 1970. **42**(18): p. 1162-&.

132. Hindermann, J., G. Hutchings, and A. Kiennemann, *Mechanistic aspects of the formation of hydrocarbons and alcohols from CO hydrogenation.* Catalysis Reviews—Science and Engineering, 1993. **35**(1): p. 1-127.
133. De Beer, M., et al., *Technical and economic aspects of promotion of cobalt-based Fischer-Tropsch catalysts by noble metals-a review*. Journal of the Southern African Institute of Mining and Metallurgy, 2014. **114**(2): p. 157-165.
134. Vannice, M., *The catalytic synthesis of hydrocarbons from H2CO mixtures over the Group VIII metals: V. The catalytic behavior of silica-supported metals.* Journal of Catalysis, 1977. **50**(2): p. 228-236.
135. Mokoena, E.M., *Synthesis and use of silica materials as supports for the Fischer-Tropsch reaction*. 2006.
136. Basset, J., et al., *Supported cluster and Mechanism of CO Reduction.* Fundam. Res. Homogeneous Catal, 1984: p. 19-53.
137. Espinoza, R., et al., *Low temperature Fischer–Tropsch synthesis from a Sasol perspective*. Applied Catalysis A: General, 1999. **186**(1): p. 13-26.
138. Bessell, S., *Support effects in cobalt-based fischer-tropsch catalysis.* Applied Catalysis A: General, 1993. **96**(2): p. 253-268.
139. Reuel, R.C. and C.H. Bartholomew, *Effects of support and dispersion on the CO hydrogenation activity/selectivity properties of cobalt*. Journal of Catalysis, 1984. **85**(1): p. 78-88.
140. Storch, H.H., R.A. Anderson, and N. Golumbic, *The Fischer-Tropsch and related syntheses*. Vol. 6. 1951: Wiley New York.
141. Carberry, J.J., *Mass Transfer in Heterogeneous Catalysis: MIT Press, Cambridge, Massachusetts and London, England*. 1971, Pergamon.
142. Rodríguez-Reinoso, F., *The role of carbon materials in heterogeneous catalysis.* Carbon, 1998. **36**(3): p. 159-175.
143. Martínez, A.n., et al., *Fischer–Tropsch synthesis of hydrocarbons over mesoporous Co/SBA-15 catalysts: the influence of metal loading, cobalt precursor, and promoters.* Journal of Catalysis, 2003. **220**(2): p. 486-499.
144. Moyo, M., *Cobalt and iron supported on carbon spheres catalysts for Fischer Tropsch synthesis*. 2012.
145. Radovic, L.R. and F. Rodriguez-Reinoso, *Carbon materials in catalysis.* Chemistry and physics of carbon, 1997. **25**: p. 243.

146. Moreno-Castilla, C., et al., *Carbon as a support for catalysts—III glassy carbon as a support for iron.* Carbon, 1980. **18**(4): p. 271-276.
147. Goncharov, A., *Stability of diamond at high pressures.* Physics-Uspekhi, 1987. **30**(6): p. 525-534.
148. Ebbesen, T.W., *Carbon nanotubes: preparation and properties*. 1996: CRC press.
149. Saito, R., G. Dresselhaus, and M.S. Dresselhaus, *Physical properties of carbon nanotubes*. 1998: World Scientific.
150. Zhao, Y.-L., et al., *A tunable photosensor.* Journal of the American Chemical Society, 2008. **130**(50): p. 16996-17003.
151. Anderson, R. and R.A.P. Emmett, *Catalysis, Vol. IV, Reinhold, New York (1956).* Catalysis, 1946. **4**: p. 208.
152. Stiles, A.B., *Catalyst supports and supported catalysts.* 1987.
153. Wikimedia. *Carbon black*. 2017.
154. Xiong, H., L.L. Jewell, and N.J. Coville, *Shaped Carbons As Supports for the Catalytic Conversion of Syngas to Clean Fuels.* ACS Catalysis, 2015. **5**(4): p. 2640-2658.
155. De Jong, K.P. and J.W. Geus, *Carbon nanofibers: catalytic synthesis and applications.* Catalysis Reviews, 2000. **42**(4): p. 481-510.
156. Serp, P., M. Corrias, and P. Kalck, *Carbon nanotubes and nanofibers in catalysis.* Applied Catalysis A: General, 2003. **253**(2): p. 337-358.
157. Ma, W.-P., Y.-J. Ding, and L.-W. Lin, *Fischer− Tropsch Synthesis over Activated-Carbon-Supported Cobalt Catalysts: Effect of Co Loading and Promoters on Catalyst Performance.* Industrial & engineering chemistry research, 2004. **43**(10): p. 2391-2398.
158. Xiong, J., et al., *The formation of Co 2 C species in activated carbon supported cobalt-based catalysts and its impact on Fischer–Tropsch reaction.* Catalysis Letters, 2005. **102**(3): p. 265-269.
159. van Steen, E. and F.F. Prinsloo, *Comparison of preparation methods for carbon nanotubes supported iron Fischer–Tropsch catalysts.* Catalysis Today, 2002. **71**(3): p. 327-334.
160. Bahome, M.C., et al., *Fischer–Tropsch synthesis over iron catalysts supported on carbon nanotubes.* Applied Catalysis A: General, 2005. **287**(1): p. 60-67.
161. Yu, Z., et al., *Carbon nanofiber supported cobalt catalysts for Fischer–Tropsch synthesis with high activity and selectivity.* Catalysis Letters, 2006. **109**(1-2): p. 43-47.
162. Iijima, S., *Helical microtubules of graphitic carbon.* nature, 1991. **354**(6348): p. 56.

163. Iijima, S. and T. Ichihashi, *Single-shell carbon nanotubes of 1-nm diameter.* nature, 1993. **363**(6430): p. 603.
164. Bethune, D., et al., *Cobalt-catalysed growth of carbon nanotubes with single-atomic-layer walls.* Nature, 1993. **363**(6430): p. 605.
165. Bezemer, G.L., et al., *Cobalt particle size effects in the Fischer− Tropsch reaction studied with carbon nanofiber supported catalysts.* Journal of the American Chemical Society, 2006. **128**(12): p. 3956-3964.
166. Jin, Y.Z., et al., *Large-scale synthesis and characterization of carbon spheres prepared by direct pyrolysis of hydrocarbons.* Carbon, 2005. **43**(9): p. 1944-1953.
167. Serp, P., et al., *A chemical vapour deposition process for the production of carbon nanospheres.* Carbon, 2001. **39**(4): p. 621-626.
168. Miao, J.-Y., et al., *Synthesis and properties of carbon nanospheres grown by CVD using Kaolin supported transition metal catalysts.* Carbon, 2004. **42**(4): p. 813-822.
169. Titirici, M.-M., M. Antonietti, and N. Baccile, *Hydrothermal carbon from biomass: a comparison of the local structure from poly-to monosaccharides and pentoses/hexoses.* Green Chemistry, 2008. **10**(11): p. 1204-1212.
170. Yu, L., et al., *Carbohydrate-derived hydrothermal carbons: a thorough characterization study.* Langmuir, 2012. **28**(33): p. 12373-12383.
171. Xiong, H., et al., *Correlating the preparation and performance of cobalt catalysts supported on carbon nanotubes and carbon spheres in the Fischer–Tropsch synthesis.* Journal of catalysis, 2011. **278**(1): p. 26-40.
172. Moyo, M., et al., *Promotion of Co/carbon sphere Fischer–Tropsch catalysts by residual K and Mn from carbon oxidation by KMnO 4.* Applied Catalysis A: General, 2012. **413**: p. 223-229.
173. Dlamini, M.W., et al., *Carbon spheres prepared by hydrothermal synthesis—a support for bimetallic iron cobalt Fischer–Tropsch catalysts.* ChemCatChem, 2015. **7**(18): p. 3000-3011.

Chapter 3: Experimental and characterization procedures for the synthesis of hollow carbon spheres encapsulating osmium nanoparticles and the Fischer-Tropsch process.

3.1. Introduction

This chapter describes the experimental procedure used to synthesize osmium nanoparticles encapsulated in hollow carbon spheres (Os@HCS), including the characterization and the evaluation of the catalyst in Fischer-Tropsch synthesis process. Noteworthy, synthesis of all the hollow carbon spheres used in this study was achieved by a chemical vapour deposition process and etching of the template with hydrofluoric acid.

3.2. Materials

All samples were of analytical grade and they were purchased from various sources. The potassium osmate (Anglo American), ruthenium chloride (Aldrich), ammonia solution (25%; Fluka), ethanol (98%; Merck), hexadecyltrimethylammonium bromide (CTAB; Aldrich), tetraethylorthosilicate (TEOS 98%; Aldrich), toluene (Merck) Hydrofluoric (HF 40%; Associated chemicals), formaldehyde (37%; Aldrich), urea (Promark chemicals), and deionized water were used as received.

3.3. Method for synthesizing Os@HCS

3.3.1. Synthesis of ammonium hexachloroosmate (IV), $(NH_4)_2OsCl_6$

A 500 mL round bottomed flask was charged with potassium osmate (5.00 g, 19.36 mmol) and 200 mL concentrated hydrochloric acid (35%). The reaction mixture was stirred and heated at reflux for 2 hours after which 50 mL 20% (w/v) ammonium chloride (186.9 mmol) solution was added, followed by cooling the mixture in ice. The solid which formed was isolated and washed with 80% ethanol in trying to remove potassium. Potassium was removed because it

could act as a promoter in FTS. The precipitate was recrystallized from hot concentrated hydrochloric acid. Ammonium hexachloroosmate (IV) ($(NH_4)_2OsCl_6$) crystallised as deep red-brown cubes which were washed with absolute ethanol (8.1 g, 95% yield).

3.3.2. Synthesis of silica spheres

The silica spheres were synthesized via the Stöber method, where a silica precursor (TEOS) undergoes hydrolysis followed by nucleation and growth to form silica spheres [54, 192-195]. The spheres were prepared by mixing 20 ml of water, 200 ml of ethanol, and then adding 10 ml of ammonia solution into the mixture. The solution was prepared in a 250 ml conical flask and stirred for 10 min. The monodispersed silica spheres were prepared by adding 15 ml of TEOS slowly into the solution and the mixture was stirred for 6 hours to form mesoporous SiO_2 (yield of 4.00g).

3.3.3. Synthesis of Os/SiO_2

Two methods were applied in the preparation of Os nanoparticles deposited on silica template; they were: homogenous deposition precipitation and incipient wetness impregnation. Different Os loadings were prepared on the silica template (1, 5 and 10% of Os/SiO_2).

In the homogenous deposition precipitation method, $(NH_4)_2OsCl_6$ crystallites were dissolved in 16.02 ml (2M) ethanol and mixed with 0.4 g of urea and 4 g of SiO_2. The mixture was dispensed into 250 ml of deionised water in a round-bottom flask and sonicated for 30 minutes. Homogeneous deposition precipitation of Os was done by stirring and refluxing the solution in a 95 °C oil bath for 12 hours. The product was filtered, then dried in an oven at 100 °C overnight, and then collected as a dry powder (Os/SiO_2).

In wetness impregnation, 0.0693 g of $(NH_4)_2OsCl_6$ crystallites were dissolved in 5 ml of distilled water in a beaker and the solution was ultrasonicated. The prepared solution was then subsequently added drop-wise to a 1 g of SiO_2 support contained in a beaker. The resulting mixture was ultrasonicated for 15 minutes and kept at room temperature. After ultrasonication,

the solution was left to dry in an oven at 100 ℃ overnight and then collected as a dry powder (Os/SiO_2).

3.4. Experimental procedure for synthesizing hollow carbon spheres

3.4.1. Gases

Argon Baseline 5.0 (99.9%) gas was used in the Chemical Vapour Deposition (CVD) process, it was purchased from AFROX (African Oxygen) Ltd. The flow rate of the gas was kept at 100 ml/min for the duration of the CVD reaction.

3.4.2. Chemical vapour deposition reactor set-up

The synthesis of carbonized osmium particles supported on silica spheres (Os/SiO_2) was carried out by using CVD (Fig 3.1). A mass of 1 g of Os/SiO_2 coated spheres were placed inside a quartz boat in the centre of a quartz tube of a horizontal furnace. The furnace temperature was ramped to 950 ˚C at a heating rate of 10 ˚C/min, while argon, as a carrier gas was flowed at a constant rate of 100 ml/min through the reactor. Once the furnace reached 950 ˚C, the carrier gas bubbled through the toluene and both the carrier gas and toluene passed through the horizontal furnace reactor for 2 hours where the reaction took place (Fig 3.1). After the reaction, the products were cooled to room temperature under a constant carrier gas flow rate of 100 ml/min. The resultant product, $Os/SiO_2@C$, was then treated with HF for 24 hours to remove silica template in attempt to produce Os nanoparticles encapsulated inside the hollow carbon spheres, Os@HCS (scheme 3.1).

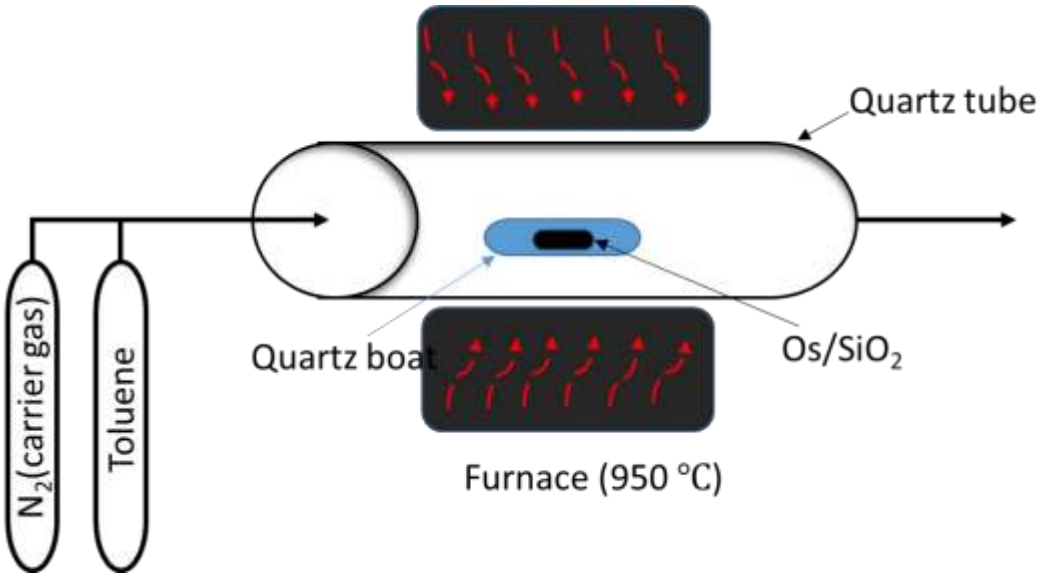
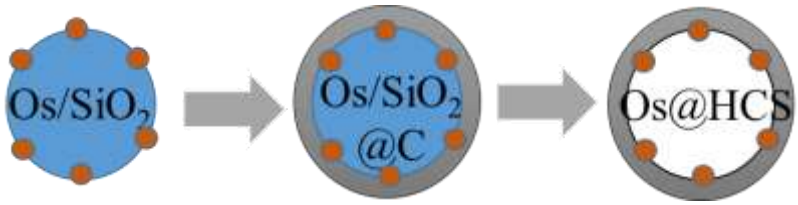


Figure 3. 1: Horizontal CVD set up.



Scheme 3. 1: Schematic illustration of Os@HCS synthesis

3.5. Structural characterization

The following techniques were used to probe the chemical and physical properties of the synthesised materials.

3.5.1. Transmission electron microscopy (TEM)

TEM micrographs were obtained using a high resolution FEI Tecnai spirit (T12) transmission electron microscope operating at 120 kV fitted with a TVIPS-TEM-Cam F416 retractable transmission electron microscope camera. The catalyst for analysis was prepared by dispensing the catalyst in methanol followed by ultrasonication for 30 minutes in an Eppendorf tube. After

ultrasonication the sample was transferred onto a copper grid and the solvent was dried prior to analysis. TEM micrographs were to study the morphology and the sizes of both the support and catalyst particles.

3.5.1. Scanning electron microscope (SEM)

SEM micrographs were obtained by using a FEI Nova Nanolab 600 FIB/Scanning electron microscope operating at 30 kV. In preparation of the catalyst, the specimen was mounted on a carbon tape. The samples were then coated with a gold-palladium alloy layer before analysis. The principal behind coating was to ensure that the samples were electrically conductive, thus minimizing charging and other related imaging artefacts during SEM analysis.

3.5.2. Powder X-ray diffraction (PXRD)

The bulk composition of the catalyst was analysed using a Bruker D2 phaser equipped with a Lynxeye PSD detector. The radiation used was Co-Kα radiation (λ = 0.178897 nm) at 30 kV and 10 mA. The goniometer of the diffractometer was 70.7 mm. The X-ray scan ranged from 5 – 90^{o} 2θ in 0.0260 steps and ran for 10 minutes.

3.5.3. Inductively coupled plasma optical emission spectroscopy (ICP-OES) analysis

ICP-OES analysis was performed to obtain the elemental analysis of the sample.

3.5.4. Thermogravimetric analysis (TGA)

Thermal stability of the samples was monitored by using a Perkin-Elmer STA6000 Thermo-gravimetric analyzer. For analysis $\pm$10 mg of the sample was placed in a ceramic pan, which was then placed in the furnace of the instrument. The samples were heated at 10 °C/min under

air or nitrogen gas, at a flow rate of 20 mL.min^{-1}. The temperature was increased from 30 °C to 900 °C to measure the weight change/loss. The principal behind TGA is to monitor the thermal decomposition of the samples by weight change as a function of time and temperature.

3.5.5. Temperature programmed reduction

TPR profiles were obtained by using a Micrometrics AutoChem II instrument fitted with a thermal conductivity detector and three Brooks mas-flow controllers. Prior to analysis ± 100 mg of the sample was degassed at 150 °C for 1 hour under helium gas at a flow rate of 50 ml/min. TPR analysis was performed using 5% hydrogen gas in argon (50 ml/min) at 1 bar pressure while the temperatures was raised to 900 °C at a heating rate of 10 °C/min. The principal behind TPR was to determine the degree of reduction and reducibility of the catalysts.

3.5.6. Brunauer-Emmet and Teller (BET) surface area measurement

Determination of the catalyst surface area, pore volume and pore size distribution was achieved using a Micromeritics Tristar 3000. Prior to analysis ± 0.2 g of the samples were first degassed at 120 °C for 4 hours in a nitrogen gas using a Micrometrics Flow Prep 060 unit. The measurements were done via monitoring the isothermal adsorption of N_2 at liquid nitrogen temperature. The Brunauer, Emmett and Teller (BET) equation was used to calculate the surface area with a relative pressure ranging from 0.05 to 0.30. The specific adsorption pore volumes were calculated using the Barrett–Joyner–Halenda (BJH) method [196].

3.5.7. Fourier transform infrared spectroscopy (FTIR)

Fourier transform infrared spectroscopy (FTIR) was used to obtain the infrared spectrum of the carbon material. From the infrared spectrum various functional groups were seen. The analysis was conducted on a Burker Trensor 27 spectrophotometer fitted with an attenuated total reflection accessory. The spectra data were collected in the range of 550 - 4000 cm^{-1} with a resolution of 4 cm^{-1} and an average of 64 scans per spectra.

3.6. Experimental procedure for Fischer-Tropsch synthesis

3.6.1. Gases

All gases used in the Fischer-Tropsch synthesis (FTS) experiments were supplied by AFROX (African Oxygen) Ltd and were of ultra-high purity (UHP) grade. The synthesis gas (syngas) used comprised of a gas mixture of 60% hydrogen, 30% carbon monoxide and 10% nitrogen gas. This was done to ensure a H_2:CO ratio of approximately 2:1 in the feed gas. Nitrogen was used as an internal standard gas to ensure accurate mass balance calculations since it was non-reactive under FTS conditions. Hydrogen gas was used to reduce the catalyst prior to FTS reaction. Argon gas was used for the offline gas chromatography, whereas, air, nitrogen and hydrogen gasses were used for online gas chromatography analysis.

3.6.2. Reactor setup

The reactor setup for the FTS is shown schematically in Fig 3.2. The system consists of a fixed bed reactor, with all gases supplied from a gas cylinders with pressure regulators installed at different location, before and after the reactor. The pressure regulators ensured that the gas going into the reactor was of the required pressure at any given moment. The fixed bed reactor was made up of a 16 mm stainless steel tube with a frit inserted in the middle to serve as a support for the catalyst bed, Fig 3.3. A thermocouple was inserted into the catalyst bed for temperature regulation, and Swagelok fittings were used for all gas line fittings. All gas lines used in the system consisted of a 1/4“ and 1/8“ stainless steel tubing. Quartz wool was placed on the frit and the catalyst rested on the wool (sieved by 150 µm sieve). Then the reactor was filled with steel balls so as to serve as a heat conductor to enable homogenous heat distribution in the reactor. All gas lines after the reactor were kept at 150 °C. Two knockout pots or traps were installed after the reactor. The first knockout pot was maintained at 150 °C to serve as a wax trap and to avoid line blockage. The second knockout pot was set at room temperature to serve as a cold trap and used to trap water and high molecular weight hydrocarbons (i.e oil products). The gaseous products were directed to an online gas chromatograph equipped with a thermal conductivity detector (TCD) and the oil products were directed to an offline gas chromatograph equipped with a flame ionization detector (FID).

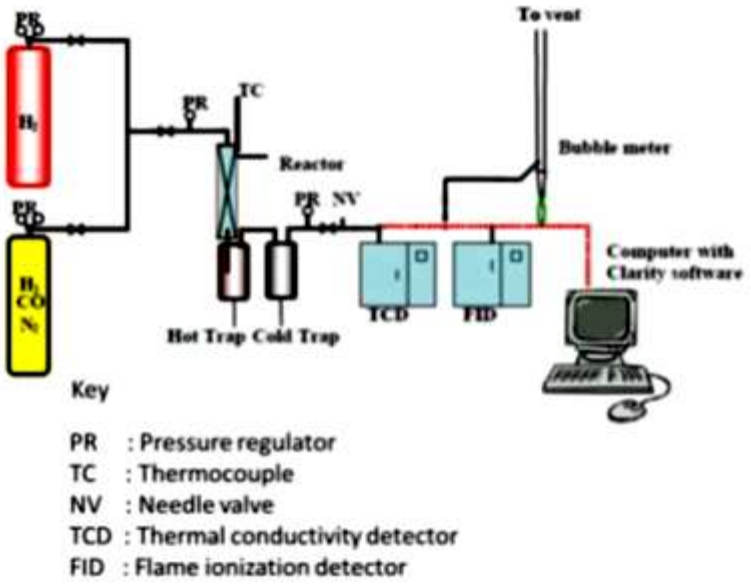


Figure 3. 2: Schematic illustration of the reactor and rig setup.

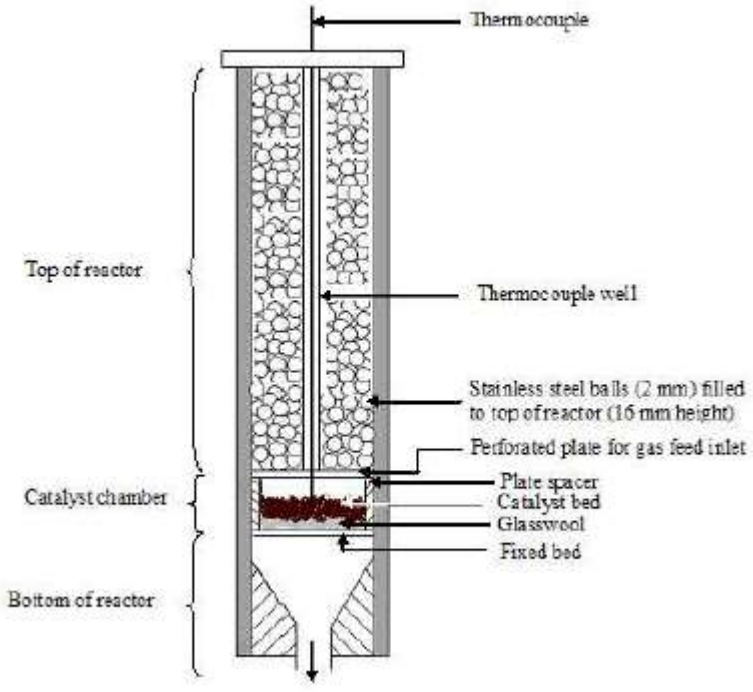


Figure 3. 3: Schematic diagram of a fixed bed reactor.

3.6.3. Catalytic experiments

A fixed bed reactor was used to obtain the hydrocarbon products. The catalyst (0.5 g) was added into the reactor and reduced in-situ by hydrogen gas passing at 220 ^{0}C for 16 hours, at a flow rate of 45 ml/min^{-1} prior to FTS.

After the reduction step the reactor was cooled to room temperature and then followed by the FTS reaction. In the FTS reaction the pressure was gradually increased to 10 bar with an introduction of syngas (29.2% CO, 10.3 of %N_2 and balance of H_2) at a flow rate of 20 ml/min^{-1}. The temperature was ramped to the desired temperatures (220, 250, 300 ^{0}C) at a ramping rate of 1 ^{0}C/min. The FT process was then conducted at steady state for 50 hours at each temperature (220, 250 and 300 ^{0}C). Gas chromatography (GC) was used for analysis of the products produced.

3.6.4. Gas chromatography calibration and product analysis

Prior to all catalytic experiments, the gas chromatograph equipment was calibrated using two gases; syngas (29.2% CO, 10.3 of %N_2 and balance of H_2) and a six-gas mixture (2.5% CH_4, 0.2% C_2H_4, 0.5% C_2H_6, 10% CO, 5% CO_2 and balance of Ar). Typical GC traces are shown in Fig 3.4, Fig 3.5, Fig 3.6 and Fig 3.7. The data was recorded from the TCD and FID detectors during calibration and FT synthesis. The peak areas corresponding to each analyte detected during the calibration was used to compute the amount that corresponded with each analyte in the FT product stream. Clarity (v.2.5) software was used to compute the gas traces. GC conditions for analysis are summarized in Table 3.1

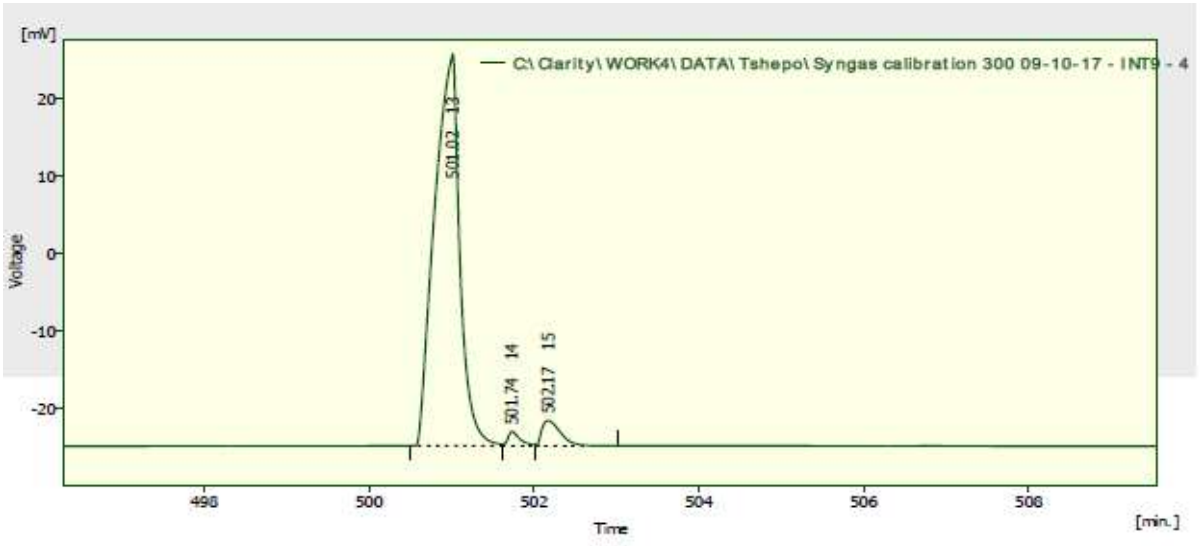


Figure 3. 4: A GC-TCD trace recorded during syngas calibration H_2 (60%), N_2 (10%) and CO (30%).

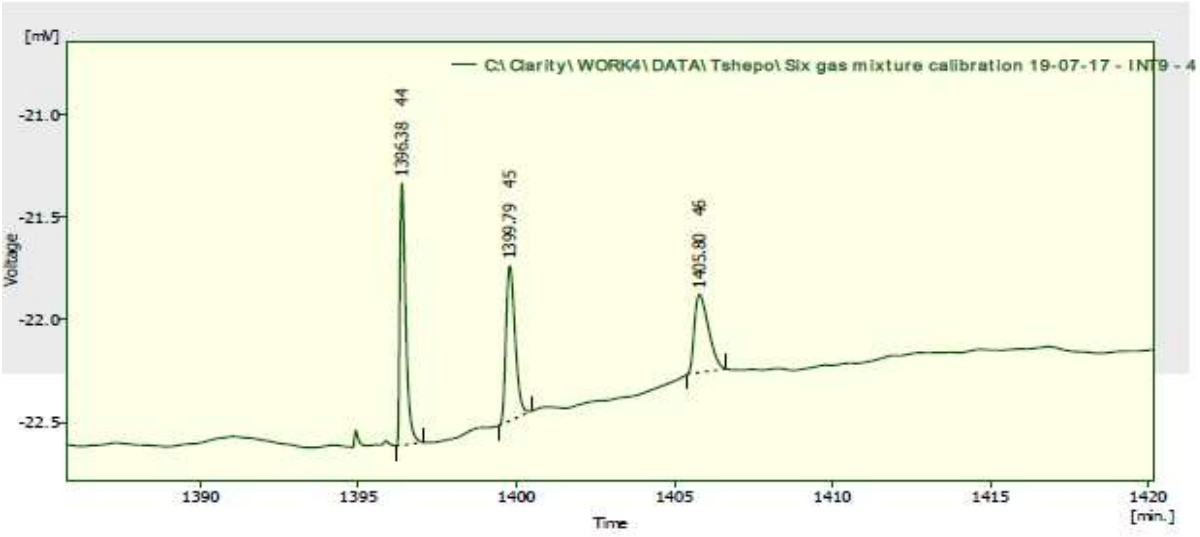


Figure 3. 5: A GC-FID trace recorded during the six-gas mixture calibration

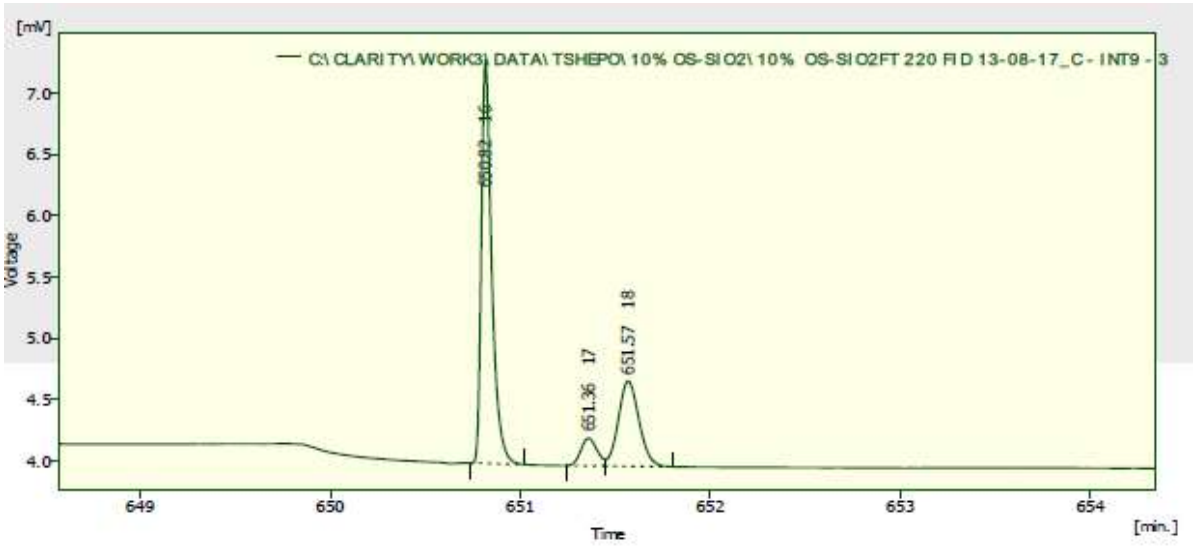


Figure 3. 6: A GC-FID trace recorded during a typical FTS run.

Table 3. 1: Specification of the GC operating conditions

Gas chromatograph (on-line)	
Make	PYE Unicam (Series 204)
Detector	Thermal conductivity detector (TCD)
Detector temperature	220 ^{0}C
Column type	Packed, stainless steel, 2 m x 2.2 mm, O.D. = 1/8”
Stationary phase	Carbosieve, S-II, 60-80 mesh
Sample valve temperature	150 ^{0}C
Carrier gas	Ar, 20 ml/min
Oven temperature	250 ^{0}C (isothermal)
Gas chromatography (on-line)	
Make	Hewlett Packard 5890
Detector	Flame ionization detector (FID)
Detector temperature	220 ^{0}C
Column type	Packed, stainless steel, 2 m x 2.2 mm, O.D. = 1/8”
Stationary phase	ZB-5, 80/100 mesh
Sample valve temperature	150 ^{0}C
Carrier gas	Ar, 20 ml/min
Oven temperature	250 ^{0}C (isothermal)

Gas chromatography (off-line)	
Make	Varian 3700
Detector	Flame ionization detector (FID)
Detector temperature	350 ^{0}C
Column type	30 m x 5 μFT, O.D. = 0.53 mm
Stationary phase	ZB-1
Sample valve temperature	250 ^{0}C
Carrier gas	N_2, 20 ml/min
Oven temperature	Heat to 300 ^{0}C (ramping rate: 10 ^{0}C/min), and hold at temperature for 3 hours

3.7. Mass balance calculations

Before carrying out the FTS, the amount of syngas in the inlet stream was determined as outlined in section 3.4.4. The mass balance calculation performed were similar to those performed by Bahome, Hexana, Phadi and Price [150, 197-199]. Mass balance calculations were performed based on the carbon content under steady state conditions for about 50 hours. During FTS the amount of unreacted syngas and the low boiling products from the outlet stream were analysed on-line.

The percentage of CO converted was calculated as follows:

$$\%CO = \left\{\frac{CO_{in} - CO_{out} \times \left[\frac{N_{2,in}}{N_{2,out}}\right]}{CO_{in}}\right\} \times 100\% \qquad \text{Eqn 3.1}$$

Where CO_{in} and $N_{2,in}$ are the calibration peak areas for CO and N_2 from the inlet stream, respectively, and CO_{out} and $N_{2,out}$ are the peak areas measured for CO and N_2 during FTS as outlet stream, respectively.

The outlet flow rate (F_{out}) from the reactor was measured using a bubble soap flow meter. From this the calculation of the inlet feed flow rate (F_{in}) was calculated. A gas contraction factor was used;

$$F_{in} = \left\{X.\frac{N_{2,out}}{N_{2,in}}\right\} F_{out} \qquad \text{Eqn 3.2}$$

where $X_{N_2,in}$ and $X_{N_2,out}$ are the mole fraction of N_2 in the six gas mixture (calibration gas) and the FTS run, respectively. F_{in} and F_{out} are the total feed inlet and exit flow rates, respectively, and expressed in mols/s.

The total number of carbon moles in the feed stream in the entire mass balance period was calculated as follows;

$$N_{C,in} = F_{in}.t.X_{CO,in} \quad \text{Eqn 3.3}$$

Where - $N_{c,in}$ are the total number of moles fed into the reactor

F_{in} is the total feed flow rate in mol/s

t is the total mass balance time

$X_{CO,in}$ is the mole fraction of CO in the feed gas

The mass balance calculations were accepted within the range $100 \pm 5\%$ in each case and calculated as follows;

$$\%\ carbon\ balance = \left\{\frac{N_{C,out}}{N_{C,in}}\right\} \times 100 \quad \text{Eqn 3.4}$$

For the mass balance to be correct, $N_{C,in}$ should be equal or approximately equal to $N_{C,out}$.

The rate of CO conversion during the steady state period was computed as follows;

$$-r_{CO} = \frac{F_{CO,in} - F_{CO,out}}{m_{cat}} \quad \text{Eqn 3.5}$$

where $F_{CO,in}$ and $F_{CO,out}$ are the molar flow rates (mol/min) of CO fed into the reactor or exiting the reactor, respectively, r_{CO} is the rate of CO conversion ($mol.min^{-1}.g_{catalyst}^{-1}$), and m_{cat} is the mass (g) of the catalyst.

From the gaseous products, the selectivity of individual hydrocarbons were calculated as follows;

$$Sel(\theta) = \frac{[n_C]_\theta}{-r_{CO}.t.m_{cat}} \quad \text{Eqn 3.6}$$

where $[n_c]_\theta$ are the moles of carbon in product θ.

The selectivity of the heavy hydrocarbons (C_{5+}) was calculated based on the moles of carbon as follows;

$$S_{5+} = 100 - \Sigma(S_{CH_4} + Sc_{2-} + S_{C_2} + S_{C_3} + S_{C_4}) \quad \text{Eqn 3.7}$$

where S_{CH_4} is the selectivity for methane, and S_{C_2}, S_{C_3}, S_{C_4} are the selectivity's for hydrocarbons ranging from C_2 to C_4 products.

3.8. Reference

1. Bogush, G. and C. Zukoski, *Uniform silica particle precipitation: an aggregative growth model.* Journal of colloid and interface science, 1991. **142**(1): p. 19-34.
2. Bogush, G. and C. Zukoski, *Studies of the kinetics of the precipitation of uniform silica particles through the hydrolysis and condensation of silicon alkoxides.* Journal of Colloid and Interface Science, 1991. **142**(1): p. 1-18.
3. Lee, K., A.N. Sathyagal, and A.V. McCormick, *A closer look at an aggregation model of the Stöber process.* Colloids and Surfaces A: Physicochemical and Engineering Aspects, 1998. **144**(1): p. 115-125.
4. Stöber, W., A. Fink, and E. Bohn, *Controlled growth of monodisperse silica spheres in the micron size range.* Journal of colloid and interface science, 1968. **26**(1): p. 62-69.
5. Van Blaaderen, A., J. Van Geest, and A. Vrij, *Monodisperse colloidal silica spheres from tetraalkoxysilanes: particle formation and growth mechanism.* Journal of colloid and interface science, 1992. **154**(2): p. 481-501.
6. Barrett, E.P., L.G. Joyner, and P.P. Halenda, *The determination of pore volume and area distributions in porous substances. I. Computations from nitrogen isotherms.* Journal of the American Chemical society, 1951. **73**(1): p. 373-380.
7. Bahome, M.C., *Synthesis and use of carbon nanotubes as a support for the Fischer-Tropsch Synthesis.* 2008.
8. Hexana, W.M., *A systematic study of the effect of chemical promotors on the precipitated Fe-based Fischer-Tropsch synthesis catalyst*. 2009.
9. Phadi, T.T., *Titanium dioxide-carbon spheres composites for use as supports in cobalt Fischer-Tropsch synthesis*. 2013.
10. Price, J.G., *An investigation into novel bimetallic catalysts for use in the Fischer-Tropsch reaction.* 1994.

Chapter 4: Synthesis and characterization of osmium nanoparticles encapsulated in hollow carbon spheres

4.1. Introduction

Recently, core-shell microspheres have received considerable attention [200-202]. Core-shell and hollow carbon spheres are closely related, in that the core-shell structure involves the encapsulation of a core by a "shell" (hollow carbon sphere) which is chemically different and therefore allows for the fabrication of materials with multiple functionalities. Various synthesis methods to make core-shell microspheres have been proposed and most approaches rely on a template-assisted synthesis [200-203]. A core-shell catalyst containing a metal nanoparticle core is expected to show a minimum support effect if an inert hollow shell such as a hollow carbon sphere is employed.

Hollow carbon spheres (HCSs) have been receiving increasing attention in the field of science and engineering, due to their unique physicochemical properties such as low density, high compressive strength, chemical inertia, thermal insulation and large inner space or surface area[73]. Applications of HCSs include gas storage media [204], supports for catalysts [205] and drug delivery devices [206]. Synthesis of HCSs rely on a template assisted synthesis. Generally the synthesis of a HCS via the templating route requires (1) production of the template; (2) simple modification of the template; (3) uniform encapsulation of the template by a shell precursor; and (4) a facile method for the removal of the template [40-42]. Stöber silica spheres are the most effective templates used in the synthesis of HCSs with well-defined pore structures [207]. The advantage of using a hard template (i.e. Stöber silica sphere) over the soft template alternatives is the easy control of the size, morphology, and structure of the resultant HCSs [208].

Encapsulation of metal nanoparticles inside HCSs involves, (1) the deposition of metal nanoparticles on the template, (2) carbonization of the deposited template, and (3) removal of the template. Generally the deposition of the metal nanoparticles on the support or template can be achieved by two methods: incipient wetness impregnation (WI) and homogenous deposition precipitation (HDP). The carbonization procedure involves the chemical vapour deposition process which was explained in detail in *section 3.3.4.2*. Removal of the template

after formation of the carbon shell-template complex entails the dissolution or etching of the silica via the use of chemicals such as HF or NaOH.

Wetness impregnation (WI), also called capillary impregnation or dry impregnation, is a commonly used technique for the synthesis of heterogeneous catalysts. Typically, the active metal precursor is dissolved in an aqueous or organic solution. Then a volume of the metal-containing solution is added to a catalyst support with the volume equal to the pore volume of the sample pores. Capillary action draws the solution into the pores. The solution added in excess of the support pore volume causes the solution transport to change from a capillary action process to a diffusion process, which is much slower. The catalyst can then be dried and calcined to drive off the volatile components within the solution, depositing the metal on the catalyst surface. The maximum loading is limited by the solubility of the precursor in the solution. The concentration profile of the impregnated compound depends on the mass transfer conditions within the pores during impregnation and drying.

Homogenous deposition precipitation is a process where a controlled homogenous precipitation technique is applied in the presence of a homogeneously distributed finely divided particulate supporting material. The metal or metal compound is deposited on the surface of the support particles. Typically, the deposition precipitation process is affected by a number of variables which include the homogeneous changes in the pH of the solution, introduction of the metal component to be precipitated, oxidation or reduction techniques, decomplexation to an insolubilizable metal ion, by introduction of precipitating ions, etc. The process requires appropriate conditions to substantially avoid any stable free nucleation and crystal development in the solution phase, and to cause nucleation and particle formation substantially only on the supporting material surfaces. The deposited metal or metal compound is obtained in the form of discrete very small particles, homogeneously distributed over the support surface, which gets either crystallographically or electrostatically adhered to the support particle. The resulting products may be used as such, or may be treated by subsequent heating, oxidation, or reduction steps to be converted into still further useful products. The products obtained are highly valuable for their catalytic activity, and, when ferromagnetic deposited particles are produced, highly advantageous properties that are related to magnetocrystalline anisotropy are obtained.

Hollow carbon spheres have emerged as support materials in heterogeneous catalysis due to their relative chemical inertness that allows easier reducibility and increased metal catalytic activity [18, 19]. Hence, HCSs can be considered as nanoreactors [209-211]. Since, catalysis

involves reactions on a metal surface, access of reactants to the metal encapsulated in the nanoreactors is determined by the porosity of the carbon shell. The shells can be mesoporous (2-50 nm) or microporous (< 2 nm) carbon shells [32, 212]. Encapsulation of the metal nanoparticles can limit metal sintering under reaction conditions [32, 212] and can lead to containment of fragmented catalyst particles [213]. The concept of using catalytic metals contained inside nanoreactors has been demonstrated [32] but to date, no reports on encapsulating osmium nanoparticles inside HCSs have been reported.

In this chapter, the synthesis and characterization of osmium nanoparticles encapsulated in HCS nanoreactors is described and discussed. Assessment of the size, morphology and uniformity of HCSs as well as the Os particles is described. The effects of different metal to silica precursor support deposition methods are discussed. Lastly, the influence that the above-mentioned parameters have on the synthesis of osmium nanoparticles encapsulated inside HCSs is discussed.

4.2. Experimental

4.2.1. Synthesis of Stöber silica sphere supporting Os (Os/SiO_2)

The Stöber silica spheres to be used as templates in the synthesis of hollow carbon spheres were fabricated using the Stöber method as described in *section 3.3.2*. An Os precursor (NH_3OsCl_6) was used to deposit Os onto synthesised Stöber silica spheres via two different methods. These methods were wetness impregnation and homogenous deposition precipitation. In the wetness impregnation method distilled water was the solvent used, whereas, in the homogenous deposition precipitation method urea in water was used as the precipitating agent. Different Os loadings were prepared on the silica template (5 and 10% Os/SiO_2).

4.2.2. Synthesis of Os nanoparticles encapsulated in HCSs (Os@HCS)

The Os loaded on a SiO_2 template was carbonized using toluene in a chemical vapour deposition procedure as described in *section 3.3.4.2*. The prepared catalyst was etched with hydrofluoric acid at room temperature to remove the silica and produce Os@HCS.

Catalyst codes used to describe the synthesized materials were as follows:

5% Os@HCS WI. Os catalyst encapsulated in HCS, prepared from 5% Os nanoparticles loaded onto a SiO_2 template via a wetness impregnation (WI) method.

5% Os@HCS HDP. Os catalyst encapsulated in HCS, prepared from 5% Os nanoparticles loaded onto a SiO_2 template via a homogenous deposition precipitation (HDP) method.

10% Os@HCS WI. Os catalyst encapsulated in HCS, prepared from 10% Os nanoparticles loaded onto a SiO_2 template via a wetness impregnation (WI) method.

10% Os@HCS HDP. Os catalyst encapsulated in HCS, prepared from 10% Os nanoparticles loaded onto a SiO_2 template via a homogenous deposition precipitation (HDP) method.

4.2.3. Characterization techniques

TEM, SEM, EDS, FTIR, XRD, ICP-OES, TGA, BET and TPR techniques were used to characterize and analyse the synthesized materials. The description of the instruments used is given in *chapter 3*.

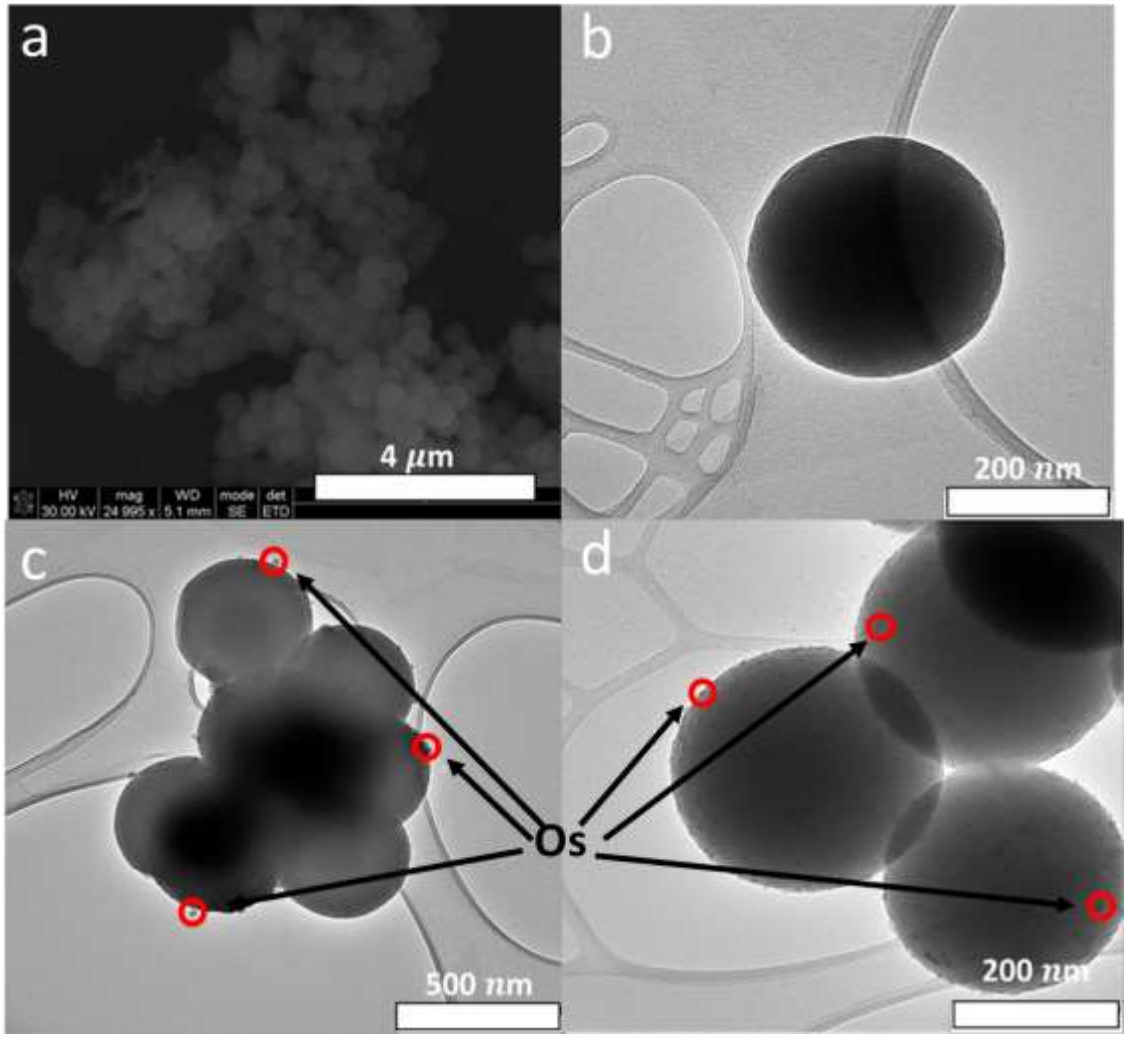
4.3. Results and discussion

4.3.1. Electron microscopy

The electron microscopy images used in the following section were recorded on the 5% Os loaded on silica sphere template (Os/SiO_2) precursor used to prepare the 5% Os encapsulated in hollow carbon sphere (Os@HCS) materials.

4.3.2. Os nanoparticles loaded on Stöber silica spheres (5% Os/SiO_2)

The mesoporous silica spheres to be used as templates in the synthesis of hollow carbon spheres were fabricated using the Stöber method as described in *section 3.3.2*. Typical SEM and TEM images of silica Stöber spheres are shown in Fig 4.1 (a) and (b), respectively. The images illustrate that the synthesized silica spheres were spherical in morphology with an average diameter of 450 ± 20 nm (Fig 4.1 (e)). The synthesized silica spheres were relatively uniform in size and monodispersed in size.



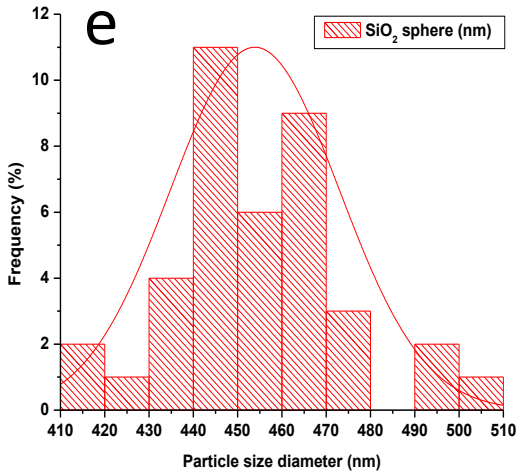


Figure 4. 1: Silica and Os/SiO_2 spheres. (a) SEM image of Stöber silica spheres, (b) TEM image of Stöber silica spheres, (c) TEM image of 5% Os/SiO_2 prepared via wetness impregnation method, and (d) TEM image of 5% Os/SiO_2 prepared via homogenous deposition precipitation method. (e) SiO_2 particle size distribution.

The effects of different loading procedures of Os on SiO_2 are shown in the TEM images in Fig 4.1 (c) and (d). These images show osmium nanoparticles supported on the silica template via the wetness impregnation (WI) and the homogenous deposition precipitation (HDP) methods. The data in Fig 4.1 (c) shows that Os nanoparticles loaded on the silica template via the WI method show a non-homogenous deposition and non-uniform dispersion of Os nanoparticles. In contrast, the data in Fig 4.1 (d) shows that Os nanoparticles loaded on the silica template via the HDP method give a more homogeneous deposition and a uniform dispersion of Os nanoparticles. In the HDP method it was possible to load the particles homogenously on the silica spheres, because OsO_2 particles are able to bind on the silica spheres while the support is still in the urea containing solvent. Overall, the presence of a large amount of functional groups (i.e. Si-OH groups) on the silica sphere surface facilitated the loading of the nanoparticles onto the surface of the silica template.

4.3.3. Carbonized Os nanoparticles loaded on Stöber silica spheres (5% Os/SiO2@C)

Characteristics of hollow carbon sphere supports such as the morphology, porosity, and durability are quite crucial to understanding the catalytic performance of a catalyst [214]. These characteristics are determined by the way in which the support is synthesised. In the current study, hard templates (i.e. Stöber silica spheres) were carbonized using toluene as the carbon source using chemical vapour deposition (CVD). The gas flow rate was 100 ml/min and the reaction time was 2 hours at a temperature of 950 °C. Illustrated in Fig 4.2 (a) and (b) are the SEM and TEM images of carbonized Os/SiO_2@C made from Os/SiO_2 HDP, respectively. The diameter of the carbonized material was 500 ± 50 nm which involves a carbon layer being added to the uncarbonized sphere (Os/SiO_2, 450 ± 20 nm). It can be seen from Fig 4.2 (b) that the composite consists of a silica core which is uniformly encapsulated by the carbon shell. In Fig 4.2, it can be seen from both SEM and TEM images that the Os/SiO_2@C were relatively uniform in size and shape which suggests that successful evenly distributed carbon deposition had occurred.

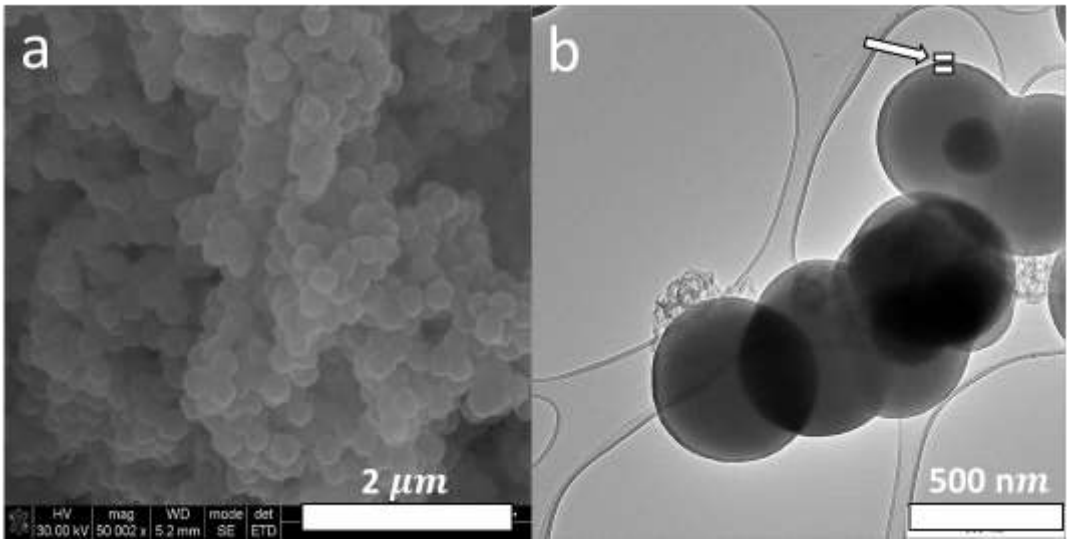


Figure 4. 2: (a) SEM and (b) TEM images of 5% Os/SiO_2@C from 5% Os/SiO_2 prepared via the homogeneous deposition precipitation method.

4.3.4. Os nanoparticles encapsulated inside hollow carbon spheres (5% Os@HCS)

A selective etching technique was applied to remove the template from the carbonized material. The selective technique removes the sacrificial core [215]. In the current study 10% hydrofluoric acid (HF) was the etching reagent used to remove the silica template from Os/SiO_2@C to obtain a carbon shell encapsulating Os nanoparticles, forming the Os@HCS catalyst.

Illustrated in Fig 4.3 (a) and (b) are the SEM images of 5% Os@HCS loaded via homogenous deposition precipitation and wetness impregnation methods, respectively. It can be seen from the SEM images that the 5% Os@HCS catalyst from both methods had a hollow spherical structural morphology. The morphology of the HCSs was uniform, however, some of the spheres were broken and this clearly shows the presence of the inner hollow cores. The broken spheres were undesirable because this means Os particle are also found on the outside of the HCS and this would affect the results from FT reaction studies. The SEM images in Fig 4.3 (a) show some Os nanoparticles dispersed inside or outside the HCSs (red circle). The presence of Os nanoparticles, if they were inside or outside the HCSs can clearly be determined by TEM analysis.

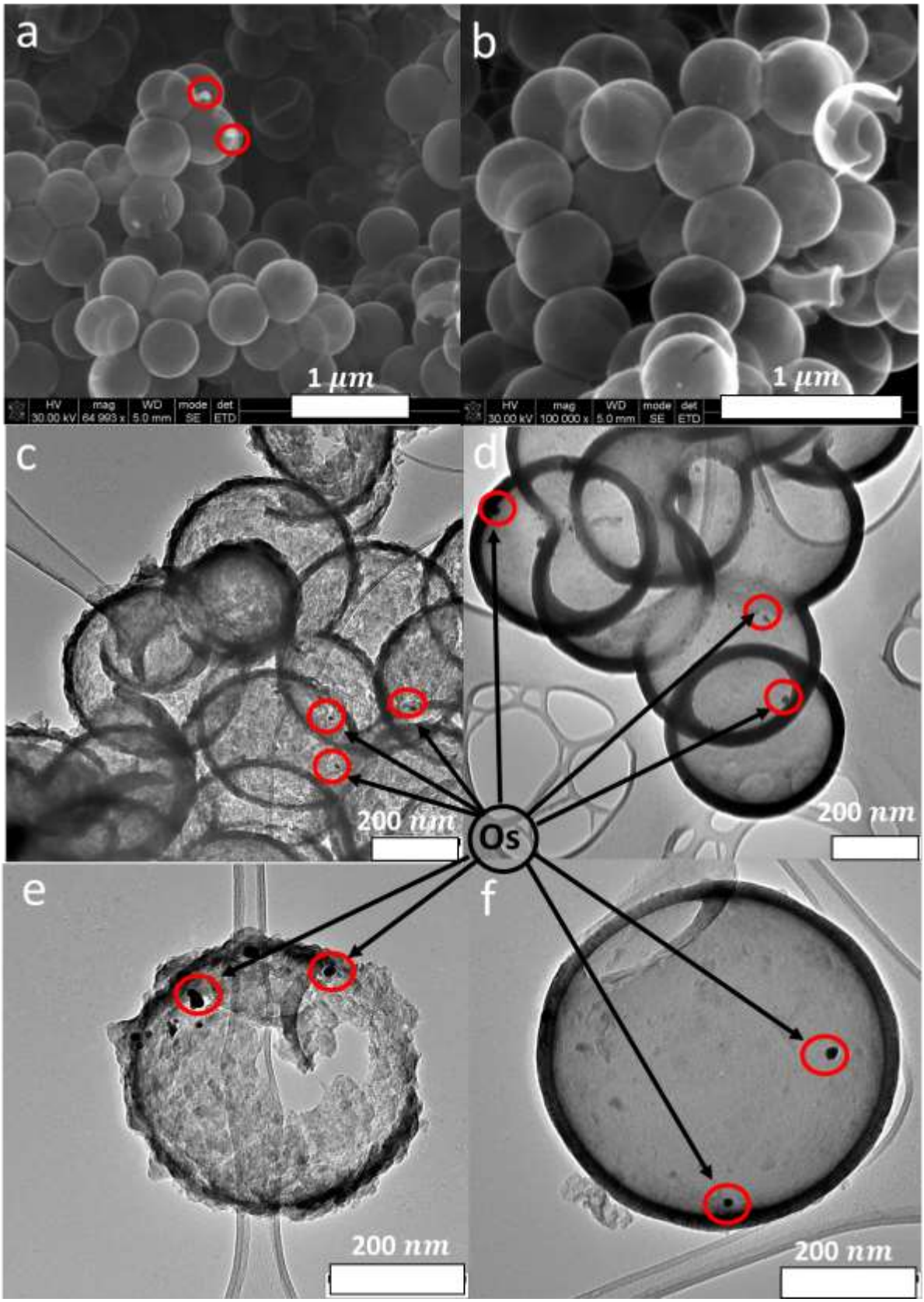


Figure 4. 3: (a) and (b) SEM images of 5% Os@HCS prepared via homogenous deposition precipitation and wetness impregnation method, respectively. (c) and (d) TEM images of 5%

Os@HCS prepared via homogenous deposition precipitation and wetness impregnation method, respectively. (e) and (f) up close TEM images of 5% Os@HCS prepared via homogenous deposition precipitation and wetness impregnation method, respectively

Illustrated in Fig 4.3 (c-f) are the TEM images of 5% Os@HCS prepared via homogenous deposition precipitation (HDP) and wetness impregnation (WI) methods. In Fig 4.3 (c-f) the carbon shell encircles one or multiple metal nanoparticles, which is a typical observation found in a core-shell structures [216-218]. It can be seen that the Os nanoparticles were well dispersed and indeed encapsulated inside the interstitial space of the carbon shell. The average diameter of the spheres produced for 5% Os@HCS HDP and 5% Os@HCS WI was 455 $\pm$ 33 nm and 560 $\pm$ 26 nm, respectively; and the carbon shell thickness was 19 $\pm$ 3 nm and 20 $\pm$ 2 nm, respectively. The average particle size distribution of Os nanoparticles encapsulated from TEM images including those shown in Fig 4.3 (c) and (d) were 11 $\pm$ 4 nm and 16 $\pm$ 5 nm, respectively, as shown in Fig 4.4. It can be seen that some of the HCSs were indeed broken and this clearly suggests that some of the Os nanoparticles could be found outside the HCS shell as seen in Fig 4.3 (e).

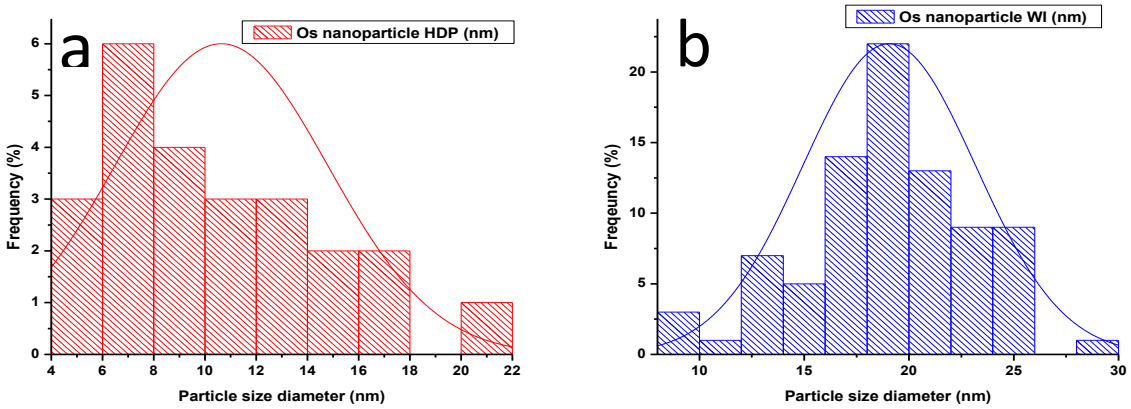


Figure 4. 4: Os nanoparticle size distribution from (a) Os@HCS HDP and (b) Os@HCS WI.

4.3.5. Energy dispersive X-ray spectroscopy

The elemental composition of the synthesised nanostructures was determined by energy-dispersive X-ray (EDX) spectroscopy. The EDX spectrum of the Stöber silica spheres, Os@HCS WI, Os@HCS HDP and Os/SiO_2@C are shown in Fig 4.5 (spectrum 1, 2, 3, and 4 respectively). The EDX spectral analysis in all cases reveals that carbon and oxygen were present with various relative intensities. From the EDX spectrum of the Stöber silica spheres it can be seen that some Si was also present. The EDX spectrum of both Os@HCS WI and Os@HCS HDP catalysts clearly identified the presence of Os. Lastly the EDX spectrum of Os/SiO_2@C showed the presence of both Si and Os.

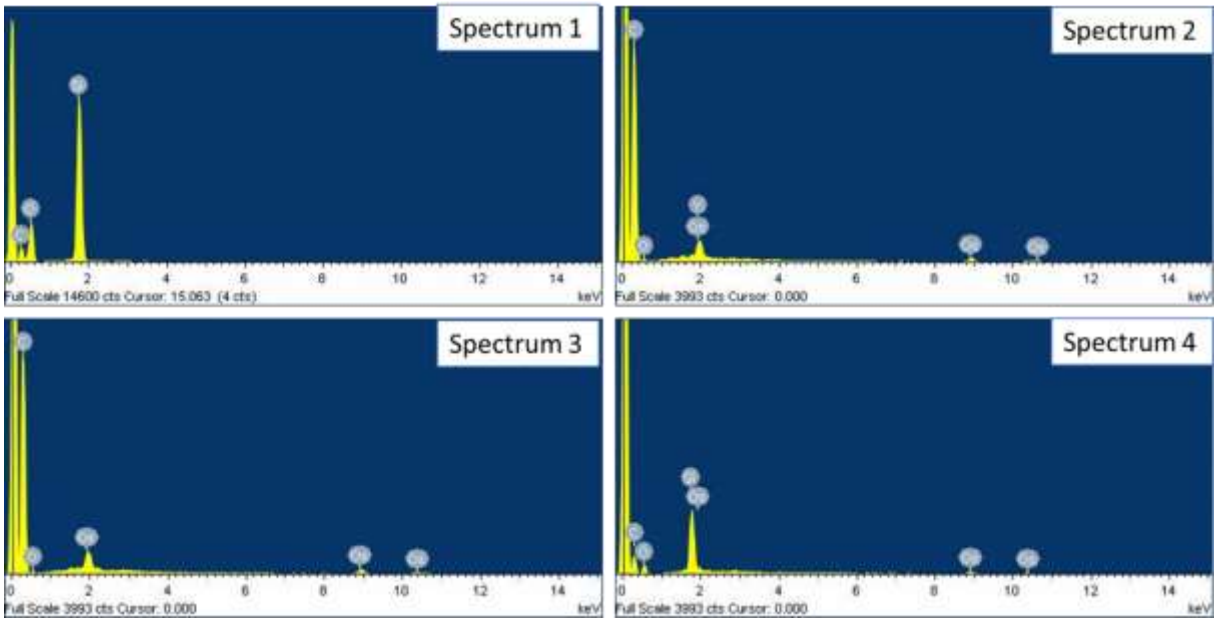


Figure 4. 5: Spectrum 1 - EDS of SiO_2; Spectrum 2 - EDS of Os@HCS synthesized via wetness impregnation method; Spectrum 3 - EDS of Os@HCS synthesized via homogenous deposition precipitation method; and Spectrum 4 - EDS of Os/SiO_2@C.

4.3.6. Fourier transformation infrared spectroscopy

Functional groups present on the surface of the products were verified by Fourier transformation infrared (FTIR) spectroscopy. FTIR spectra of Os/SiO_2, Os@HCS WI

Os@HCS HDP and HCS only are displayed in Fig 4.6. A Si-O-Si stretching vibration peak at 1398 cm^{-1} was observed for the Os/SiO_2 sample. The Si-O-Si functional group was lost upon HF treatment to give HCS and Os@HCS. Os@HCS catalysts synthesized by WI and HDP procedures all revealed the same functional groups (Fig 4.6). The functional groups present in Os@HCS were the carbonyl groups at 1768 cm^{-1} and a C-H alkyl group stretching vibration at 2903 cm^{-1}. An interesting observation is that HCSs had a similar FTIR spectra as that of Os@HCS. The presence of Os in the Os@HCS catalyst, therefore, did not affect the functional groups of HCSs since no shift in the pattern was observed. From FTIR spectra it can be confirmed that silica spheres were successfully etched after HF treatment and that the Si-O-Si stretching vibration was not present in the Os@HCS IR spectra.

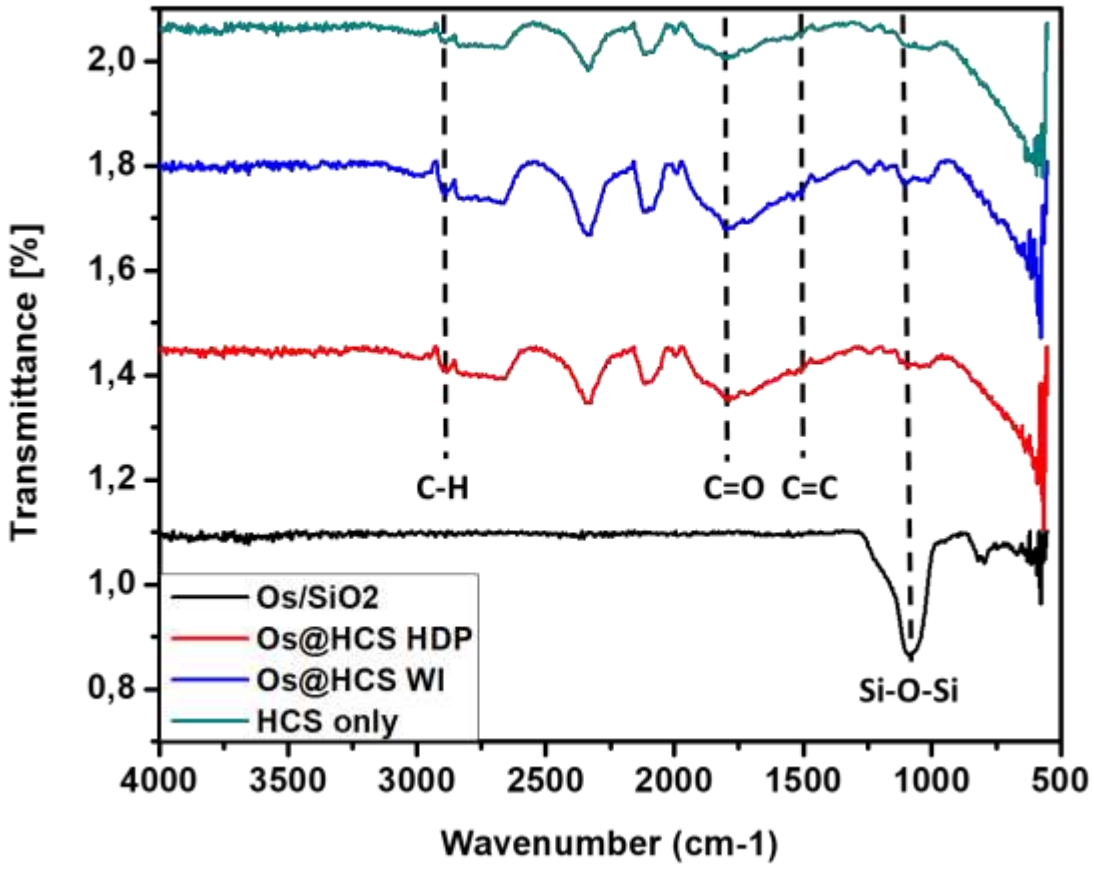


Figure 4. 6: FTIR spectra of the Os/SiO_2, Os@HCS prepared via the wetness impregnation and homogeneous deposition precipitation methods, and HCS only.

4.3.7. Powder X-ray diffraction

The identity and phase of the products produced in the study was verified by powder X-ray diffraction (PXRD) data. PXRD patterns of the synthesised 5% and 10% Os@HCS catalysts prepared via wetness impregnation and homogenous deposition methods are shown in Figure 4.7. Peaks denoted "●" represent carbon and were indexed according to the crystallographic data for amorphous carbon. Peaks denoted "★" represent osmium and were indexed according to the crystallographic data contained in the EVA software. The PXRD analyses revealed that in all cases, carbon and osmium were present in the products. The broad peak at 2θ = 30° is consistent with an amorphous (002) carbonaceous phase of the HCSs. The five sharp peaks at 2θ = 44.3°, 49.0°, 51.2°, 68.1°, and 81.6° correspond to the (100), (002), (101), (102), (110) planes of crystalline hexagonal Os (**ICSD 064993**). This means that the Os nanoparticles were reduced by carbonization under CVD. This reduced phase of Os arises since the Os nanoparticles are imbedded in the carbonaceous shell of the HCSs, which effectively protects the Os nanoparticles from being oxidized in air [219]. The planes for both carbon and Os nanoparticles were similar for different percentage loadings and different procedures employed in depositing Os nanoparticles on the silica templates. A variation in Os percentage loading is associated with an intensity variation of the peaks. In Fig 4.7, the intensity of the peak heights increased with an increase in percentage loading of Os.

The average particle sizes of the Os crystallites were calculated from the most intense reflection peak at 2θ = 51.2° using the Scherer Equation [220]:

$$\boldsymbol{D_{hkl} = \frac{\kappa \times \lambda}{\beta \times cos\theta}}$$

Where D_{hkl} is the crystallite size, β is the full width half maximum value in radians, λ is the X-ray wavelength and $\boldsymbol{\theta}$ is the Bragg angle.

A K factor of 0.9 was used and the instrument line broadening was assumed negligible.

From the Scherre equation the particle sizes of Os nanoparticles were obtained (Table 4.1).

Table 4. 1: Particle size data for osmium nanoparticles and hollow carbon spheres.

Sample name	TEM HCS diameter (nm)	TEM Os nanoparticles (nm)	XRD Os nanoparticles (nm)
5% Os@HCS WI	455	16	9.8
5% Os@HCS HDP	560	11	8.9
10% Os@HCS WI	-	-	11.3
10% Os@HCS HDP	-	-	10.2

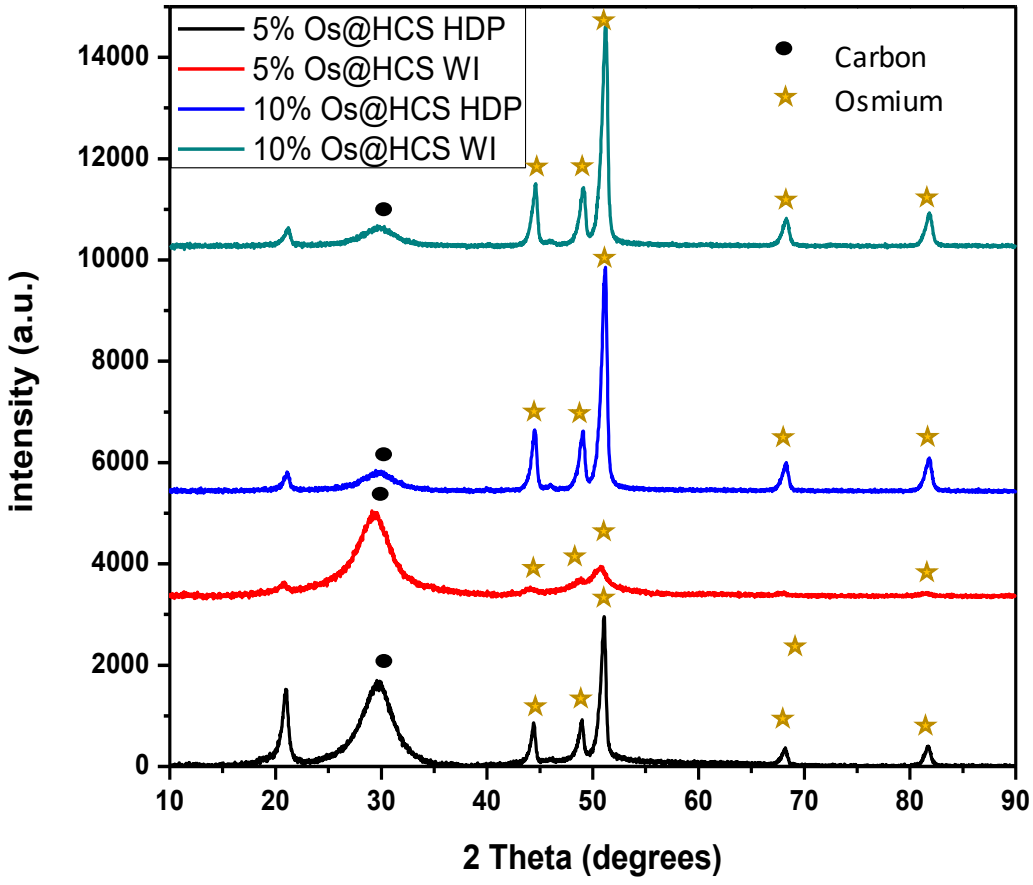


Figure 4. 7: PXRD patterns of the synthesized 5% and 10% Os@HCS prepared via the wetness impregnation and homogeneous deposition precipitation methods.

4.3.8. Thermogravimetric analysis

Thermogravimetric analysis (TGA) of the catalysts was conducted to study the efficacy of template removal and the influence of osmium nanoparticles on the thermal stability of hollow carbon sphere supports. The first derivative of the TGA thermograms for the bulk assembled synthesized catalyst curves allowed for the identification of the temperatures at where maximum weight loss occurred during the experiments. Illustrated in Fig 4.8 and 4.9 are the TGA and first derivative thermograms of the catalysts that were measured in a flow of air (heating rate of 10 °C.min^{-1}). The percentage weight loss of the synthesized catalysts were compared relative to the hollow carbon sphere support, as a function of temperature as shown in Fig 4.8.

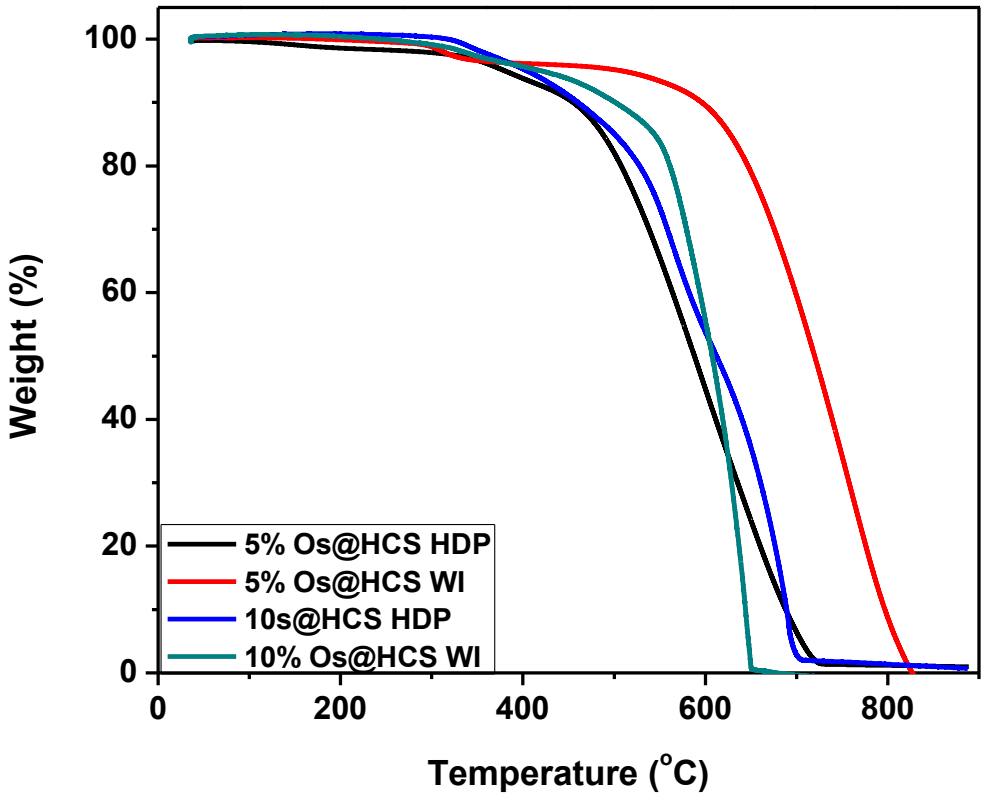


Figure 4. 8: TGA thermograms for the bulk assembled synthesized 5% and 10% Os@HCS prepared via the wetness impregnation and homogeneous deposition precipitation methods

The key observation from the TGA thermograms was that the silica template was completely removed from the carbon shell core by HF, as seen by the amount of residue remaining at 900 °C. This observation emphasizes the efficacy of silica removal by the HF, as well as the quality of the carbon shell. The observation on the efficacy of silica removal by HF has been also supported by TEM, EDS, and FTIR studies. Interestingly the 5% Os@HCS WI (red) has a different oxidation curve when compared to the other three samples (Fig 4.8). The weight loss occurred at a higher temperatures relative to the other catalysts. Of importance is the observation that no Os residue was detected. This is not unexpected as Os metal oxidizes to form OsO_4 under oxidative conditions [77], OsO_4 is volatile and is thus removed from TGA under the experimental conditions.

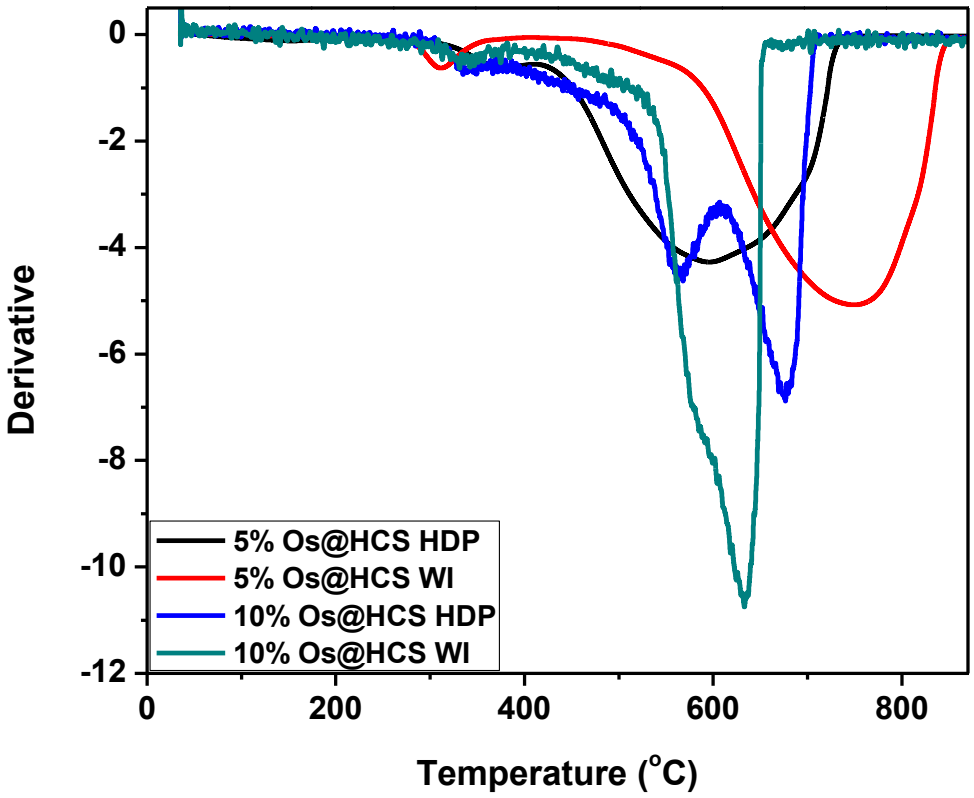


Figure 4. 9: First derivative of TGA thermograms for the bulk assembled synthesized 5% and 10% Os@HCS prepared via the wetness impregnation and homogeneous deposition precipitation methods.

An observation made from the first derivative thermograms shown in Fig 4.9 is that the decomposition temperatures occurred between 600 -700 ℃ for the catalysts synthesized. The catalysts (e.g. 5% Os@HCS WI) showed a peak between 300-350 ℃ and this is observed to be due to the loss of Os to OsO_4 [77]. The major decomposition peaks between 600 -700 ℃ can be attributed to the oxidation of carbon from the HCS support to give CO_2. The decomposition of carbon in the 5% Os@HCS WI (red) catalyst was higher at 760 ℃ when compared to the other catalysts. The derivative curves clearly reveal the presence of what appears to be two peaks between 600 -700 ℃ for three of the samples. This suggests two different types of carbon species are being removed by oxygen. A study by Xiong *et al.* reported that 5% Co/CS catalyst has two distinct regimes for the oxidation of carbon sphere (CS). It was proposed that for the Co/CS materials, the reaction $C + O_2 \rightarrow CO_2$ is catalysed by Co and during this reaction cobalt becomes reduced [221]. A similar observation of Os being reduced by the HCS was observed in *section 5.3.3*. The second oxidation peak of carbon is believed to be due to the noncatalysed oxidation of the carbon. The reason for the loss of carbon at a much higher temperature for the 5% Os@HCS WI catalyst is not known.

Repeat experiments to understand this behaviour is required. However, the volatility of the OsO_4 that is formed in the TGA is of concern. OsO_4 is a known to cause severe lung, skin and eye damage and this poses a health hazard. For this reason the TGA experiments were discontinued. Further experiments will require modifications of our TGA equipment to resolve the health issues associated with OsO_4 formation.

4.3.9. Nitrogen absorption-desorption analysis

Brunauer-Teller-Emmet (BET) measurements were used to determine the textual properties (surface area, pore volume and average pore size) of the synthesized hollow carbon sphere support and the osmium encapsulated in hollow carbon sphere materials. Fig 4.10 illustrates one example (5% Os@HCS WI) of the adsorption-desorption isotherms of the synthesized materials and Table 4.2 gives a summary of the information calculated from the BET measurments of all the samples.

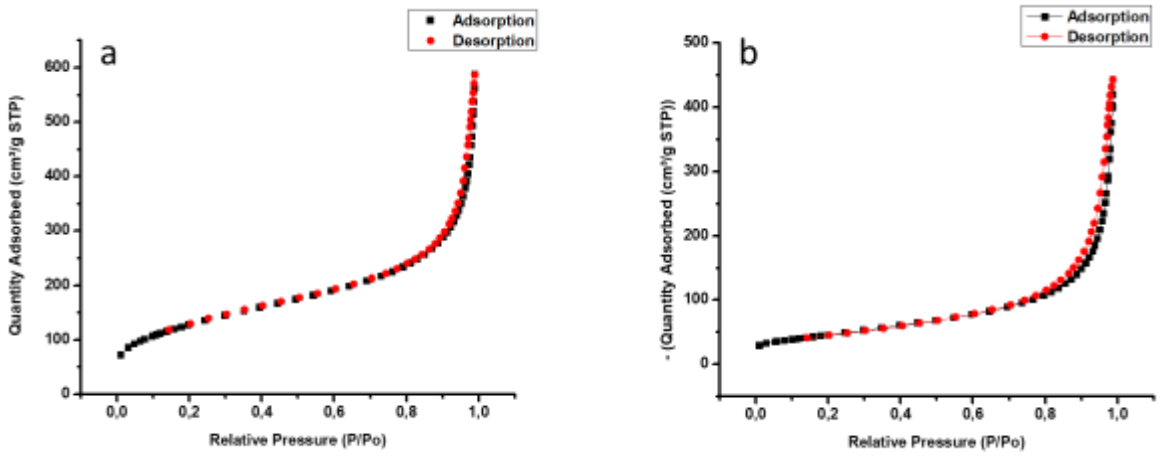


Figure 4. 10: N_2 adsorption-desorption isotherms of (a) HCS only and (b) 5% Os@HCS WI catalyst.

Both the HCS and 5% Os@HCS WI catalyst in Fig 4.10 (a) and (b), respectively, displayed a typical type II isotherm [222]. Both the type II isotherms showed a steep adsorption at relative pressures between 0.60 – 0.80 which can be attributed to the presence of a mesoporous carbon framework. Furthermore, the HCS isotherm show's a steeper adsorption curve than 5% Os@HCS WI catalyst and this accounts for the higher surface area of HCSs relative to the 5% Os@HCS WI catalyst. Both the isotherms show a very small to hysteresis loop between the adsorption and desorption peaks, indicating a small number of mesopores within the carbon framework. The mesoporous structure of the carbon framework is important in terms of the use of the HCS in catalytic reactions. The mesopores will reduce mass transfer resistance of reactants in and out of the carbon shell when the Os@HCS catalysts are employed in catalysis reactions (e.g. Fischer-Tropsch synthesis). In both the isotherms, a steep adsorption is observed at relative pressures close to 1.0, which is attributed to the large volume of HCSs [223].

Table 4. 2: Textual properties (surface area, pore volume and average pore size) of the hollow carbon sphere support and osmium encapsulated inside hollow carbon spheres.

Sample	Surface area (m^2/g)	Pore volume (cm^3/g)	Pore size (nm)
HCS only	441	0,87	7,7
5% Os@HCS WI	252	0,26	19,6
5% Os@HCS HDP	124	0,33	10,5
10% Os@HCS WI	162	0,43	15,9
10% Os@HCS HDP	119	0,65	14,1

Generally, it is expected that the measured surface area for each type of carbon would increase as (i) the number of pores increase, (ii) the pore volume increases, and (iii) the pore width decreases. Based upon the data given in Table 4.2 it can be seen that the specific surface area of HCSs decreased upon an addition of Os. This trend was expected because as the metal is loaded on the inner surface of the hollow support, blockage of some mesopores in the carbon framework would occur. Another observation is that catalysts prepared via the WI method show a higher surface area compared to those prepared via HDP method. The reason for this observation is currently not known.

4.4. Conclusion

In this chapter, we have successfully synthesized Os nanoparticles encapsulated inside hollow carbon spheres (Os@HCS) and Os nanoparticles supported on silica spheres (Os/SiO_2) as potential Fischer-Tropsch catalysts. The synthesized Os/SiO_2 were prepared via the wetness impregnation (WI) and homogeneous deposition precipitation (HDP) methods. It was observed that varying the synthesis method led to different levels of Os dispersion on the silica template. Which in turn resulted in better dispersion for the Os/SiO_2 prepared via HDP method compared

to WI method. The synthesized Os/SiO_2 were successfully carbonized using toluene in a chemical vapour deposition procedure and successfully etched to produce Os@HCS catalysts. Here it was observed that both Os@HCS catalyst prepared via WI and HDP method had well dispersed Os nanoparticles encapsulated within a carbon shell.

PXRD patterns revealed that Os nanoparticles encapsulated inside HCS were in the reduced phase. The efficacy of SiO_2 template removal was studied by TGA. The key observation from the TGA thermograms was that the silica template was completely removed from the carbon shell core by HF, as seen by the amount of residue remaining at 900 °C. At temperature between 600-700 °C, two major decomposition peaks due to metal catalysed and non-metal catalysed decomposition of HCS to CO_2 were observed. Another important observation was that Os oxidized to OsO_4 at temperature between 300-350 °C. Since OsO_4 is known to be health hazardous TGA experiments were discontinued. Generally, the HCSs encapsulating Os nanoparticles had a high surface area. The catalysts surface area decreased with an increase in metal loading. This observation was due to a blockage of some mesopores in the carbon framework of HCS.

Overall, the results obtained from EDS, FTIR, XRD, TGA, and BET show that both Os@HCS catalyst prepared via WI and HDP method had similar chemical and physical properties.

4.5. Reference

1. Lou, X.W.D., L.A. Archer, and Z. Yang, *Hollow micro-/nanostructures: Synthesis and applications.* Advanced Materials, 2008. **20**(21): p. 3987-4019.
2. Zhao, W., et al., *Uniform Rattle-type Hollow Magnetic Mesoporous Spheres as Drug Delivery Carriers and their Sustained-Release Property.* Advanced Functional Materials, 2008. **18**(18): p. 2780-2788.
3. Sun, Y., et al., *Synthesis and optical properties of nanorattles and multiple-walled nanoshells/nanotubes made of metal alloys.* Journal of the American Chemical Society, 2004. **126**(30): p. 9399-9406.
4. Choi, W.S., H.Y. Koo, and D.Y. Kim, *Scalable Synthesis of Chestnut-Bur-like Magnetic Capsules Loaded with Size-Controlled Mono-or Bimetallic Cores.* Advanced Materials, 2007. **19**(3): p. 451-455.
5. Su, F., et al., *Hollow carbon spheres with a controllable shell structure.* Journal of materials chemistry, 2006. **16**(45): p. 4413-4419.
6. Jiang, J., et al., *Enhanced room temperature hydrogen storage capacity of hollow nitrogen-containing carbon spheres.* International journal of hydrogen energy, 2010. **35**(1): p. 210-216.
7. Wen, Z., et al., *Hollow carbon spheres with wide size distribution as anode catalyst support for direct methanol fuel cells.* Electrochemistry communications, 2007. **9**(8): p. 1867-1872.
8. Gill, I. and A. Ballesteros, *Encapsulation of biologicals within silicate, siloxane, and hybrid sol− gel polymers: an efficient and generic approach.* Journal of the American Chemical Society, 1998. **120**(34): p. 8587-8598.
9. Gao, C., et al., *Templated synthesis of metal nanorods in silica nanotubes.* Journal of the American Chemical Society, 2011. **133**(49): p. 19706-19709.
10. Sun, Y., B. Mayers, and Y. Xia, *Metal nanostructures with hollow interiors.* Advanced Materials, 2003. **15**(7-8): p. 641-646.
11. Piñeiro-Redondo, Y., et al., *The influence of colloidal parameters on the specific power absorption of PAA-coated magnetite nanoparticles.* Nanoscale research letters, 2011. **6**(1): p. 383.
12. Zhang, Q., et al., *Self-templated synthesis of hollow nanostructures.* Nano Today, 2009. **4**(6): p. 494-507.

13. Büchel, G., et al., *A Novel Pathway for Synthesis of Submicrometer-Size Solid Core/Mesoporous Shell Silica Spheres.* Advanced Materials, 1998. **10**(13): p. 1036-1038.
14. Xiong, H., et al., *Cobalt catalysts supported on a micro-coil carbon in Fischer–Tropsch synthesis: A comparison with CNTs and CNFs.* Catalysis today, 2013. **214**: p. 50-60.
15. Trépanier, M., A.K. Dalai, and N. Abatzoglou, *Synthesis of CNT-supported cobalt nanoparticle catalysts using a microemulsion technique: role of nanoparticle size on reducibility, activity and selectivity in Fischer–Tropsch reactions.* Applied Catalysis A: General, 2010. **374**(1): p. 79-86.
16. Pérez-Lorenzo, M., et al., *Hollow-Shelled Nanoreactors Endowed with High Catalytic Activity*. Chemistry-A European Journal, 2013. **19**(37): p. 12196-12211.
17. Chen, Z., et al., *Diffusion induced reactant shape selectivity inside mesoporous pores of Pd@ meso-SiO2 nanoreactor in Suzuki coupling reactions.* The Journal of Physical Chemistry C, 2012. **116**(28): p. 14986-14991.
18. Chen, Z., et al., *Pd nanoparticles in silica hollow spheres with mesoporous walls: a nanoreactor with extremely high activity.* Chemical Communications, 2010. **46**(35): p. 6524-6526.
19. Nongwe, I., et al., *Synthesis of gold encapsulated in spherical carbon capsules with a mesoporous shell structure. A robust catalyst in a nanoreactor.* Catalysis Communications, 2014. **53**: p. 77-82.
20. Liu, R., et al., *Au@ carbon yolk–shell nanostructures via one-step core–shell–shell template.* Chemical Communications, 2014. **50**(4): p. 478-480.
21. Li, S., et al., *High-rate aluminium yolk-shell nanoparticle anode for Li-ion battery with long cycle life and ultrahigh capacity.* Nature communications, 2015. **6**.
22. Jayaprakash, N., et al., *Porous hollow carbon@ sulfur composites for high-power lithium–sulfur batteries.* Angewandte Chemie, 2011. **123**(26): p. 6026-6030.
23. Caruso, F., R.A. Caruso, and H. Möhwald, *Nanoengineering of inorganic and hybrid hollow spheres by colloidal templating.* Science, 1998. **282**(5391): p. 1111-1114.
24. Kim, M., et al., *Synthesis of nanorattles composed of gold nanoparticles encapsulated in mesoporous carbon and polymer shells.* Nano Letters, 2002. **2**(12): p. 1383-1387.
25. Fuertes, A.B., et al., *Synthetic route to nanocomposites made up of inorganic nanoparticles confined within a hollow mesoporous carbon shell.* Chemistry of Materials, 2007. **19**(22): p. 5418-5423.

26. Zhu, J., et al., *Fabrication of core− shell structure of M@ C (M= Se, Au, Ag2Se) and transformation to yolk− shell structure by electron beam irradiation or vacuum annealing*. Chemistry of Materials, 2009. **21**(16): p. 3848-3852.
27. Jia, B., et al., *One-pot synthesis of Cu–carbon hybrid hollow spheres*. Carbon, 2013. **62**: p. 472-480.
28. Holzwarth, U. and N. Gibson, *The Scherrer equation versus the'Debye-Scherrer equation'*. Nature Nanotechnology, 2011. **6**(9): p. 534-534.
29. Barnes, C.E., *Inorganic Chemistry (Catherine E. Housecroft and Alan G. Sharpe)*. Journal of Chemical Education, 2003. **80**: p. 747.
30. Xiong, H., et al., *Autoreduction and Catalytic Performance of a Cobalt Fischer–Tropsch Synthesis Catalyst Supported on Nitrogen-Doped Carbon Spheres*. ChemCatChem, 2010. **2**(5): p. 514-518.
31. Durndell, L.J., et al., *Tunable Pt nanocatalysts for the aerobic selox of cinnamyl alcohol*. Nanoscale, 2013. **5**(12): p. 5412-5419.
32. Yeh, Y.-Q., et al., *Synthesis of hollow silica spheres with mesostructured shell using cationic− anionic-neutral block copolymer ternary surfactants*. Langmuir, 2006. **22**(1): p. 6-9.

Chapter 5: Application – osmium encapsulated inside hollow carbon spheres as a Fischer Tropsch synthesis catalyst.

5.1. Introduction

The Fischer-Tropsch synthesis (FTS) is of great academic and industrial interest because it has proven to produce clean liquid fuels from syngas (CO and H_2), which may be produced from (i) gaseous fuels such as natural gas, coal gas, and biogas, (ii) liquid fuels such as heavy oils and oil residues, and (iii) solid fuels such as biomass and coal [1-4]. Among the transition metals used to catalyse the process, cobalt and iron based catalysts are the commercially used catalysts at temperatures between 200 and 300 °C, and at 10 to 60 bar pressure [1, 5, 6]. Generally the reaction involved in FTS requires a heterogeneous catalyst where the metal catalyst is supported on conventional oxides such as SiO_2, TiO_2 and Al_2O_3, or various shaped carbon materials [7-9]. Research work has shown that the support material plays a vital role in influencing the dispersion of the active metal as well as stabilizing the active metal phase against loss of surface area due to sintering or agglomeration in FTS reaction conditions.

As mentioned, generally conventional supports such as metal oxides are used in FTS. However, the drawback of using such supports includes the formation of hard-to-reduce complexes, for example Co_2SiO_2, $CoTiO_2$ and $Co_2Al_2O_4$. The hard-to-reduce complexes are attributed by the strong interaction of these supports with the catalyst precursors [10-12]. As an alternative, carbon-based materials have shown to be excellent support materials in FTS due to their chemical inertness thus meaning that they do not interact strongly with the catalyst precursor or active catalyst. In the last decade the possibility of making hollow supports with the metal placed inside the support has become possible [13, 14]. Recently several reports have been reported for improving the stability of metal nanoparticles by encapsulating the metal nanoparticles inside hollow porous shells [15, 16]. In the case of using carbon as the support, hollow carbon spheres (HCSs) have been used in heterogeneous catalysis due to their relative chemical inertness, thus allowing easier reducibility and increased metal catalytic activity [17, 18]. Recently, Phaahlamohlaka *et al* used ruthenium nanoparticles encapsulated in HCSs as a catalyst and from their study the HCS porous and hollow structure were shown to be stable and suitable for high pressure reaction conditions such as in FTS [19]. The Ru nanoparticles inside the HCSs were accessible to the syngas through the porous network and such observations were verified by the calculated turnover frequencies and product selectivities. The data

obtained indicated that the products could exit from the HCSs and that they were not held up significantly during the reaction [19].

Although much attention has been paid in recent years to the use of cobalt and iron based catalysts as a CO hydrogenation catalyst in FTS, less work has been done on osmium. In literature, studies performed by Basset *et al.* reported the first work done in investigating the catalytic properties of osmium in FTS and from their work Os/SiO_2 revealed to be catalytically active with C_1-C_5 hydrocarbons being produced [20]. However from their investigation methane (70%) was the dominant product. Another study performed by Knözinger and Zhao revealed that triosmium carbonyl cluster supported on Al_3O_4 had a catalytic activity in CO hydrogenation reactions with low conversions of C_1-C_4 hydrocarbons products being produced [21-25]. Ntombovuyo *et al.* also conducted a study on Os/SiO_2 catalyst under FTS and the catalyst showed some catalytic activity with C_1-C_3 hydrocarbons being the products produced [26]. From these studies Os metal clusters and complexes have shown to be active in FTS with only lower hydrocarbons being produced.

Even though osmium has been investigated on conventional oxide supports, to date, no reports on the application of Os nanoparticles encapsulated inside HCS (Os@HCS) for gas phase CO hydrogenation reaction in FTS has been reported. Since osmium and ruthenium resemble one another in their low oxidation state, in this chapter, we explore osmium nanoparticles encapsulated in hollow carbon spheres as a potential Fischer-Tropsch catalyst. In this chapter, the effect of varying the following parameters were tested: (i) the percentage loading of Os, (ii) the type of support used e.g. HCS or SiO_2, (iii) and the different reaction conditions such as temperature variation under FTS. The reducibility of the catalyst was studied using TPR analysis. The stability of the spent catalyst after FTS was investigated by TEM and PXRD analysis.

5.2. Experimental

5.2.1. Catalyst preparation

The catalyst precursor ($(NH_4)_2OsCl_6$) was prepared from potassium osmate, using the procedures described in *section 3.3.1*. Conventional FT catalysts are commonly prepared using homogenous deposition precipitation (HDP) and wetness impregnation (WI) procedures. In

this study the Os catalysts were prepared by using a homogenous deposition precipitation method using ($(NH_4)_2OsCl_6$) as the metal precursor loaded on the silica template. In homogenous deposition precipitation the catalyst was deposited on the silica template by using urea as the precipitating agent and urea hydrolysis was done for 12 h at 95 °C. Afterwards, the samples were dried overnight at 80 °C in an oven. The synthesized products were carbonized under chemical vapour deposition at 950 °C for 2 h, using toluene as the carbon source. After carbonization the products contained Os on the silica template were encapsulated in the carbon shell ($Os/SiO_2@C$). The obtained $Os/SiO_2@C$ was etched with HF to obtain Os encapsulated inside hollow carbon spheres (Os@HCS). A range of catalysts were made and the catalyst codes used to describe the different catalysts are given below:

1. **5% Os@HCS HDP**. Os catalyst encapsulated in HCSs, prepared from 5% Os nanoparticles loaded on the SiO_2 template via a homogenous deposition precipitation (HDP) method.

2. **10% Os@HCS HDP**. Os catalyst encapsulated in HCSs, prepared from 10% Os nanoparticles loaded on the SiO_2 template via a homogenous deposition precipitation (HDP) method.

3. **5% Os/SiO_2 HDP**. Os catalyst supported on SiO_2 prepared by homogenous deposition precipitation.
4. **10% Os/SiO_2 HDP**. Os catalyst supported on SiO_2 prepared by homogenous deposition precipitation.

5.2.2. Characterization

Transmission electron microscopy (TEM) images were taken on FEI Tecnai T12 microscope operated at 120 kV. Temperature programmed reduction (TPR) profiles were obtained by using a Micrometrics AutoChem II instrument fitted with a thermal conductivity detector (TCD) and three Brooks mas-flow controllers. TPR analysis was performed using 5% hydrogen gas in argon (50 ml/min) at 1 bar pressure while the temperatures was raised to 900 °C at a heating rate of 10 °C/min. Powder X-ray diffraction (PXRD) measurements were done using a Bruker

D2 phaser with Cu Kα (λ = 0.15406 nm), scan range 10-90° (2θ) with 0.026° steps. The instrument was operated at 30 kV and 10 mA.

5.2.3. Catalytic evaluation

Fischer-Tropsch reactor studies were performed in a fixed bed reactor made up of a 16 mm stainless steel tube with a frit inserted in the middle to serve as a support for the catalyst bed. The reactor was filled with steel balls so as to serve as a heat conductor where a homogenous heat distribution is enabled in the reactor. The catalysts used in the FTS experiments were 5% Os@HCS HDP, 10% Os@HCS HDP and 10% Os/SiO_2 used as a reference. The catalysts (0.5 g) were reduced in-situ by hydrogen gas passed at 220 ℃ for 16 h, at a flow rate of 45 ml/min^{-1} prior to FTS. The average FTS measurements were conducted at 220 ℃, 250 ℃, and 300℃ using syngas (29.2% CO, 10.3 of $\%N_2$ and balance of H_2) at a flow rate of 20 ml/min^{-1} and a total gas pressure of 10 bar. All gas lines after the reactor were kept at 150 ℃ and a hot trap placed immediately after the reactor was held at this temperature in order to collect wax. A second trap kept at ambient temperature was used to collect the oil and water mixture. The flow was controlled using a metering valve and measured by a bubble meter. Connected to the gas lines were two online GCs to monitor the composition of gaseous products, a GC-TCD and a GC-FID. An offline GC-FID was also connected to the traps and was used to analyse liquid products.

5.3. Results

The electron microscopy images were recorded on the 5% and 10% Os loaded on silica sphere template (Os/SiO_2) precursor used to prepare the 5% and 10% Os encapsulated in hollow carbon sphere (Os@HCS) materials, respectively. However, the difficulty in detecting the 5% Os/SiO_2 HDP catalyst by other characterization techniques resulted to the catalyst being excluded in PXRD, TPR and FTS evaluation sections.

5.3.1. Transmission electron microscopy

Reported in this section are the TEM images, as well as the size distribution, of the catalysts and their evaluation in Fischer-Tropsch synthesis in terms of their catalytic activity and selectivity. The catalysts were synthesized as described in *chapter 3*.

TEM analysis was employed to determine whether the catalyst particles were indeed supported on SiO_2 and encapsulated inside the HCS support and also to obtain a rough estimation of the metal particle sizes loaded on SiO_2 and inside the HCSs. Shown in Fig 5.1 are TEM images and Os particle size distributions of the 5% Os/SiO_2 and 10% Os/SiO_2 catalysts, respectively. Shown in Fig 5.2 TEM images and Os particle size distributions of are 5% Os@HCS HDP, 10% Os@HCS HDP, respectively.

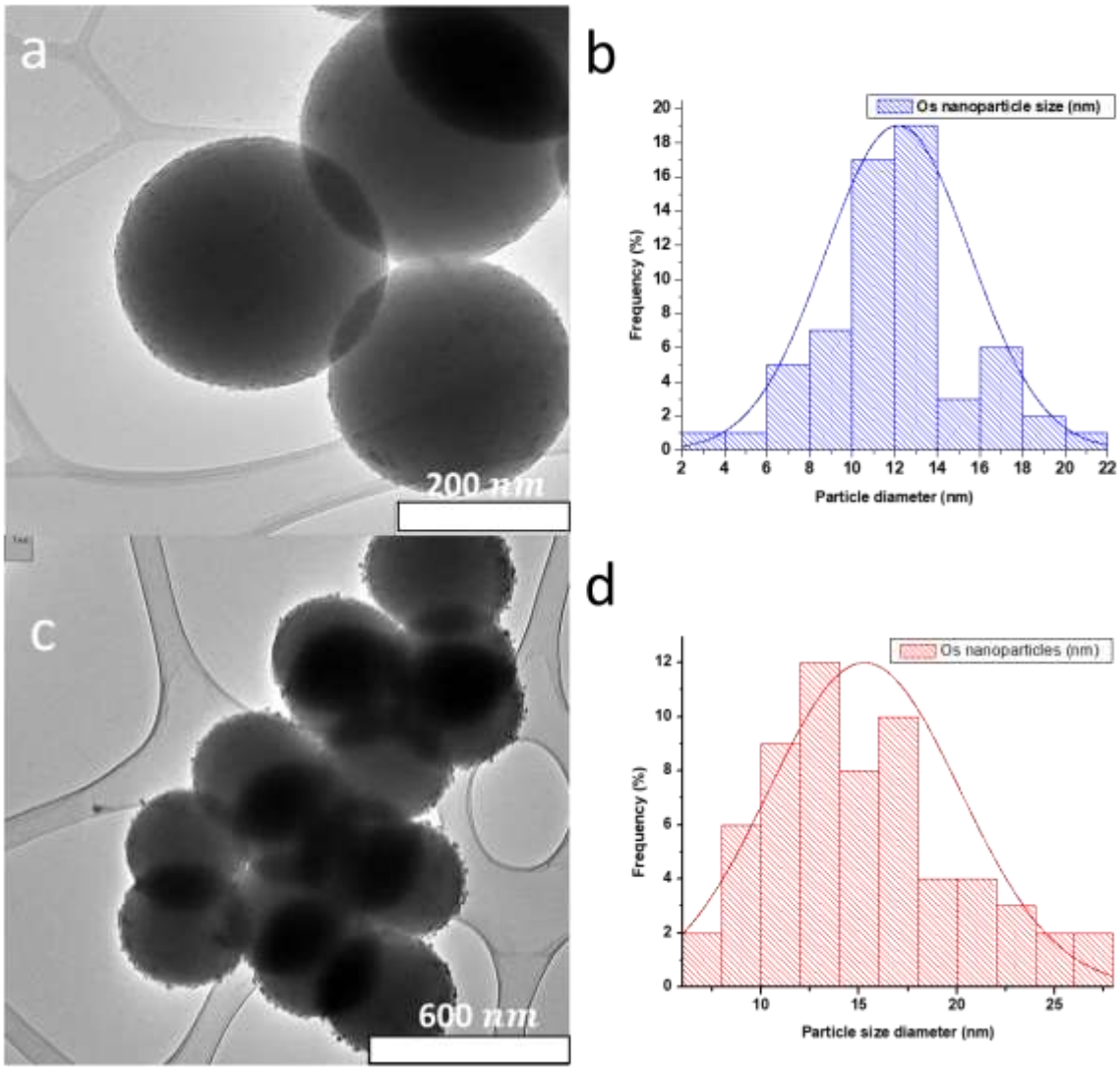


Figure 5. 1: TEM images and particle size distribution for: (a) and (b) 5% Os/SiO_2, (c) and (d) 10% Os/SiO_2 catalyst.

In Fig 5.1 (a) and (c), it can be seen that the Os nanoparticles were evenly distributed and well dispersed on the silica sphere support, and the average particle size of Os nanoparticles for the 5% Os/SiO_2 was 12 ± 3 nm and that of 10% Os/SiO_2 was 15 ± 5 nm.

Generally good Os particle dispersion occurred on the support and this was expected as the catalyst loading was achieved through homogenous deposition precipitation; the good dispersion is consistent with other literature reports using homogenous deposition precipitation. This 5% and 10% Os loaded silica support materials were then treated with toluene and the silica was removed by HF, forming the Os@HCS catalyst.

In Fig 5.2 (a) and (b), it can be seen that the 5% Os@HCS HDP catalyst Os nanoparticles were well dispersed inside the HCSs, and the average particle size of Os nanoparticle was 11 ± 4 nm. The 10% Os@HCS HDP catalyst showed metal aggregates inside the HCSs and the average particle size of the Os nanoparticle was 23 ± 11 nm, Fig (c) and (d). It appears that the 10% Os loaded catalyst sintered during the carbonization process. Such an observation was expected in that as the metal loading increased so did the metal particle size increase due to formation of metal clusters via sintering processes.

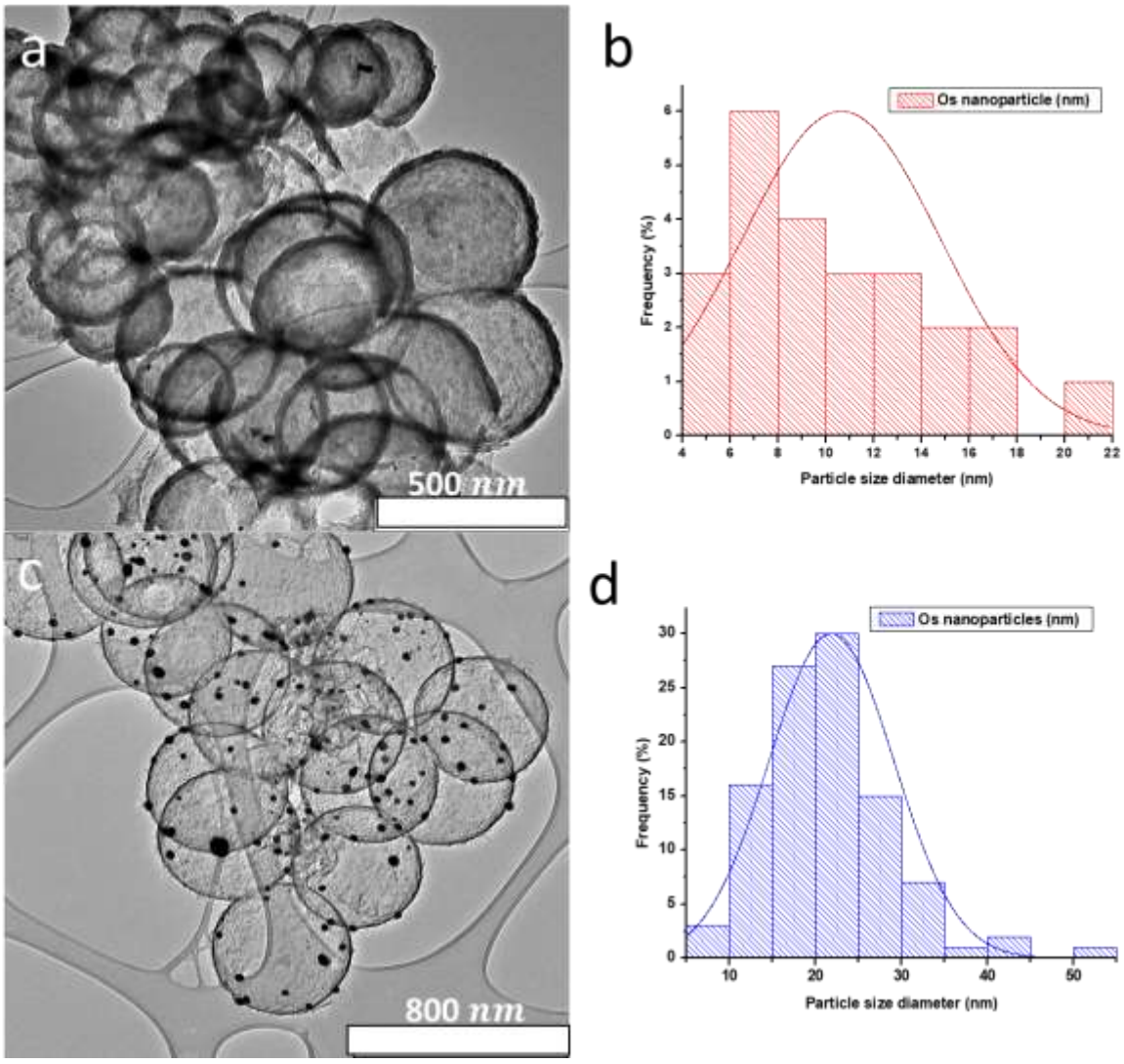


Figure 5. 2: TEM images and particle size distribution for: (a) and (b) 5% Os@HCS HDP, (c) and (d) 10% Os@HCS HDP.

Interestingly, it was observed from the TEM images of the 10% Os@HCS HDP catalyst that the surface of the HCS had become rougher (Fig 5.3 (a)), and that upon closer inspection the roughness of the HCS surface appeared to be due to the presence of carbon nanofibers (CNFs) that had grown on the carbon shell of the HCSs (Fig 5.3 (b)), during the CVD process.

The identity of the assumed CNFs on the spent 10% Os@HCS HDP catalyst has not been confirmed at this stage. A method to achieve this would be thermogravimetric analysis (TGA). However, due to complications associated with the volatility and health hazards associated with the formation of OsO_4 during TGA experiments. TGA analysis on the spent catalyst cannot be performed until modification of the TGA equipment to resolve the health issues are tackled (see *section 4.3.5*).

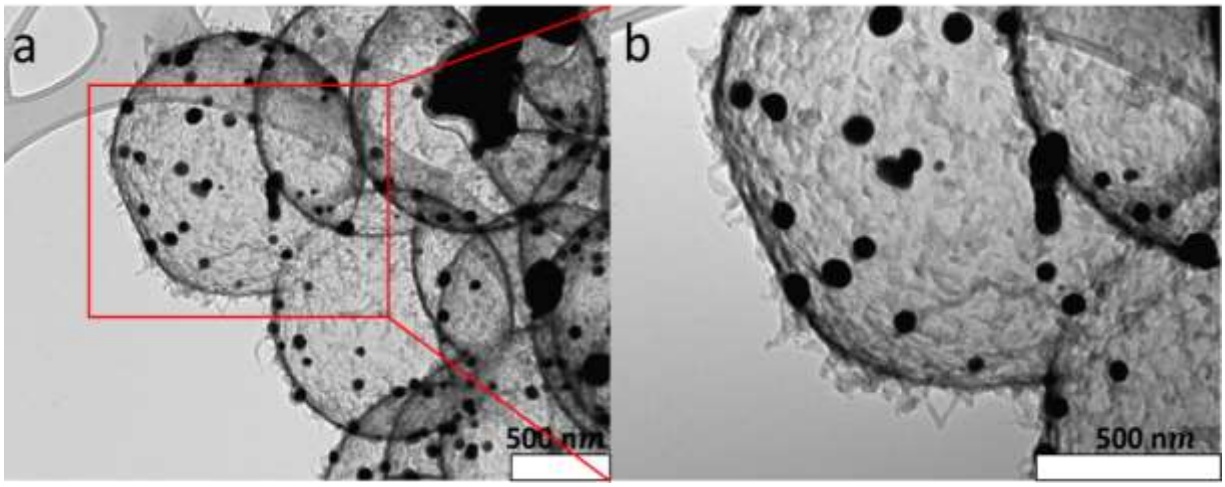


Figure 5. 3: TEM images of 10% Os@HCS HDP catalyst. (a) Lower magnification TEM image, displaying the larger portion of the spent catalyst. (b) High magnification TEM image, displaying the presence of carbon nanofibers on the surface of the HCSs from the spent catalyst.

Overall, it can be seen that the Os nanoparticles were well dispersed and indeed supported on the surface of the silica spheres for the SiO_2 supported catalyst and were well dispersed and indeed encapsulated inside the interstitial space of the carbon shell for the HCS supported catalysts and that the Os nanoparticles sintered upon an increase in metal loading.

5.3.2. Powder X-ray diffraction

Powder X-ray diffraction (PXRD) pattern of 5% Os@HCS HDP, 10% Os@HCS HDP, and 10% Os/SiO_2 are shown in Fig 5.4. The PXRD pattern of the HCS supported catalysts had similar features, displaying peaks at $2\theta = 44.3^o, 49.0^o, 51.2^o, 68.1^o$, and 81.6^o which correspond to the (100), (002), (101), (102), (110) planes of crystalline hexagonal Os (**ICSD 064993**) denoted "★" in the 5% and 10% Os@HCS HDP catalysts. The peak at $2\theta = 30^o$ denoted "●" corresponds to the amorphous (002) carbonaceous phase of the HCSs. From the 5% and 10% Os@HCS HDP catalysts it was observed that the supported Os was in a reduced phase. This suggests that Os was reduced by the support as described in *section 4.3.4*. The PXRD pattern of silica supported catalyst showed the silica peak denoted "▲" at $2\theta = 22.3^o$ and peaks at $2\theta = 15.6^o, 17.9^o, 25.6^o, 30.1^o, 36.5^o$ and 48.0^o which correspond to the (111), (200), (220), (311), (222), (400) planes of crystalline FCC $(NH_4)_2OsCl_6$ (metal precursor) [27] denoted "■" in the 10% Os/SiO_2 HDP catalyst. This suggests that the Os supported on silica is on its Os(IV) oxidation state. This observation supports the suggestion that the carbon is needed to reduce the Os.

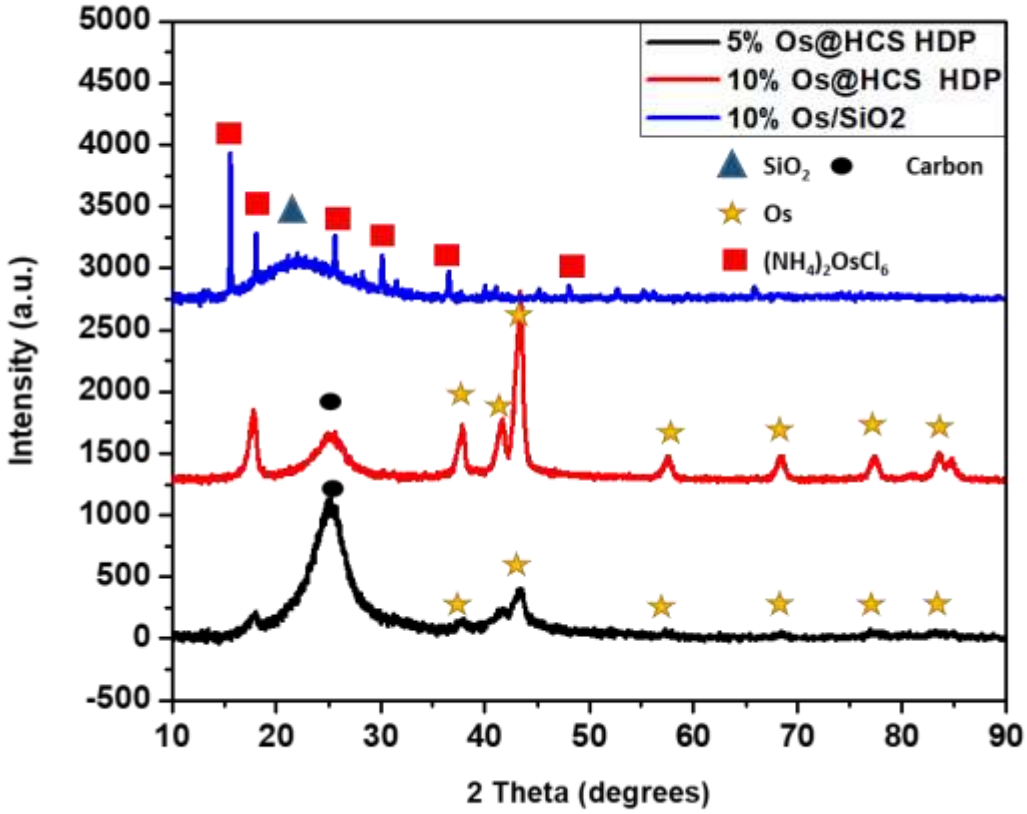


Figure 5. 4: PXRD pattern of 5% Os@HCS HDP, 10% Os@HCS HDP, and 10% Os/SiO_2

5.3.3. Temperature programmed reduction

Hydrogen temperature programmed reduction (H_2-TPR) analysis was performed to study the reduction of the Os compounds. Reduction profiles of 5% Os@HCS HDP, 10% Os@HCS HDP, and 10% Os/SiO_2 HDP catalysts are shown in Fig 5.5. The hydrogenation profile of the 10% Os/SiO_2 HDP catalyst shows three peaks ranging between 100–250 ℃ and these can be attributed to the reduction process of Os(IV) → Os(0) which seems to take place in different steps. The Os(IV) oxidation state is found in the $(NH_4)_2OsCl_6$ precursor salt. The possible steps in the process are as follows:

$$(NH_4)_2OsCl_6\,(IV)/SiO_2 + \frac{1}{2}H_2 \rightarrow OsCl_3\,(III)/SiO_2 + HCl + 2NH_4Cl \qquad \text{Eqn 5.1}$$

$$OsCl_3\ (III)/SiO_2 + \frac{1}{2}H_2 \rightarrow OsCl_2\ (II)/SiO_2 + HCl \qquad \text{Eqn 5.2}$$

$$OsCl_2\ (II)/SiO_2 + H_2 \rightarrow Os\ (0)/SiO_2 + 2HCl \qquad \text{Eqn 5.3}$$

It has been reported that unsupported $K_2[OsCl_6]$ salt shows three broad overlapping peaks at 271, 296 and 320 °C and the Os precursor supported on zirconium-doped mesoporous silica showed lower reduction temperatures ranging between 150-275 °C [28]. The 10% Os/SiO_2 HDP catalyst has a first reduction peak at 121°C which can be attributed to the reduction step Os(IV) → Os(III), the second reduction peak at 187 °C can be attributed to the reduction step Os(III) → Os(II), and the final reduction peak at 220 °C can be attributed to the reduction step Os(II) → Os(0) [28].

Another option to explain the data would be the following. The peak at ca 121 ^{0}C could correspond to removal of the NH_4 species. The ratio of the remaining two peaks (ca 3/1) would then correspond to the first peak at 187 ^{o}C being due to the two step reduction of Os (IV) to Os (II) and the peak at 220 ^{o}C due to the reduction of Os (II) to Os (0).

In contrast, the 5% and 10% Os@HCS HDP catalysts show no Os reduction steps. This observation can be attributed to the fact that the Os metal underwent autoreduction by the carbon support. The reduced phase of Os is believed to have taken place during the carbonization procedure at 950 ˚C under Ar gas as described in *section 3.3.4.2*. A study by Chen *et al*. reported that iron oxide supported both inside and outside multi-walled carbon nanotubes (CNTs) could be reduced by the CNT host above 600 ˚C [29]. Carbon spheres (CSs) are known to compose of curling graphitic flakes with random twisting, and these flakes, with sizes ranging from 1-10 nm, are not closed shells [30]. They are also to be present in HCSs. The edges of the graphitic flakes are ideal sites for absorbing oxygen [31]. The observation on the reduced phase of Os has been further supported by PXRD studies in *section 4.3.4 and 5.3.2*. It can be seen in Fig 5.5 that the 5% and 10% Os@HCS HDP catalysts undergoes a methanation "" reaction with hydrogen at 553 and 458 °C, respectively. The difference in breadth of the methanation peak is believed to be due to two effects; (1) the thickness of the carbon layer, and (2) the Os nanoparticle sizes and/or the Os loading percentage. The difference in thickness and

metal size results in a 5% Os@HCS HDP support having a broader peak, while the same effects results in a narrow peak for the 10% Os@HCS HDP support. Furthermore, the osmium catalyst can catalyse the hydrogenation of the HCSs. The methanation of the HCS on the 10% Os@HCS HDP catalyst was observed at lower temperature because the Os nanoparticles were large in size and had a higher loading inside the HCSs compared to the 5% Os@HCS HDP catalyst which showed methanation of HCSs at a higher temperature. The difference in intensity of the methanation peaks between the two catalysts is currently not known and further experiments will have to be performed to understand this phenomenon.

It is apparent that Os-support interaction influences the reduction behaviours of the Os chlorides. The metal-carbon support interaction influences the Os reduction as observed in the Os@HCS catalysts. In contrast, the Os/SiO_2 catalyst appeared not to be reduced and it required the presence of H_2 to be reduced, and the reduction phenomena corresponded to the different oxidation states of Os as mentioned in *section 5.3.2*. Overall, we have demonstrated that Os supported on SiO_2 is the Os (IV) and that Os salts can be reduced to Os metal upon heating the catalyst precursor under an inert gas (Ar) in the chemical vapour deposition process when supported inside the carbon shell (HCSs).

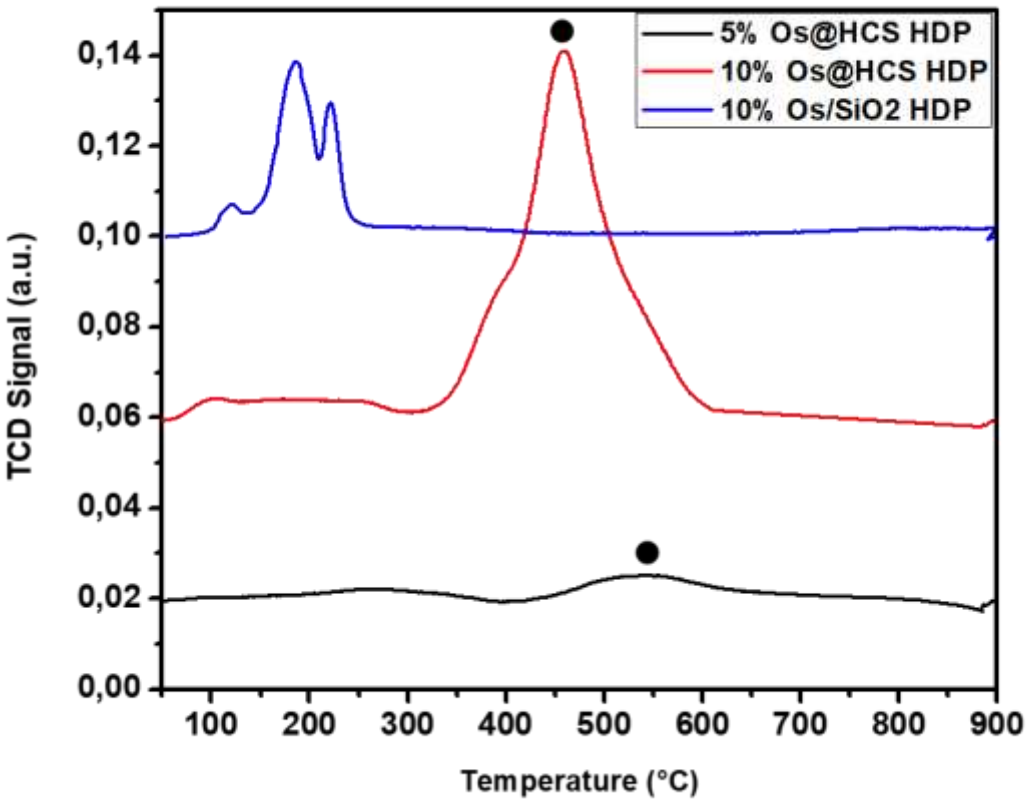


Figure 5. 5: H_2-TPR profile for Os nanoparticles on various supports, 5% Os@HCS HDP, 10% Os@HCS HDP, and 10% Os/SiO_2 HDP catalysts ("●" methanation).

5.3.4. Fischer-Tropsch evaluation

Fischer-Tropsch synthesis (FTS) was performed for a period of 150 hours using Os encapsulated inside the HCS and Os supported on SiO_2. The Os supported on SiO_2 was used as a reference catalyst to obtain base line information for the study of Os encapsulated inside HCSs. The CO conversions of the 5% Os@HCS HDP, 10% Os@HCS HDP, and 10 Os/SiO_2 HDP catalysts as a function of time on stream were studied at three temperatures (220, 250 and 300 ℃) and the data are shown in Fig 5.6 and Fig S.1 (see appendix). The temperature was raised after 50 h time periods as the Os@HCS catalysts appeared to generally achieve equilibrium in this timeframe. However, the 10% Os/SiO_2 HDP catalyst did not show stability with time on stream at a constant temperature (see Appendix1, Fig S.1). This was unexpected

since in literature this type of catalyst has been reported to be stable [22]. The 5% and 10% Os@HCS HDP catalysts reached a pseudo-steady state activity after (~20 h).

In Table 5.1 a summary of the catalysts performance is given. Among the three catalysts evaluated the 10% Os/SiO_2 HDP catalyst showed the highest FT activity, followed by the 10% Os@HCS HDP catalyst and lastly the 5% Os@HCS HDP catalyst (Table 5.1). Even though the 10% Os/SiO_2 HDP catalyst had the highest activity it however was the least stable catalyst (Fig S.2, see Appendix 1). The reason for the unstable behaviour of the catalyst could be due to strong metal-support interaction (Os-Si) and also metal sintering on the SiO_2 support. Another reason and the most probable one for the instability of the 10% Os/SiO_2 HDP catalyst could be due to instabilitiy in the flow rate of the syngas during the experiment. The CO conversion of 10% Os@HCS HDP catalyst was higher than that of 5% Os@HCS HDP catalyst and such observation was expected in that the CO conversion was expected to increase with metal loading on the support.

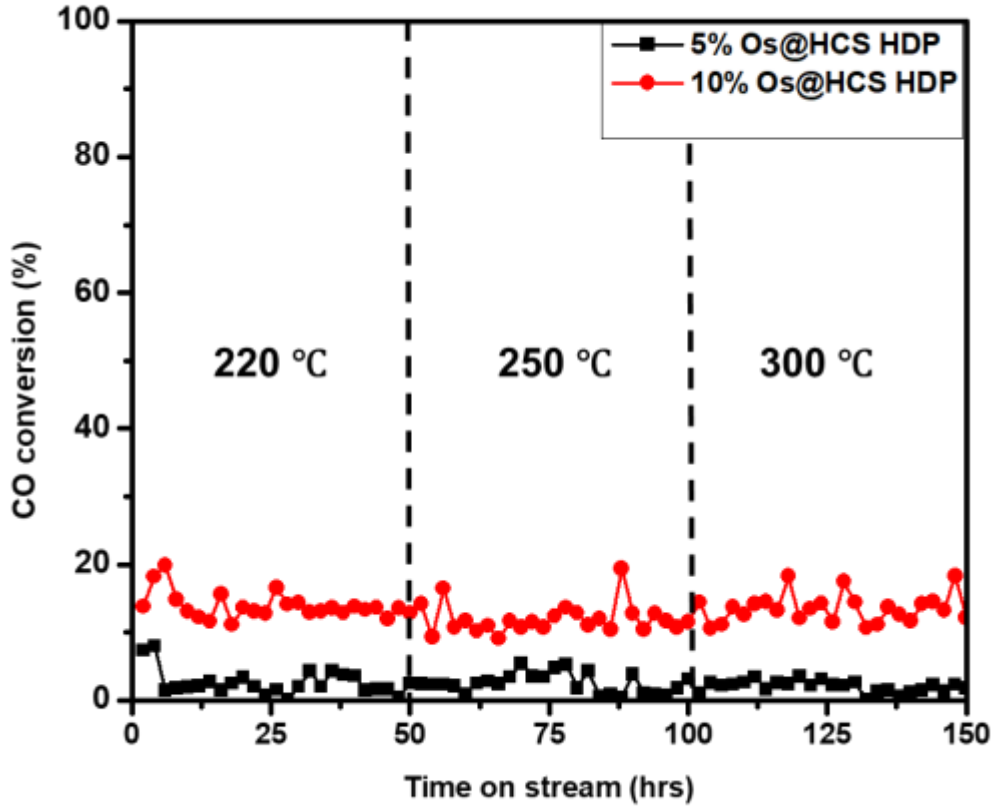


Figure 5. 6: CO conversions for the Os supported catalysts over 150 hours on stream at different reaction temperatures.

Table 5.1, Fig 5.6, and Fig S.1(see Appendix 1) presents the FTS CO conversion data at three different temperatures (220, 250 and 300 ℃). An observation made from the data collected at the three different temperatures was that the CO conversions showed a decrease as the temperature was increased with time on stream. This is unexpected if the catalyst particles do not change with temperature. This observation can however be attributed to proposals made by other authors in studies conducted on N-doped and undoped carbons where a continuous decrease in activity with time on stream was noted for samples supported on a pristine carbon support [32]. In the study the unusual behaviour was ascribed to significant catalyst sintering which occurred at high reaction temperatures on the pristine carbon materials. A similar proposal could be used to explain the data obtained for the Os dispersed inside the HCSs. While sintering can be reduced by placing one or two small particle within a HCS, the presence of

multiple particles within one HCS could still lead to sintering. Indeed TEM data indicated that each HCS was filled with many Os particles.

The 5% Os@HCS HDP catalyst showed a ~5% decrease in FT activity from 220 – 250 ℃ and a ~19% decrease in FT activity from 250 – 300 ℃. The 10% Os@HCS HDP catalyst showed a ~14% decrease in FT activity from 220 – 250 ℃ and a ~11% increase in FT activity from 250 – 300 ℃. This is to be contrasted with the 10% Os/SiO_2 HDP catalyst which showed a ~62% decrease in FT activity from 220 – 250 ℃ and a ~45% increase in FT activity from 250 – 300 ℃. This would then suggest that indeed the concept of limited sintering by use of metals contained in HCSs is seen here. Use of fewer Os particles within a HCS should lead to even less sintering. However the poor quality of the FT data for the 10% Os/SiO_2 HDP catalyst do not allow for further speculation on this issue.

Table 5. 1: Fischer-Tropsch synthesis catalytic performance of Os supported catalysts.

Sample	**Temperature (°C)**	**CO conversion (%)**	**Product selectivity (%)**		
			C_1	**C_2**	**Olefin/Paraffin (ratio)**
5% Os@HCS HDP	220	2.6	78.3	21.7	0.943
	250	2.48	75.3	24.7	0.685
	300	2.01	75.6	24.4	0.639
10% Os@HCS HDP	220	13.85	92.8	7.2	1.277
	250	11.95	90.3	9.7	0.718
	300	13.52	88.4	11.6	0.451
10% Os/SiO_2 HDP (reference)	220	19.36	64.3	35.7	0.335
	250	7.38	64.9	35.1	0.286
	300	13.53	66.1	33.9	0.387

From Table 5.1, it can be seen that the catalytic selectivity of the three catalysts showed high selectivity towards methane (> ~65%). Knözinger *et al.* and Bungani *et al.* [25, 26] also obtained high methane selectivity on Os/Al_2O_3 and Os/SiO_2 catalysts, respectively. The high selectivity to methane can be explained as being associated with the electronic effects of small nanoparticles [33, 34]. The other hydrocarbon product observed in the FT data was C_2 hydrocarbons. All three catalysts produced C_1 and C_2 hydrocarbons. The selectivity to C_2 hydrocarbons slightly increased when FTS was carried out at higher temperatures for the 5% and 10% Os@HCS HDP catalysts. In contrast, 10% Os/SiO_2 HDP catalyst slightly decreased in selectivity to C_2 hydrocarbons with an increase in FTS reaction temperature.

Figure 5.7 shows the gas phase olefin to paraffin ratio for the C_2 olefins for the three catalyst systems. It can be seen that the three catalysts formed more olefin products than paraffin products. As expected for both the 5% and 10% Os@HCS HDP catalysts, as temperature increased the olefin/paraffin product ratio decreased. In contrast, the 10% Os/SiO_2 HDP catalyst showed no trend in olefin to paraffin ratio with an increase in temperature.

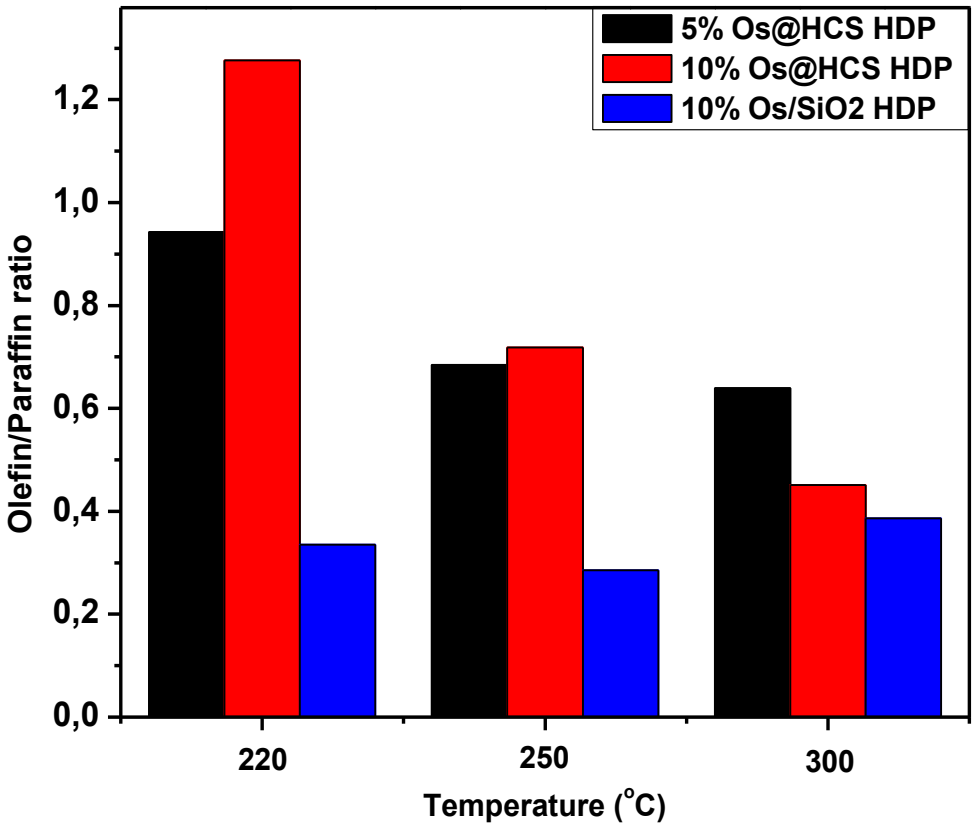


Figure 5. 7: Olefin to paraffin ratio of Os supported catalysts at various temperatures.

Generally, the Os catalysts showed low CO conversions when compared to conventional catalysts applied in FTS [26]. The dominant product produced from the Os supported catalysts was methane (average of 65% selectivity). The 5% and 10% Os@HCS HDP catalysts showed poor selectivity in the FTS, whereas, the 10% Os/SiO_2 was unstable during FTS and selectivity data were difficult to interpret. In conclusion, as expected the 5% Os@HCS HDP, 10% Os@HCS HDP, and 10 Os/SiO_2 HDP catalysts showed poor FTS catalytic behaviour with product selectivity mainly to C_1 and C_2 hydrocarbons.

5.3.5. Transmission electron microscopy studies of a spent catalyst

In an attempt to establish information on the Os catalysts after Fischer-Tropsch synthesis i.e. whether metal sintering had occurred during FTS, the spent catalysts were analysed by TEM (Fig 5.8).

Firstly, it was observed that indeed Os particles had sintered during the reaction. This was evident in that agglomerated Os particles were seen inside the HCSs and on the SiO_2 supports. These Os particles that sintered are highlighted with red circles for the three catalysts in Fig 5.8 (a, c, and e).

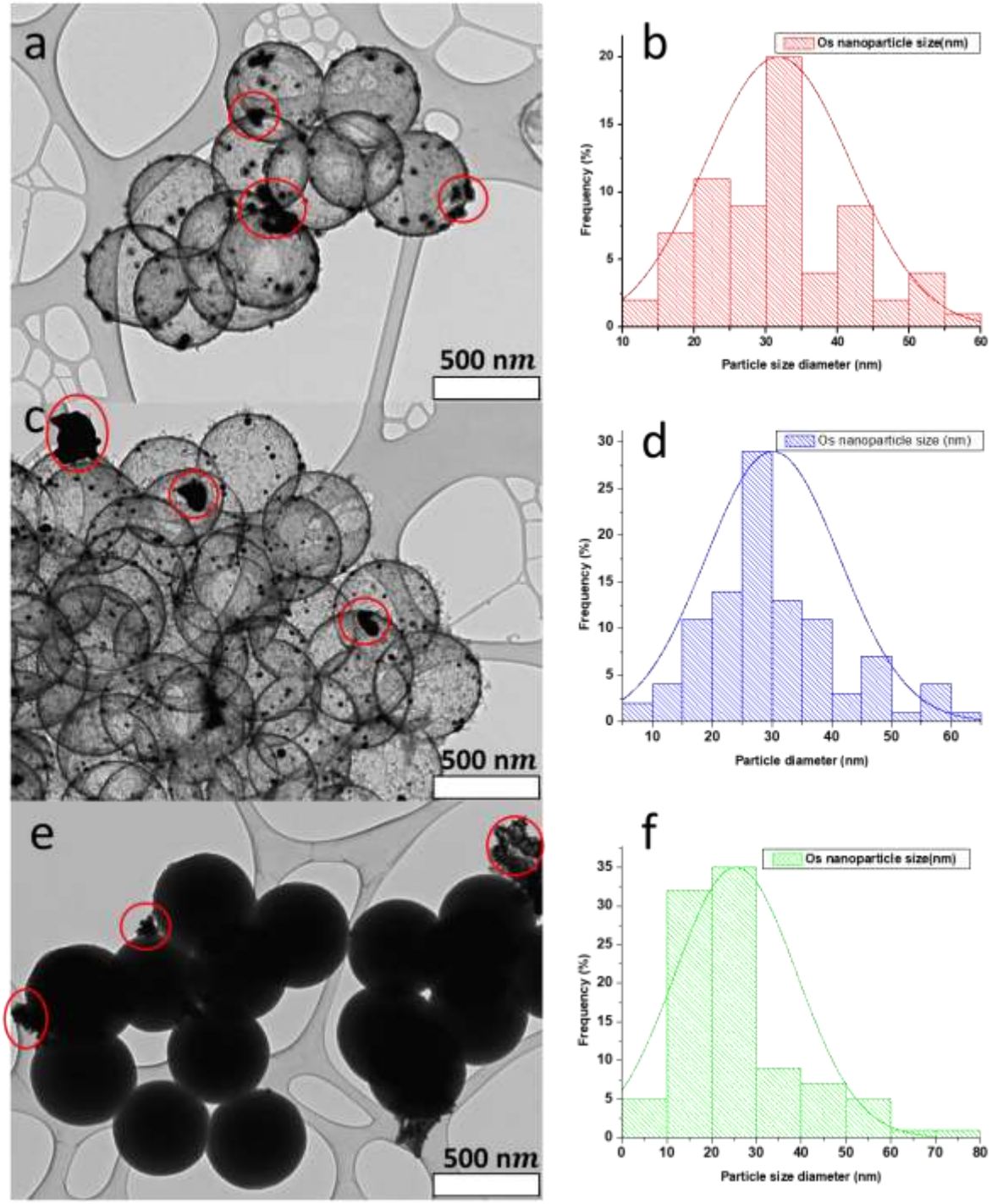


Figure 5. 8: TEM images and particle size distribution for: (a) and (b) 5% Os@HCS HDP, (c) and (d) 10% Os@HCS HDP, (e) and (f) 10% Os/SiO_2 spent catalysts.

Secondly, the dispersion of the Os particles varied among the three catalysts in that the 5% Os@HCS HDP catalyst showed more sintering and a lower dispersion. Interestingly the 10% Os@HCS HDP catalyst had Os particles that were in contrast better dispersed inside the HCSs

even after the high temperature reaction. The TEM images of the 10% Os/SiO_2 HDP catalyst showed that the Os particles had sintered on the SiO_2 support.

Lastly, the average metal particles sizes of the catalysts were measured on the spent catalysts (Fig 5.8 (b, d, and f). The 5% Os@HCSs HDP catalyst had a particle size of 32 $\pm$ 10 nm which reflected a 34% increase in size relative to the fresh catalyst, while the 10% Os@HCSs HDP catalyst had a particle size of 30 $\pm$ 12 nm which reflected a 23% increase relative to the fresh catalyst. More impotantly, the 10% Os/SiO_2 HDP catalyst had a particle size of 25 $\pm$ 14 nm which reflected a 52% increase relative to the fresh catalyst.

5.3.6. Poweder X-ray diffraction studies of a spent catalyst

PXRD analyses were also performed on the spent catalysts to identify the phase and particle size of the Os particles supported on SiO_2 and inside HCSs. Fig 5.9 shows the PXRD pattern of the 5% Os@HCS HDP, 10% Os@HCS HDP, and 10 Os/SiO_2 HDP spent catalysts. The 5% and 10% Os@HCS HDP spent catalyst peaks in the PXRD pattern were indexed according to **ICSD 064993**. The major peaks of the 5% and 10% Os@HCS HDP spent catalyst are labelled in Fig 5.9, where "●" represent carbon and was indexed according to the crystallographic data for amorphous carbon and the peaks denoted "★" represent the reduced hexagonal crystalline phase of osmium. The 10% Os/SiO_2 spent catalyst showed two peaks in the PXRD pattern and these were indexed according to the crystallographic data published by Finnie *et al.* [35]. The peak denoted "★" corresponds to the reduced hexagonal crystalline phase of osmium according to the crystallographic data contained in the EVA software. In all the spent catalysts analysed, the Os metal reduced phase was expected because the FTS reaction takes place under reducing conditions

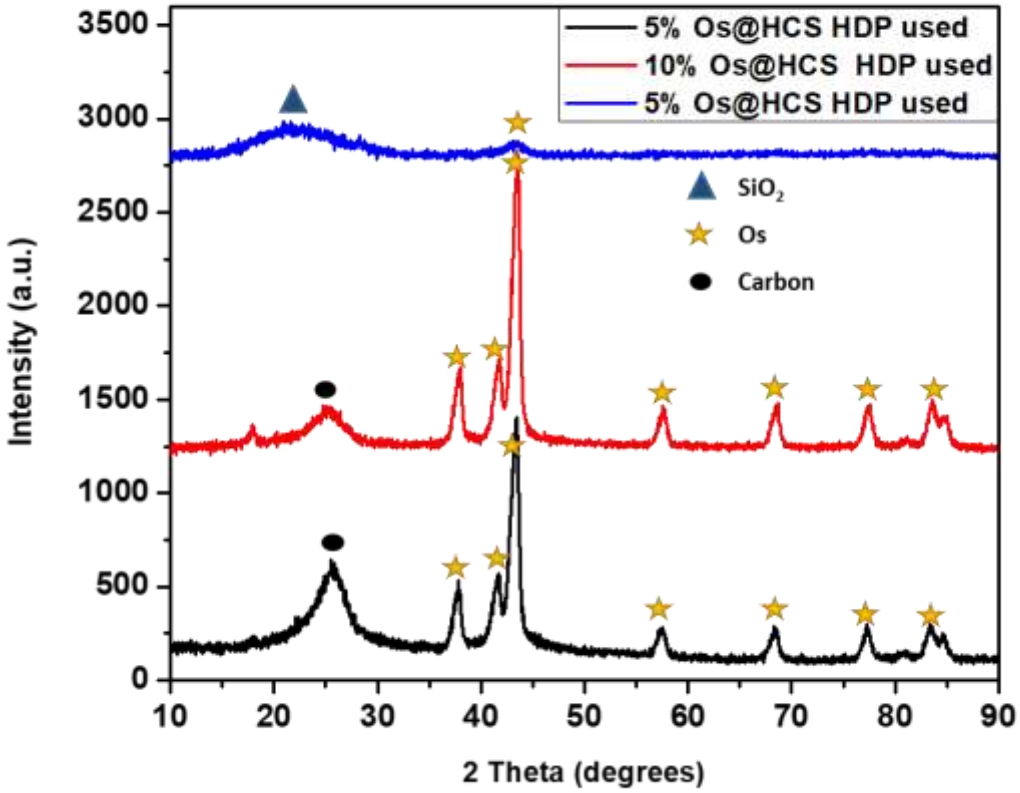


Figure 5. 9: PXRD patterns of the synthesized 5%, 10% Os@HCS and 10% Os/SiO2 via homogeneous deposition precipitation methods.

The crystallite sizes of the spent Os metal supported on HCS and SiO_2 were computed from the full width at half-maximum (FWHM) of the most intense peak values at $2\boldsymbol{\theta}$ using the Scherrer equation, (Table 5.2). Surprisingly the XRD data suggest little sintering with sizes actually smaller than those found before the FTS reaction. While it is known that the XRD data reflect an average particle size and that the TEM data relate to measurement of specific particles (those counted) these result were still unexpected.

Table 5. 2: Particle size data for osmium nanoparticles and hollow carbon spheres.

Sample name of spent catalysts	TEM Os nanoparticles (nm)	XRD Os nanoparticles (nm)
5% Os@HCS HDP	32	9.8
10% Os@HCS HDP	41	10.2
10% Os/SiO_2 HDP	25	4.2

5.4. Conclusion

In this chapter, we have used Os nanoparticles (NH_3OsCl_6 metal precursor) encapsulated inside hollow carbon spheres and Os nanoparticles supported on silica spheres as potential Fischer-Tropsch catalysts. The catalysts were successfully synthesized and indeed Os nanoparticles were supported on the silica. Interestingly, the Os particles supported inside the HCSs were reduced prior to a H_2 reduction step needed for the FTS reaction. The reducibility of Os particles of Os@HCS catalysts occurred during the carbonization procedure. On the other hand, Os particles supported on SiO_2 were found in the Os(IV) oxidation state after synthesis which was expected. Another finding was that Os-Si bonds had formed during the FTS for the Os/SiO_2 catalysts.

In the FTS evaluation study, it has been shown that Os nanoparticles have catalytic activity and selectivity in FTS. As expected Os@HCS and Os/SiO_2 catalysts showed poor catalytic activity in FTS with product selectivity mainly to C_1 and C_2 hydrocarbons. The Os supported catalysts showed high selectivity to methane production. More interestingly, the Os/SiO_2 catalyst revealed instability with time on stream compared to the Os@HCS catalysts which showed greater stability. After FTS all of the spent catalysts showed the presence of metal sintering.

Importantly the basis for the use of Os as a promoter for Co FT catalysts supported on HCSs has now been completed. While the data for the Os/SiO_2 catalyst will need to be repeated it is clear that the Os is a very poor FT catalyst irrespective of the two supports studied. This study will thus allow for a study of Os placed inside and outside the HCS to investigate spillover effects for Co/HCS and Co@HCS catalysts, as has been done for equivalent Ru promoted catalysts.

5.5. Reference

1. Jager, B. and R. Espinoza, *Advances in low temperature Fischer-Tropsch synthesis.* Catalysis Today, 1995. **23**(1): p. 17-28.
2. Zhang, Q., J. Kang, and Y. Wang, *Development of novel catalysts for Fischer–Tropsch synthesis: tuning the product selectivity.* ChemCatChem, 2010. **2**(9): p. 1030-1058.
3. Masters, C., *The Fischer-Tropsch Reaction.* Advances in Organometallic Chemistry, 1979. **17**: p. 61-103.
4. Rostrup-Nielsen, J.R., *Catalytic steam reforming*, in *Catalysis*. 1984, Springer. p. 1-117.
5. Dry, M., *The fischer-tropsch synthesis.* Catalysis science and technology, 1981. **1**: p. 159-255.
6. Oukaci, R., A.H. Singleton, and J.G. Goodwin, *Comparison of patented Co F–T catalysts using fixed-bed and slurry bubble column reactors.* Applied Catalysis A: General, 1999. **186**(1): p. 129-144.
7. Jenness, G.R. and J.R. Schmidt, *Unraveling the Role of Metal-Support Interactions in Heterogeneous Catalysis: Oxygenate Selectivity in Fischer-Tropsch Synthesis.* Acs Catalysis, 2013. **3**(12): p. 2881-2890.
8. Xiong, J., X. Dong, and L. Li, *CO selective methanation in hydrogen-rich gas mixtures over carbon nanotube supported Ru-based catalysts.* Journal of Natural Gas Chemistry, 2012. **21**(4): p. 445-451.
9. Kang, J., et al., *Ruthenium nanoparticles supported on carbon nanotubes as efficient catalysts for selective conversion of synthesis gas to diesel fuel.* Angewandte Chemie, 2009. **121**(14): p. 2603-2606.
10. Mogorosi, R.P., et al., *Strong-metal–support interaction by molecular design: Fe–silicate interactions in Fischer–Tropsch catalysts.* Journal of catalysis, 2012. **289**: p. 140-150.
11. Liu, Y., et al., *Titania-decorated silicon carbide-containing cobalt catalyst for fischer–tropsch synthesis.* ACS Catalysis, 2013. **3**(3): p. 393-404.
12. Zhang, S., et al., *Dynamical Observation and Detailed Description of Catalysts under Strong Metal–Support Interaction.* Nano letters, 2016. **16**(7): p. 4528-4534.
13. Yin, Y., et al., *Formation of hollow nanocrystals through the nanoscale Kirkendall effect.* Science, 2004. **304**(5671): p. 711-714.

14. Kim, S., et al., *IR Spectroscopic Observation of Molecular Transport through Pt@ CoO Yolk− Shell Nanostructures.* Journal of the American Chemical Society, 2007. **129**(30): p. 9510-9513.
15. Hu, Y., et al., *Size-controlled synthesis of highly stable and active Pd@ SiO2 core–shell nanocatalysts for hydrogenation of nitrobenzene.* The Journal of Physical Chemistry C, 2013. **117**(17): p. 8974-8982.
16. Du, X. and J. He, *Carrier effect in the synthesis of rattle-type Au@ hollow silica nanospheres by impregnation and thermal decomposition method.* Microporous and Mesoporous Materials, 2012. **163**: p. 201-210.
17. Xiong, H., et al., *Cobalt catalysts supported on a micro-coil carbon in Fischer–Tropsch synthesis: A comparison with CNTs and CNFs.* Catalysis today, 2013. **214**: p. 50-60.
18. Trépanier, M., A.K. Dalai, and N. Abatzoglou, *Synthesis of CNT-supported cobalt nanoparticle catalysts using a microemulsion technique: role of nanoparticle size on reducibility, activity and selectivity in Fischer–Tropsch reactions.* Applied Catalysis A: General, 2010. **374**(1): p. 79-86.
19. Phaahlamohlaka, T.N., et al., *Ruthenium nanoparticles encapsulated inside porous hollow carbon spheres: A novel catalyst for Fischer–Tropsch synthesis.* Catalysis Today, 2016. **275**: p. 76-83.
20. Basset, J., et al., *Supported cluster and Mechanism of CO Reduction.* Fundam. Res. Homogeneous Catal, 1984: p. 19-53.
21. Ede, S.R., U. Nithiyanantham, and S. Kundu, *Enhanced catalytic and SERS activities of CTAB stabilized interconnected osmium nanoclusters.* Physical Chemistry Chemical Physics, 2014. **16**(41): p. 22723-22734.
22. Nithiyanantham, U., S.R. Ede, and S. Kundu, *Self-assembled wire-like and honeycomb-like osmium nanoclusters (NCs) in DNA with pronounced catalytic and SERS activities.* Journal of Materials Chemistry C, 2014. **2**(19): p. 3782-3794.
23. Anantharaj, S., et al., *Osmium organosol on DNA: application in catalytic hydrogenation reaction and in SERS studies.* Industrial & Engineering Chemistry Research, 2014. **53**(49): p. 19228-19238.
24. Boyd, E.P., et al., *Chemical vapor deposition of metallic thin films using homonuclear and heteronuclear metal carbonyls.* Chemistry of materials, 1997. **9**(5): p. 1154-1158.
25. Knözinger, H., et al., *Alumina-supported CO hydrogenation catalysts prepared from molecular osmium and ruthenium clusters.* Faraday Discussions of the Chemical Society, 1981. **72**: p. 53-71.

26. Bungane, N., et al., *Fischer-Tropsch CO-Hydrogenation on SiO2-supported Osmium Complexes.* Zeitschrift für Naturforschung B, 2008. **63**(3): p. 289-292.
27. Swanson, H.E., E. Tatge, and R.K. Fuyat, *Standard X-ray diffraction powder patterns.* 1953.
28. Eliche-Quesada, D., et al., *Ru, Os and Ru–Os supported on mesoporous silica doped with zirconium as mild thio-tolerant catalysts in the hydrogenation and hydrogenolysis/hydrocracking of tetralin.* Applied Catalysis A: General, 2005. **279**(1): p. 209-221.
29. Chen, W., et al., *Facile autoreduction of iron oxide/carbon nanotube encapsulates.* Journal of the American Chemical Society, 2006. **128**(10): p. 3136-3137.
30. Kang, Z. and Z. Wang, *On accretion of nanosize carbon spheres.* The Journal of Physical Chemistry, 1996. **100**(13): p. 5163-5165.
31. Wang, Z. and Z. Kang, *Graphitic structure and surface chemical activity of nanosize carbon spheres.* Carbon, 1997. **35**(3): p. 419-426.
32. Lu, J., et al., *Promotion effects of nitrogen doping into carbon nanotubes on supported iron Fischer–Tropsch catalysts for lower olefins.* ACS Catalysis, 2014. **4**(2): p. 613-621.
33. Den Breejen, J., *Cobalt particle size effects in catalysis*. 2010, Utrecht University.
34. van Dijk, H.A.J., *The Fischer-Tropsch synthesis: A mechanistic study using transient isotopic tracing*. 2001: Technische Universiteit Eindhoven Eindhoven, The Netherlands.
35. Finnie, L.N., *Structures and compositions of the silicides of ruthenium, osmium, rhodium and iridium*. Journal of the Less Common Metals, 1962. **4**(1): p. 24-34.

Chapter 6: Conclusions and recommendations

6.1. Conclusion

In this research project, osmium (Os) nanoparticles encapsulated inside hollow carbon spheres (HCSs), a core-shell structure, was prepared as a potential catalyst for Fischer-Tropsch synthesis (FTS). The support material, HCSs, was synthesized via a hard templating method using silica spheres, synthesized using a Stöber method. Stöber silica spheres were prepared and Os nanoparticles were deposited on the SiO_2 via two methods: homogenous deposition precipitation (HDP) and wetness impregnation (WI). The Os/SiO_2 particles were carbonized using chemical vapour deposition (CVD) with toluene as the carbon source. Removal of the silica spheres resulted in the formation of Os nanoparticles encapsulated in the hollow carbon spheres (Os@HCS). The catalysts were characterized by TEM, SEM, FTIR, PXRD, TGA, nitrogen adsorption–desorption, and H_2-TPR techniques.

Data obtained from TEM and PXRD studies for the Os@HCS catalysts showed that Os nanoparticles with a size of 11-17.5 nm in diameter had formed (hexagonal cubic packed structure) and that they were indeed encapsulated inside the HCSs. The size of the Os nanoparticles increased with an increase in Os percentage loading on SiO_2. The HCS diameter ranged between 450-560 nm with a carbon shell thickness of 20-34 nm. Interestingly, in one of the synthesized catalyst the HCSs surface was rough and this was presumed to be due to the presence of carbon nanofibers (CNFs) that had grown on the carbon shell of the HCS during the CVD process. PXRD patterns revealed that Os nanoparticles encapsulated inside the HCSs were in the reduced phase. The PXRD pattern of the silica supported catalyst showed that the Os particles supported on SiO_2 were found in the Os(IV) oxidation state as the osmium precursor was $(NH_4)_2OsCl_6$.

The efficacy of SiO_2 template removal was studied by TGA. The key observation from the TGA thermograms was that the silica template was completely removed from the carbon shell core by HF, as seen by the amount of residue remaining at 900 °C. At temperatures between 600-700 °C, two major decomposition peaks due to metal catalysed and non-metal catalysed

decomposition of HCSs to CO_2 were observed. Another important observation was that Os oxidized to OsO_4 at temperature between 300-350 °C. Since OsO_4 is known to be a health hazard, TGA experiments were discontinued. Generally, the HCSs encapsulating Os nanoparticles had a high surface area. The catalysts surface area decreased with an increase in metal loading. This observation was due to a blockage of some mesopores in the carbon framework of the HCS by Os.

Prior to FTS, H_2-TPR analysis was performed to study the reduction of the Os compounds. The Os particles supported on SiO_2 were found to be in the Os(IV) oxidation state and a three-step reduction process took place to give Os(0). In the three step process 3 peaks (ca 121 ^oC, 187 ^oC, and 220 ^oC) could correspond to the expected Os three step reduction process. Another option to explain the data would be that the peak at ca 121 ^oC could be attributed to the removal of NH_3 species followed by the remaining two peaks that could be attributed to the three step reduction being observed as a two-step reduction of Os. The Os particles encapsulated inside the HCSs were found in their reduced phase. The reduced Os phase was attributed to an auto-reduction process involving the HCS support. The reducibility of Os particles in the Os@HCS catalysts occurred during the carbonization procedure.

FTS studies on Os@HCS and Os/SiO_2 catalysts were performed at 220, 250 and 300 °C (P = 10 bar, flow rate = 20 ml/min). In the FTS evaluation study, the Os@HCS and Os/SiO_2 catalysts showed poor catalytic activity in FTS with high selectivity towards methane (> ~65%). The Os supported catalysts showed a product selectivity mainly to C_1 and C_2 hydrocarbons. More interestingly, the Os/SiO_2 catalyst revealed instability with time on stream compared to the Os@HCS catalysts which showed greater stability. After FTS all of the spent catalysts showed the presence of Os metal sintering.

6.2. Recommendations

Since Os@HCS catalysts undergo Os to OsO_4 oxidation in the TGA. OsO_4 is known to cause severe lung, skin and eye damage and this poses a health hazard. For this reason we recommend

further TGA experiments with modifications of the TGA equipment to resolve the health issues associated with OsO_4 formation, e.g. include a gas trap or OsO_4 absorbent.

Importantly the basis for the use of Os as a promoter for Co FT catalysts which are supported on HCSs has now been completed. While the data for the Os/SiO_2 catalyst will need to be repeated it is clear that the Os is a very poor FT catalyst irrespective of the two supports studied. This study will thus allow for a study of Os placed inside and outside the HCS to investigate spillover effects for Co/HCS and Co@HCS catalysts, as has been done for equivalent Ru promoted catalysts.

Appendix 1

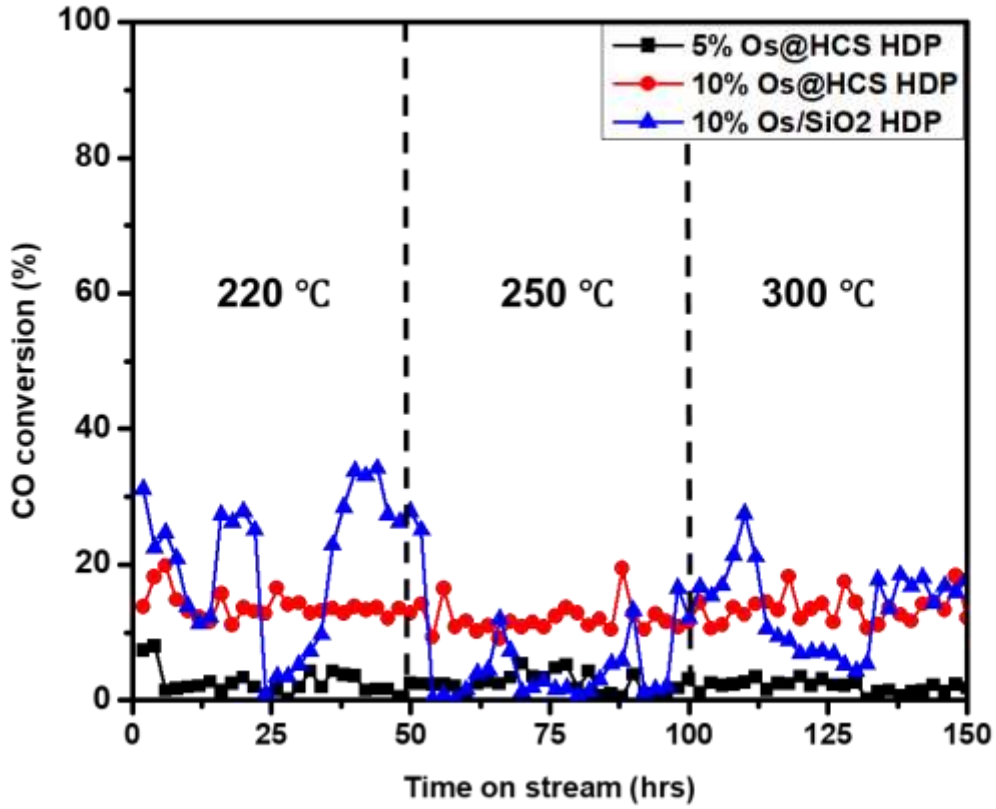


Figure S. 1: CO conversions for the Os supported catalysts over 150 hours on stream at different reaction temperatures.

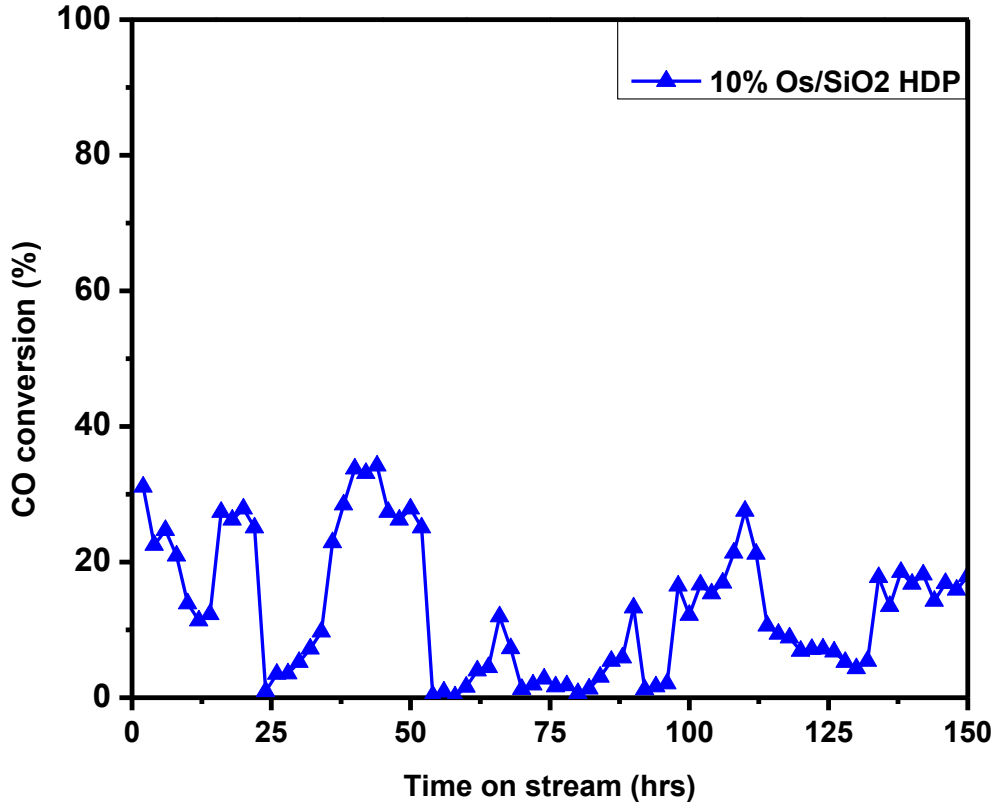


Figure S. 2: CO conversions for the Os/SiO_2 catalyst over 150 hours on stream at different reaction temperatures.